Static and Dynamic Electron Microscopy Investigations at the Atomic and Ultrafast Scales

A DISSERTATION
SUBMITTED TO THE FACULTY OF THE GRADUATE SCHOOL
OF THE UNIVERSITY OF MINNESOTA
BY

Pranav Kumar Suri

IN PARTIAL FULFILLMENT OF THE REQUIREMENTS
FOR THE DEGREE OF
DOCTOR OF PHILOSOPHY

Advisor: David J. Flannigan

May 2016

ACKNOWLEDGEMENTS

I know not how to thank you, you're truly a part of me
With me every moment, together at every step are we

On the inner stage, consciousness dances unfazed
Formless takes form, the cosmic creation stands amazed.

Stage and dancer merge into one, so do the seer and the scenery
The speaker and the audience, the Master and the devotee

This is the only truth, the rest is Maya's cover
Whom to thank here, where there is no other.

- *Sri Sri*

I am grateful to my Spiritual Guru, Sri Sri Ravi Shankar, for his witty wisdom of leading healthy life and knowledge of Sudarshan Kriya which made me mature, kept me stress-free and helped me to sail happily through the ups and downs of my Ph.D. journey. Hon. Prime Minister of India, Shri Narendra Modi, for his exuberant leadership skills, inspirational speeches, hard work and perseverance which I cherish every day in my life.

I am extremely thankful to my advisor Prof. David J. Flannigan whose constant support, guidance and criticism inspired me to keep pushing my limits and to put in my best effort in the professional academic life. His own life is an example of perseverance, hard work and strive for perfection. I feel proud and lucky that I spent my graduate career with the ever caring, super smart and enthusiastic Flannigan Group members – Boo, Dan, Alyssa, Dayne, Dr. David Valley, Tom, Jess, Jeff, Kyle - who inspired me with their deeds and kept cheering me up with their exotic UEM movies, and were always ready to give feedback on my write-ups and presentations, and tremendously helped me in learning UEM.

Prof. Jian-Ping Wang for giving his support in my graduate career and serving on my thesis committee, and Wang group members – Dr. Yanfeng, Mehedi – for providing me iron-nitride specimens and spending time on analysis of TEM results. Our collaborators at Oak Ridge National Lab – Prof. Mandrus and Dr. Yan – for providing extremely high quality LaFeAsO single-crystals which made my life a little easy, and Seagate for providing TEM specimens made out of HAMR devices.

Prof. Andre Mkhoyan and Prof. Bill Gerberich for initiating me in the graduate school life and helping me to seamlessly go through the Ph.D. qualifying exams and coursework. Mkhoyan and Gerberich group members – Al, Anudha, Andrew, Michael, Prof. Jong Jeong, Eric, Jason, Claire, Prashant, Ryan, Jake – for contributing towards my

electron microscopy and nanoindentation learning experiences. Special thanks to Prof. Jong, Michael, Andrew, Al, Anudha, Jason for invigorating discussions and teaching me invaluable electron microscopy lessons and tricks.

My Art of Living family in Minnesota – Deepti, Abhay, Mohan, Sarita, Eshitha, Sathya, Narayan, Karthik, Mike, Rosemary, Anna, Derek, Shashi and many more - who were my buddies inside and outside of UofM. Special thanks to my multiple mothers in Minnesota – Meena Aunty, Girija Aunty, Kala Aunty, Laxmi Aunty, Shantala – who fed me Indian delicacies during my stay at Minnesota.

My mother Sushma Kumari who inculcated values in me and kept cheering me every week over phone from India. My grandfather Rajendranath Suri for teaching me and monitoring my school performance which instilled scholarly habits in me. My grandmother Shakuntala Devi for feeding me and for introducing me to the world of spirituality. My father Ramesh Sharma who is the backbone of our family. Mrs. Manju Verma for cooking and mailing me delicious cuisines from India.

My undergraduate advisors and instructors Krishanu Biswas, Kallol Mondal, Dipak Mazumdar, Rajeev Shekhar and B. S. Murty who saw light in me and inspired me to pursue research and academic career.

All of them have played a significant role in shaping my personality. You all truly are a part of my life!

To Mummy, Papa, Nanaji, Naniji

ABSTRACT

Advancements in the electron microscopy capabilities – aberration-corrected imaging, monochromatic spectroscopy, direct-electron detectors – have enabled routine visualization of atomic-scale processes with millisecond temporal resolutions in this decade. This, combined with progress in the transmission electron microscopy (TEM) specimen holder technology and nanofabrication techniques, allows comprehensive experiments on a wide range of materials in various phases via *in situ* methods. The development of ultrafast (sub-nanosecond) time-resolved TEM with ultrafast electron microscopy (UEM) has further pushed the envelope of *in situ* TEM to sub-nanosecond temporal resolution while maintaining sub-nanometer spatial resolution. A plethora of materials phenomena – including electron-phonon coupling, phonon transport, first-order phase transitions, bond rotation, plasmon dynamics, melting, and dopant atoms arrangement – are not yet clearly understood and could be benefitted with the current *in situ* TEM capabilities having atomic-level and ultrafast precision. Better understanding of these phenomena and intrinsic material dynamics (e.g. how phonons propagate in a material, what time-scales are involved in a first-order phase transition, how fast a material melts, where dopant atoms sit in a crystal) in new-generation and technologically important materials (e.g. two-dimensional layered materials, semiconductor and magnetic devices, rare-earth-element-free permanent magnets, unconventional superconductors) could bring a paradigm shift in their electronic, structural, magnetic, thermal and optical applications.

Present research efforts, employing cutting-edge static and dynamic *in situ* electron microscopy resources at the University of Minnesota, are directed towards understanding the atomic-scale crystallographic structural transition and phonon transport in an iron-pnictide parent compound LaFeAsO, studying the mechanical stability of fast moving hard-drive heads in heat-assisted magnetic recording (HAMR) technology, exploring the possibility of ductile ceramics in magnesium oxide (MgO) nanomaterials, and revealing the atomic-structure of newly discovered rare-earth-element-free iron-nitride (FeN) magnetic materials. Via atomic-resolution imaging and electron diffraction coupled with *in situ* TEM cooling on LaFeAsO, it was found that additional effects not related to the structural transition, namely dynamical scattering and electron channeling, can give signatures reminiscent of those typically associated with the symmetry change. UEM studies on LaFeAsO revealed direct, real-space imaging of the emergence and evolution of acoustic phonons and resolved dispersion behavior during propagation and scattering.

Via UEM bright-field imaging, megahertz vibrational frequencies were observed upon laser-illumination in TEM specimens made out of HAMR devices which could be detrimental to their long-term thermal and structural reliability. Compression testing of 100-350 nm single-crystal MgO nanocubes shows size-dependent stresses and engineering strains of 4-13.8 GPa and 0.046-0.221 respectively at the first signs of yield accompanied by an absence of brittle fracture, which is a significant increase in plasticity of a brittle ceramic material. Atomic-scale characterization of FeN phases show that it is possible to detect interstitial locations of low atomic-number nitrogen atoms in iron

crystal and hints at a development of novel routes (without involving rare-earth elements) for bulk permanent magnet synthesis.

Captions for Supplementary Videos in Chapter-4

Video S4.1 **Propagating acoustic phonons in a thin [001] oriented LaFeAsO crystal.** The video illustrates a transitory nature of the contrast waves which originates at the vacuum-specimen interface and propagates down towards the thicker specimen regions at the base of the frame. The images were acquired with a 50-kHz repetition rate and a 10-s integration time per frame. The video illustrates dynamics at 1-ps steps spanning -35 to 340 ps (376 total frames) and plays at 60 frames per second (fps) (i.e., dynamics slowed by 1.7×10^{10} times).

Video S4.2 **Propagating and decaying acoustic phonons in a thin [001] oriented LaFeAsO crystal.** The video illustrates a transitory nature of the contrast waves which originates at the vacuum-specimen interface and propagates down towards the thicker specimen regions at the base of the frame. The contrast waves seem to scatter and vanish after 500-ps in the thicker specimen regions at the base of the frame. The images were acquired with a 50-kHz repetition rate and a 15-s integration time per frame. The video illustrates dynamics at 1-ps steps spanning -60 to 689 ps (750 total frames) and plays at 60 frames per second (fps) (i.e., dynamics slowed by 1.7×10^{10} times).

Video S4.3 **Propagating acoustic phonons in a thin [100] oriented LaFeAsO crystal.** The video illustrates a transitory nature of the contrast waves which originates in the top-central and propagates towards the upper-left portions of the specimen. The images were acquired with a 50-kHz repetition rate and a 12-s integration time per frame. The video illustrates dynamics at 2-ps steps spanning -200 to 600 ps (401 total frames) and plays at 60 frames per second (fps) (i.e., dynamics slowed by 8.3×10^9 times).

Captions for Supplementary Videos in Chapter-5

Video S5.1 **Real-space dynamics showing the diffraction contrast motion in the sapphire surrounding the gold disk.** The video illustrates dynamics at 1-ns steps spanning -20 to 500 ns (521 total frames) and plays at 20 fps (i.e., dynamics slowed by a factor of 5×10^7). The oscillatory nature of motion in the diffraction contrast is clearly visible. Note that the video is made out of drift-corrected raw images and there is no Gaussian filtering involved.

Video S5.2 **Real-space dynamics showing the diffraction contrast motion in the sapphire surrounding the gold disk.** The video illustrates dynamics at 40 ns steps spanning -1000 to 0 ns (26 total frames) and at 1-ns steps spanning 0 to 2331 ns (2331 total frames), and plays at 60 fps (i.e., dynamics slowed by factors of 4.17×10^5 for negative time-points and by 1.67×10^7 for positive time-points). The oscillatory nature of the diffraction contrast motion is clearly visible. Note that the video is made out of

drift-corrected raw images and there is no Gaussian filtering involved. This video is from a different set of experiment than Video S5.1.

TABLE OF CONTENTS

LIST OF FIGURES

Chapter 1

Introduction

The birth of electron microscopy happened in the first part of 20th century roughly around the same time when the wave character of electrons was under extensive investigation. Soon after de Broglie's hypothesis in 1924 that matter exhibits wave-like behavior, it was proposed that the resolution limit of light microscopes could be surpassed by the microscopes using smaller-wavelength electrons. However, scientists were not sure how to focus electrons, preventing the idea of electron microscopy from turning into reality. In 1932, Knoll and Ruska made a breakthrough and developed the first electron lenses [1]. Since then the field of electron microscopy has advanced from being a proof-of-concept, lab prototype to a commercial instrument routinely used for research purposes around the globe.

Currently, modern electron microscopes can routinely achieve sub-nanometer and even sub-angstrom spatial resolutions with aberration correctors [2-6]. A unique advantage of achieving real and reciprocal space information by manipulating post-specimen electron optics in TEM also enables crystallographic information, similar to information obtained from X-ray scattering techniques, from nanoscale volumes of materials. An integration of complementary spectroscopic techniques – including

electron energy-loss spectroscopy (EELS) and X-ray energy dispersive spectroscopy (XEDS) – with imaging capabilities allows comprehensive atomic-scale characterization of the structure, chemical composition, and electronic properties of materials [7, 8]. Recent advances in electronics, fabrication techniques, and specialized TEM holders have introduced an era of *in situ* electron microscopy where dynamic experiments at video-rate temporal resolutions can be performed directly in the TEM. These include observation of materials under otherwise vacuum-incompatible conditions [9-11] such as liquid and gas phases, allowing direct observation of chemical reactions at atomic-scale [12-15]. In addition, conditions including temperature and pressure control [16-19], electrical biasing, and mechanical deformation [20-22] are also achievable in TEM. However, the temporal resolutions for these *in situ* experiments are still in the millisecond range even with the latest digital-detector technology [14, 23-25].

While millisecond temporal resolutions of state-of-the-art detectors are reasonable to study various atomic-scale phenomenon, there are many intrinsic materials dynamics – including megahertz mechanical oscillations in micro- and nano-structures, terahertz molecular vibrations, phonon transport, electron-phonon coupling, first-order phase transitions, melting, bond rotation, and spin/charge/orbital ordering – occurring on timescales well below 1 nanosecond. In order to probe ultrafast (sub-nanosecond) materials dynamics on nanoscale spatial resolutions, a stroboscopic, time-resolved pump-probe approach employing fast (relativistic) electrons of TEM has been developed [26-40], referred to as ultrafast electron microscopy (UEM) in this document. UEM experiments usually comprise coherent optical excitation (pumping) of a specimen

followed by imaging (probing) with fast TEM electrons. The pump and probe pulses generally have durations of a few hundred femtoseconds, which enable visualization of dynamics relatively slower than this time scale, therefore providing temporal resolutions from few hundred femtoseconds to milliseconds (video-rate) and seconds. The time-delay between pumping and probing is precisely controlled via an optical delay line.

Much of the work contained herein relies on the advances in time-resolved, *in situ*, and aberration-corrected TEM. Using ultrafast and probe-corrected electron microscopy imaging capabilities along with spectroscopy techniques, static and dynamic materials processes are observed as they occur in oxides, iron nitrides and complicated devices. Chapter 2 provides an overview of various techniques and discusses the instruments employed in my research: CTEM, STEM, spectroscopy, UEM, specimen preparation, SEM, nanoindentation, AFM. Chapter 3 demonstrates the effects of multiple scattering and electron channeling on intensity modulation of atomic columns and Bragg spots with crystal thickness in high-angle annular dark-field scanning TEM (HAADF-STEM) images and parallel-beam diffraction (PBED) patterns from tetragonal and orthorhombic LaFeAsO. I demonstrate the thickness-dependent modulation of intensities within the (Fe,O) and (La,As) columns along the [001] zone axis at 300 K and show how reflections arising from the {*100}* planes (forbidden in the *P4/nmm* space group of the tetragonal structure) can be made to appear and disappear by moving to crystal regions of differing thickness, independent of a structural phase transition. Via cryo-TEM and PBED, I further demonstrate the same such effects in the orthorhombic structure (*Cmme*) along the [001] zone axis at 90 K, wherein the intensities of forbidden {*110}* reflections

are shown to be thickness dependent. The results are supported with multislice simulations of atomic-column and Bragg-spot intensities from LaFeAsO.

Chapter 4 examines the ultrafast structural dynamics of tetragonal LaFeAsO and describes preliminary results on real-space phonon propagation and scattering in single-crystals. Real- and reciprocal-space nanosecond dynamics depict megahertz mechanical vibrations. Reciprocal-space femtosecond dynamics require more statistics for any conclusions. Chapter 5 describes the photo-actuation of heat-assisted magnetic recording (HAMR) devices. I report the direct visualization of laser-induced nanoscale megahertz vibrations in these devices. The results are supported with finite element method simulations. Chapter 6 explores the possibility of ductile ceramics at the nanoscale and studies the size-dependent mechanical response of magnesium oxide nanocubes. The results suggest an inverse size dependence of yield stresses and engineering strains and represent an observation of extended plasticity in magnesium oxide single-crystals. Chapter 7 shows the static TEM characterization of iron-nitrogen-carbon compounds which are potential candidates to replace permanent magnets made out of rare-earth elements. A discovery of a new phase is also reported.

Chapter 2

Methods and Equipment

This chapter gives an overview of the various techniques and equipment used for the work reported in the following chapters. When necessary, additional descriptions of experimental parameters specific to work reported in a particular chapter will be given in the corresponding chapter. For more details of the techniques, standard textbooks can be consulted [7, 41-43].

2.1 Conventional Transmission Electron Microscopy

In conventional transmission electron microscopy (CTEM), electrons originating at the electron source, i.e., gun system, are guided to the specimen such that a coherent and collimated beam of electrons passes through the specimen. The transmitted electrons are collected using an objective lens and a system of projection lenses. Figure 2.1(a) shows the relative positions in a TEM column of an electron source, a condenser system to guide the electrons to the specimen, an objective system to form a CTEM image or diffraction pattern, and a projection system to change magnification.

CTEM is analogous to various optical microscopy modes where a parallel beam of light illuminates the specimen, and the corresponding images or diffraction pattern are recorded in parallel. But CTEM takes the advantage of the fast (relativistic) electrons with picometer wavelengths and therefore has resolution on the order of few angstroms

which is not achievable with optical microscopy due to its diffraction limit. In the following chapters, an FEI Tecnai G2 F30 (S)TEM, an FEI Tecnai G2 F30 Cryo (S)TEM, an FEI Tecnai T12 TEM, and an FEI Tecnai Femto UEM were used for CTEM imaging and diffraction.

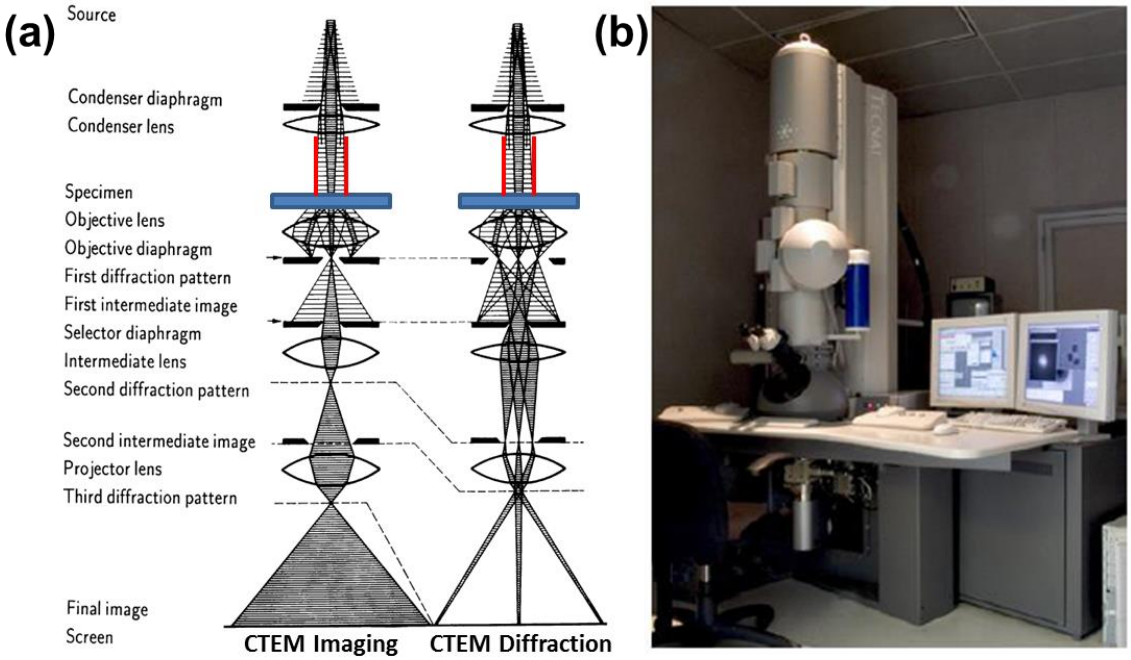

Figure 2.1 (a) Schematics for CTEM imaging and selected-area diffraction modes. Adpated from ref [41]. (b) A picture of the FEI Tecnai G2 F30 (S)TEM at the Shepherd Labs, UMN characterization facilities.

2.1.1 Imaging in CTEM.

The transmitted beam through the specimen, centered on the objective diaphragm (or aperture), produces bright-field CTEM images (Figure 2.1(a)). The resulting bright-field CTEM images have mass-thickness, diffraction, and phase contrast. When a smaller

objective aperture is used to select the non-diffracted central beam, the aperture excludes diffracted electrons and leads to strong mass-thickness contrast. In the present work, bright-field CTEM imaging has been extensively used. Figure 2.2 shows a high-resolution CTEM image acquired with FEI Tecnai G2 F30 (S)TEM without an objective aperture and therefore has mass-thickness, diffraction, and phase contrast in it. Note that the objective aperture is present in the back focal plane of the objective lens where the diffraction spots are formed. When the non-diffracted central beam is excluded with an objective aperture, a dark-field CTEM image with both mass-thickness and diffraction contrast contributions is formed. Selection of a diffraction spot with the objective aperture allows only diffraction-contrast contributions and is useful for grain mapping and defect characterization in crystalline materials.

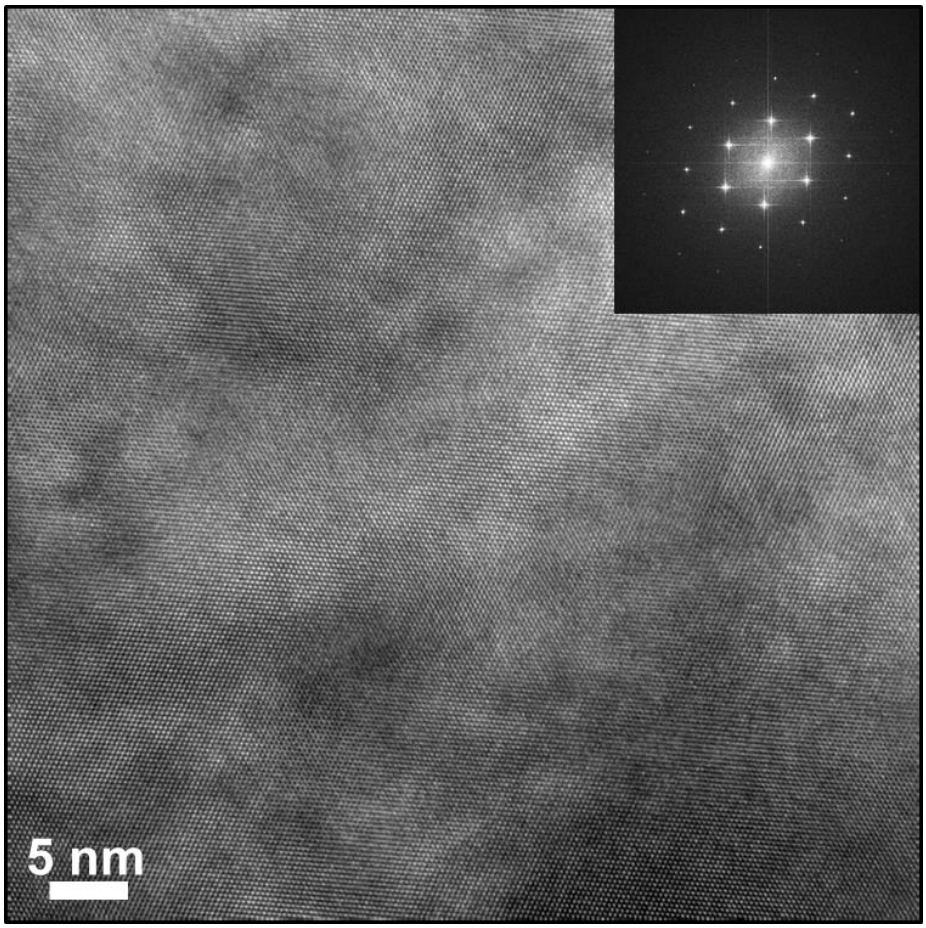

Figure 2.2 A high-resolution CTEM image of [110]-oriented silicon single-crystal prepared by mechanical wedge polishing. Inset shows the FFT of the image.

2.1.2 Diffraction in CTEM.

Diffraction patterns in the CTEM mode provide information about the crystal structure of the specimen. Electron diffraction in TEM is analogous to X-ray diffraction for structural characterization of crystalline materials. Figure 2.3 shows representative electron diffraction patterns from both polycrystalline and single-crystalline specimens.

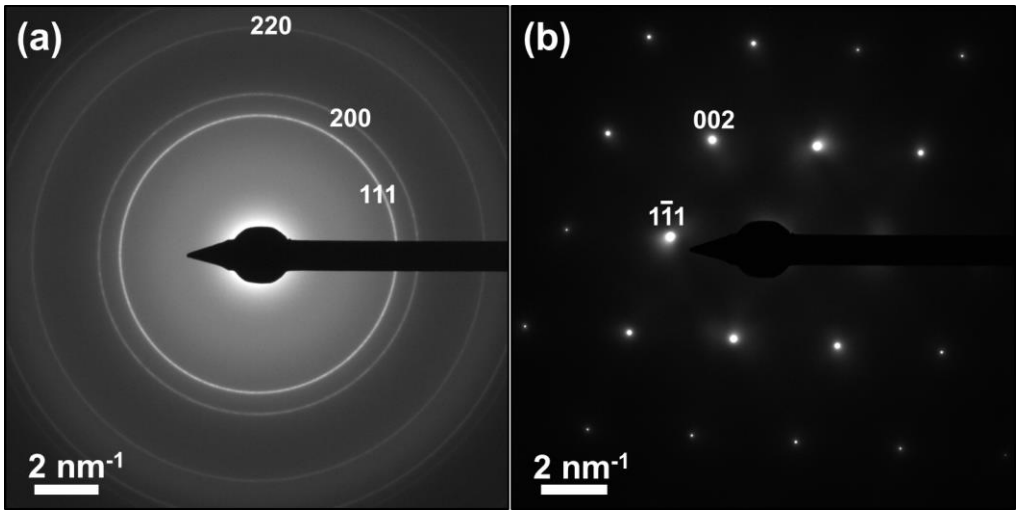

Figure 2.3 (a) A CTEM diffraction pattern from polycrystalline aluminium prepared by DC magnetron sputtering. Sample courtesy of Daniel Cremons. (b) A CTEM diffraction pattern from [110]-oriented silicon single-crystal prepared by mechanical wedge polishing.

Using the selected-area (SA) aperture, located in the first image plane and after the back focal plane of the objective lens, crystal structure information from localized regions of the specimen can be obtained by excluding rays originating from regions outside the aperture. However, the smallest regions of interest that can be selected with SA apertures are roughly 300 nm in the microscopes at the University of Minnesota. Therefore, convergent beam electron diffraction (CBED) can be employed to collect diffraction information that is more spatially localized than the selected-area diffraction. In CBED, the electron beam is converged on a region of interest in the specimen leading to a spreading of the central and diffracted spots into disks proportional to the

convergence angle of the incident beam. Overlap of diffraction disks may occur for higher convergence angles and/or smaller reciprocal lattice vectors.

2.2 Scanning Transmission Electron Microscopy

In scanning transmission electron microscopy (STEM) mode, a combination of condenser and upper-objective lenses focus the electron beam into a small, coherent probe with a full width at half maximum (FWHM) on the order of an angstrom (Figure 2.4(a)). With the help of scan coils shown in Figure 2.4(a), the probe is rastered across a region of interest to form the images. Images can then be formed in a serial manner from the various signals produced at each point in the scan area. The signals from specimen include the direct electrons resulting in a bright-field STEM image, low-angle-scattered electrons creating a dark-field diffraction contrast image, high-angle scattered electrons to form a high-angle dark-field image, inelastically scattered electrons to form an electron energy-loss spectrum, and generated X-rays to produce an X-ray energy-dispersive spectrum. In the following chapters, an FEI Tecnai G2 F30 (S)TEM and an FEI Titan G2 60-300 (S)TEM were used for STEM imaging.

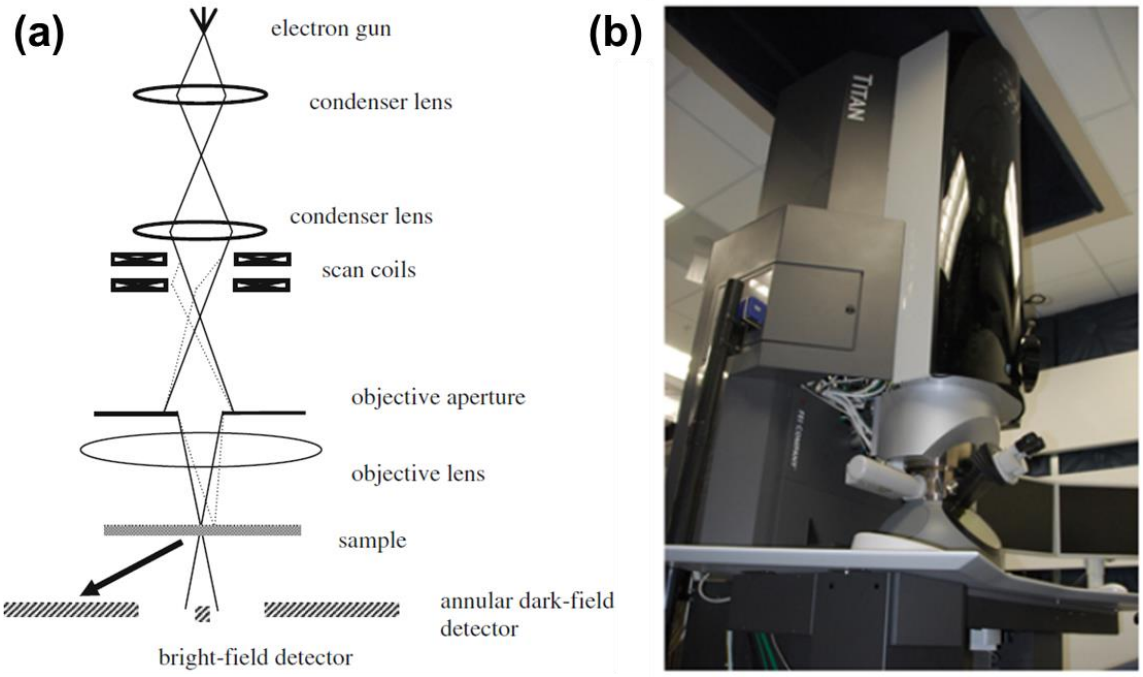

Figure 2.4 (a) A schematic of the STEM imaging mode. Adapted from ref [42]. (b) A picture of the FEI Titan G2 60-300 (S)TEM at the Shepherd Labs, UMN characterization facilities.

2.2.1 Bright-Field and Annular Dark-Field STEM.

The STEM imaging mode can be classified into bright-field (BF) and annular dark-field (ADF) imaging. Both BF and ADF detectors are located in a conjugate plane to the back focal plane to intercept the direct and scattered electrons from the diffraction patterns (Figure 2.5(a)). Since BF-STEM mainly uses the direct electrons, the image contrast thus mimics that of CTEM image. ADF-STEM utilizes a detector with inner and outer collection angles such that Bragg scattered electrons are collected. Consequently, gold particles diffracting the electron beam appear dark in the BF-STEM image in Figure

2.5(b) whereas the same particles appear bright in a simultaneously acquired ADF-STEM image in Figure 2.5(c). The ADF-STEM images, when acquired at collection angles of typically 54-300 milli-radian (mrad), are often referred as *Z*-contrast or high-angle ADF (HAADF) images since the elastic scattering intensity depends on powers of the atomic number such as found in Rutherford scattering, $I \propto Z^{1.5}$–Z^2 [42]. In the present work, FEI Titan G2 60-300 (S)TEM and FEI Tecnai G2 F30 (S)TEM were used for BF-STEM and ADF-STEM imaging.

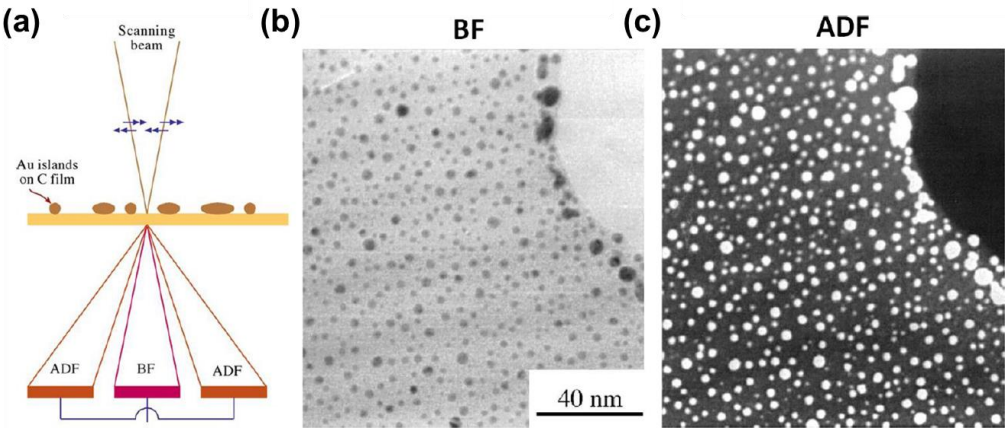

Figure 2.5 (a) A schematic showing the detector locations in the STEM imaging mode. (b) Bright-field (BF) and (c) annular dark-field (ADF) images of gold particles acquired simultaneously in the STEM mode. Adapted from ref [7].

2.2.2 Aberration-Correction.

For the high-energy, relativistic electrons of a TEM with wavelengths of 2–5 pm, theoretically a spatial resolution of less than 10 pm can be achieved. However in conventional electron microscopes, achieving this diffraction-limited resolution is

prevented by aberrations induced by imperfect lenses and incoherent electron sources. The inability of electromagnetic lenses to focus rays of different axial positions to the same point causes a point object to be imaged as a disk of finite size and is referred to as spherical aberration. In conventional electron microscopes, which exhibit significant spherical aberration, an optimal resolution of 150 pm or greater is obtained at a convergence angle of approximately 10 mrad.

In the past twenty years, the development of spherical aberration correctors has significantly improved the resolution of TEM. As a result, diffraction-limited imaging is possible out to convergence angles of 30 mrad and larger, and now it is routinely possible to image sub-angstrom features. To date, resolution below 50 pm has been demonstrated in STEM imaging [5]. Figure 2.6 shows how with aberration-correction the neighboring atomic-columns in [110] oriented silicon dumbbells could be resolved [44]. In the present study, a spherical aberration-corrected FEI Titan G2 60-300 (S)TEM was used for atomic-resolution STEM imaging.

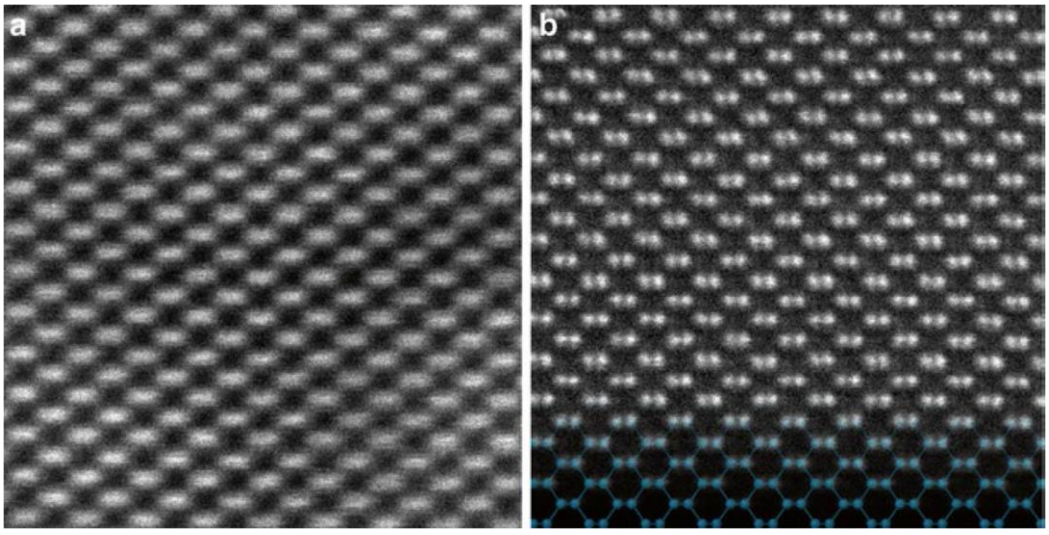

Figure 2.6 (a) A non-aberration-corrected and (b) an aberration-corrected STEM image of silicon dumbbells along [110] crystal orientation. The distance between two silicon atoms in a dumbbell is 1.36 Å. Adapted from ref [44].

2.3 Spectroscopy

Spectroscopy in conjunction with imaging in TEM provides useful information about material composition, thickness, bonding, etc. Carrying out spectroscopy and imaging simultaneously is often referred to as analytical electron microscopy [7]. In the present work, two spectroscopy techniques – electron energy-loss spectroscopy and X-ray energy dispersive spectroscopy – were used.

2.3.1 Electron Energy-Loss Spectroscopy (EELS).

When high-energy electrons pass through a specimen, they lose energy inelastically by exciting various electronic transitions in the specimen. In EELS, these inelastically scattered electrons transmitted through the specimen are dispersed with magnetic prisms to different angles depending on their energy loss, which are then magnified and detected by a CCD. Since inelastically scattered electrons are predominantly in the forward direction whereas ADF-STEM signal falls on an annular detector, it is possible to collect ADF-STEM images and EELS spectra simultaneously. Figure 2.7 shows a schematic of ADF-STEM imaging and EELS acquisition in parallel.

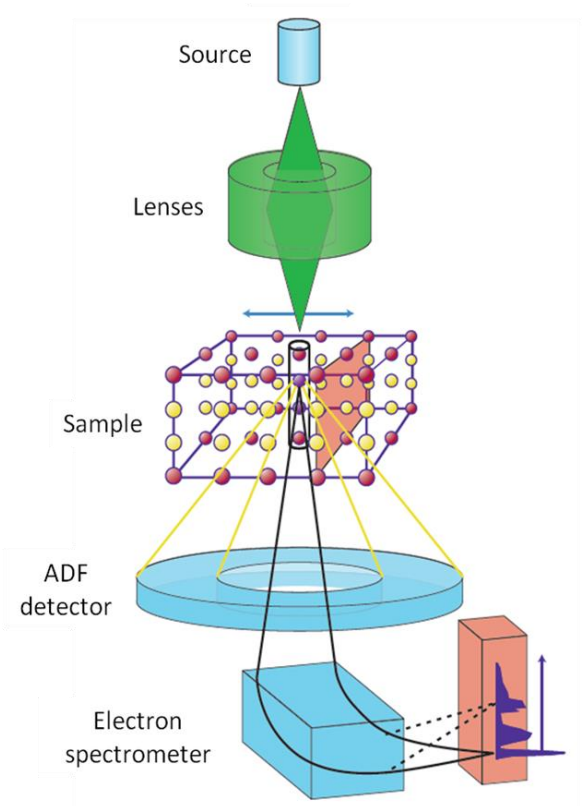

Figure 2.7 A schematic showing analytical STEM-EELS capability. Adapted from ref [45].

The zero-loss peak in EEL spectra contains direct beam electrons and therefore reflects the energy resolution of the electron source and magnetic prism. The low-loss spectrum from 0-50 eV is due to weakly bound outer-shell excitations and predominantly features plasmon-loss and valence-to-conduction interband transitions. From the low-loss spectrum, the local specimen thickness, local dielectric constant, band gap, and band structure can be derived. The core-loss spectrum above 50 eV results from core electron excitations to states above the Fermi level. These transitions are used to determine elemental compositions and coordination states. In the present work, low-loss EELS was

used to determine local specimen thicknesses, and core-loss EELS was used for elemental mapping. In the present work, a Gatan Enfinium spectrometer was used in FEI Titan G2 60-300 (S)TEM and a Gatan Enfina spectrometer was used in FEI Tecnai G2 F30 (S)TEM.

2.3.2 X-ray Energy Dispersive Spectroscopy (XEDS).

The incident electron beam excites electrons from the inner shell of atoms, creating a hole that can be relaxed by emission of Auger electrons or secondary X-rays. In XEDS, secondary X-rays, characteristic of an element, are detected using XEDS detector systems. In the present work, a Super-X detector system was used in FEI Titan G2 60-300 (S)TEM, a rTEM EDAX detector system was used in FEI Tecnai G2 F30 (S)TEM, and an Oxford Inca system was used in FEI Tecnai T12 TEM.

2.4 Ultrafast Electron Microscopy

Ultrafast electron microscopy (UEM), established in the last decade, combines the concept of pump-probe femtosecond spectroscopy with the relativistic electrons of TEM [31, 32, 34, 46, 47] and is currently operating in handful of places in the world including the Flannigan group at the University of Minnesota, the Zewail group at the California Institute of Technology, the Carbone group at the École polytechnique fédérale de Lausanne in Switzerland, the Ropers group at the University of Göttingen in Germany, the Banhart group at the University of Strasbourg in France, the Institute of Physics at the Chinese Academy of Sciences in China, and the Tanimura group at the Osaka University in Japan. Several other research institutions and groups including the van der Veen group

at the University of Illinois at Urbana Champaign, the Ortalan group at the Purdue University, the Ruan group at the Michigan State University, and the Yurtsever group at the Institut National de la Recherche Scientifique in Canada are attempting to build their own UEM lab. Therefore, this technique is described in a little more detail in this chapter than the other state-of-the-art electron microscopy and characterization techniques, and the equipment details in this chapter are mostly specific to the UEM lab in the University of Minnesota. The concept of UEM is universal.

From Figure 2.8, it can be seen that a FEI Tecnai Femto UEM is positioned right next to an optical table. The optical table is a research-grade Newport optical table with four-point tuned damping and has dimension 4 feet × 8 feet × 24 inches. Both the microscope and optical table rest on a vibration isolation slab that is completely decoupled from the building. This is necessary for accurately studying the atomic-scale phenomenon on sub-picosecond timescale and decoupling the intrinsic materials dynamics from various external noises.

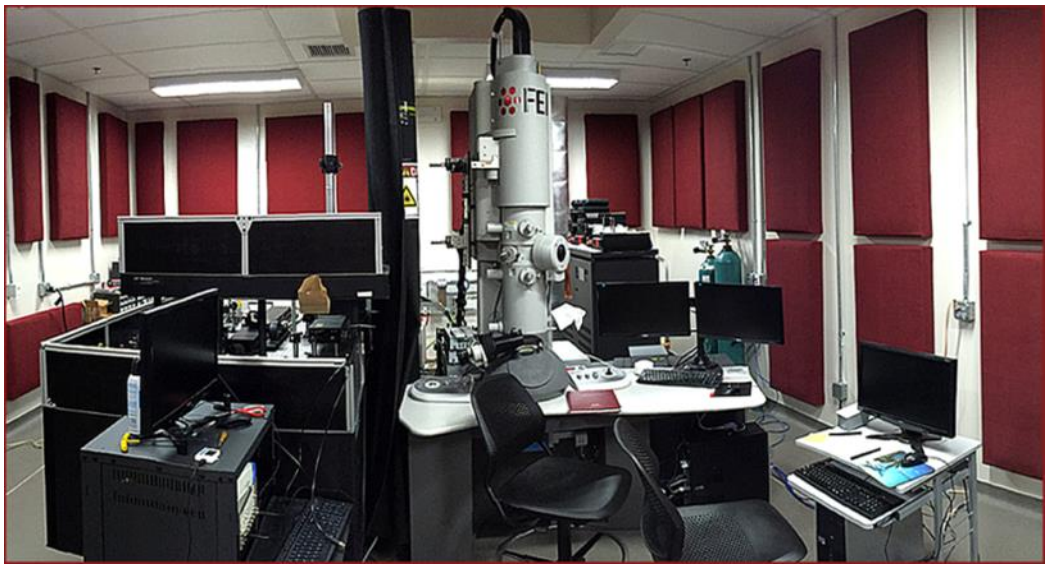

Figure 2.8 A picture of the UEM lab at the University of Minnesota. A FEI Tecnai Femto UEM (right side in the picture) and LASER systems on a Newport optical table (left side in the picture) constitute a major portion of the UEM apparatus.

In UEM, potentially all the imaging and diffraction signals from the CTEM mode are available for the time-resolved investigations. Currently spectroscopy capabilities are not available in the UEM lab at the University of Minnesota. Image acquisitions are exactly similar to routine CTEM acquisitions with a Gatan Orius SC200B video-rate CCD camera, except photoelectron packets (generated from LaB_6 filament upon pulsed laser excitation) are used and the image acquisition time is usually 2-10 times higher than that for a normal thermionic CTEM acquisition due to a lower electron beam intensity originating from the pulsed nature of probing laser. Figure 2.9(a) shows the optical ports for the entry of the pump and probe-extracting pulses in the microscope. Probe-extracting photon pulses go to the LaB_6 filament and extract photoelectrons. Note that in

the UEM experiments, the LaB_6 filament is not heated from external power supply (like CTEM operation); therefore, all the probing electrons are generated with pulsed excitation, and the time-delay between pump and probe pulses is precisely controlled with an optical delay line (Figure 2.9(b)).

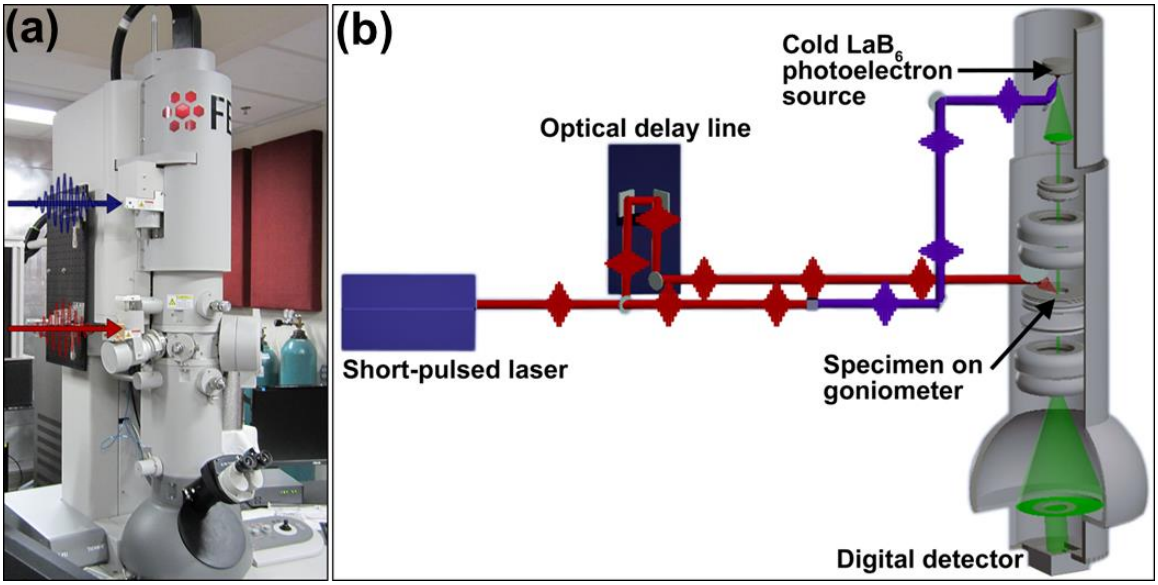

Figure 2.9 (a) A FEI Tecnai Femto UEM at the University of Minnesota. The points of entry of the probe and the pump pulses are highlighted by blue and red arrows, respectively. (b) Simplified schematic of the UEM experimental layout. Several critical pieces of equipment and points of interest are labelled. Adapted from ref [46].

The optical delay line comprises a Newport broadband retroreflector attached to an Aerotech linear motorized translation stage which can potentially cover 270 fs to 6.7 ns temporal range with a 1 meter travel range. The experiments performed in this temporal regime have been referred to as femtosecond UEM experiments. In addition to

the motorized stage with a retroreflector, the delay line also consists of a wide range of optics on the table. To cover from 700 ps to video-rate temporal regime, a nanosecond laser is used, and all the experiments in this time regime have been referred to as nanosecond UEM experiments. The optical delay line for nanosecond experiments does not employ the movement of motorized delay stage but comprises a digital delay generator to precisely control the time delays between pump and probe pulses. Figure 2.10 summarizes the layout of the optical table for both femtosecond and nanosecond UEM experiments.

For both nanosecond and femtosecond UEM experiments, a Yb:KGW (1030-nm fundamental output), diode-pumped, solid-state Light Conversion PHAROS laser and a custom Light Conversion HIRO harmonics generation module were used to generate the pump pulses. The HIRO harmonics generation module takes the fundamental output of PHAROS and generates second and third harmonics. In femtosecond experiments, to generate the probing photoelectron packets, the pump line is split, and a portion of the 515-nm pulses was frequency doubled to 257.5-nm and focused into the gun region of the microscope. For nanosecond experiments, probe-extraction pulses were generated with a Nd:YAG (1064-nm fundamental output), Q-switched, diode-pumped, solid-state laser. The fourth harmonic was generated on the laser table with frequency-doubling BBO crystals and was used to generate the photoelectrons out of the LaB_6 cathode for image formation. A custom Newport breadboard is used for delivering light from laser table to the pump and probe optical ports in the microscope. For nanosecond experiments, the pump line is kept constant, and a delay in probe line via digital delay generator dictates

the time delay of the experiments. On the other hand, in femtosecond experiments, the probe line is kept constant, and a delay in pump line via a precise movement of the motorized translation stage controls the time delays.

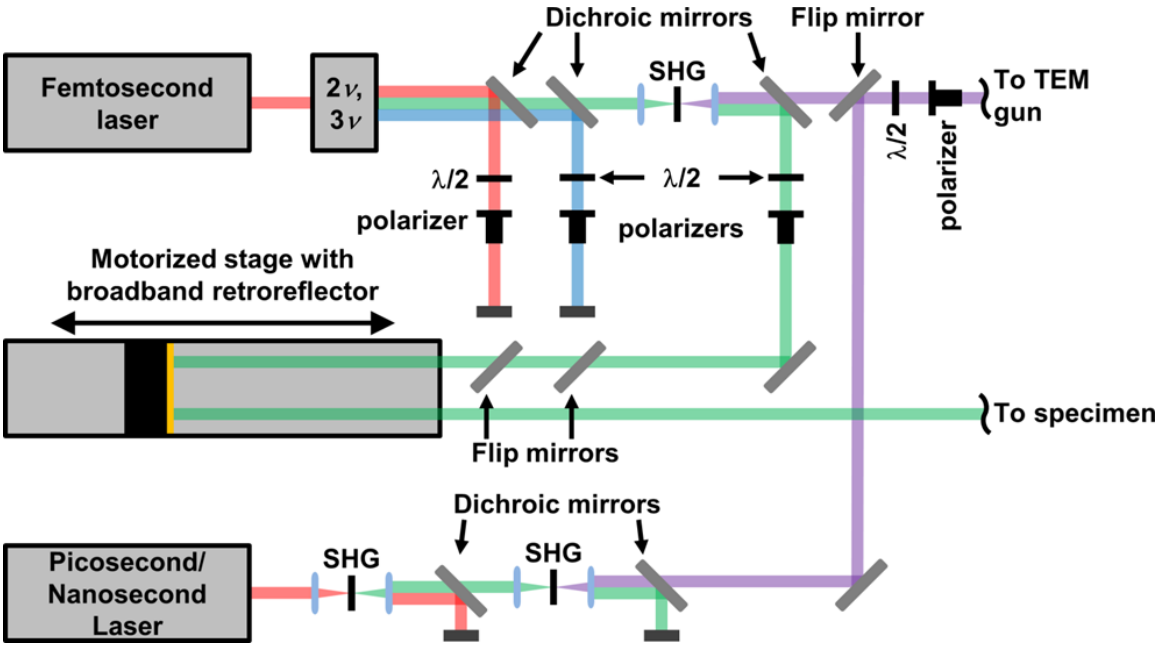

Figure 2.10 A schematic showing the layout of LASER systems, motorized stage, and non-linear optics mounted on the optical table. Red beams originating from the femtosecond and nanosecond lasers are their fundamental output (1030-nm for femtosecond and 1064-nm for nanosecond). Green, blue and violent beams are respectively the second, third and fourth harmonics of the fundamental output generated on the optical table. Figure courtesy of Professor David Flannigan.

With UEM, it is possible to reach far below the conventional limits of imaging to only a few hundreds of femtoseconds (i.e., 10^{-15} seconds, the timescale of atomic bond

vibrations). This is accomplished using a pump-and-probe approach in which the time-dependent behavior is initiated with a change-inducing agent (the pump; e.g., a laser pulse) and subsequently followed with an imaging agent (the probe; e.g., short-wavelength electron packets). Analogous to a strobe light, the electron packets in the pump-and-probe approach act as a very brief flash of illumination to capture snapshots only a few hundred femtoseconds apart. This equates to having the ability to capture more than 10^{13} frames per second. The imaging component in UEM is realized by applying the pump-and-probe approach with a transmission electron microscope and acquiring the images with the standard CCD cameras by building the image signal-to-noise over the multiple frames and integration times of usually a few seconds, as shown in Figure 2.11. After sufficient image signal-to-noise is achieved, the time-delay is changed. An image acquisition time depends on the numbers of electrons contained in a probing photoelectron packet, i.e., the repetition-rate of the experiment and pulse-width of the probing electon packet, and the number of photoelectrons scattered off the TEM specimen, i.e., dependent on specimen thickness. Therefore, a higher repetition-rate and a 'thin' TEM specimen are usually ideal for a lower UEM image acquisition time. But at higher repetition-rates, the specimen may not have time to thermally and mechanically relax to its ground state before the arrival of the next pulse. Therefore, choosing a repetition-rate that is suitable for an UEM experiment is highly dependent on the intrinsic thermal, optical, and mechanical properties of the specimen and its boundary conditions (e.g., type of TEM grid used) which dictate the thermal relaxation.

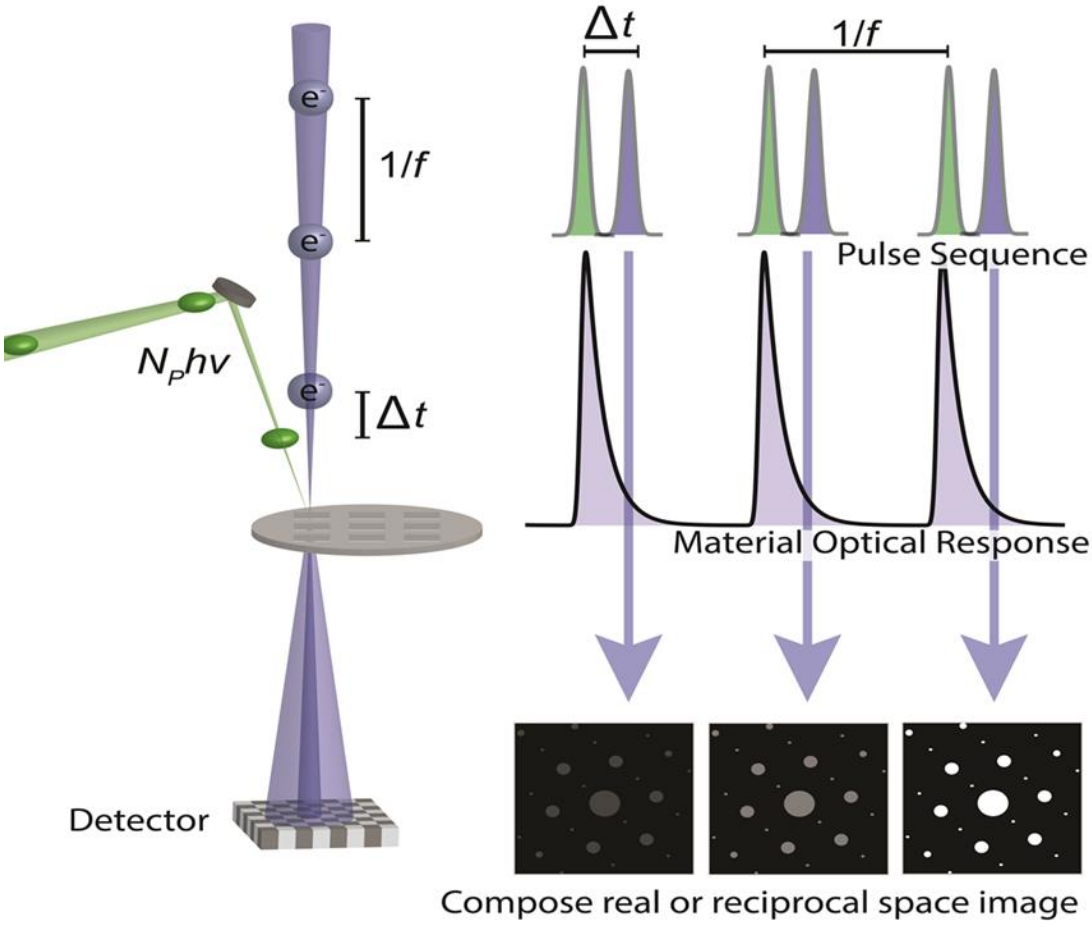

Figure 2.11 A schematic representing the image acquisition concept in UEM. Pumping photons and probing photoelectrons are shown in green and violet, respectively. f is the repetition-rate of pump and probe lasers used in an experiment, and Δt is a time-delay between the pump (photon) and the probe (photoelectron) pulses. Figure courtesy of Dr. David Valley.

The stroboscopic image acquisition concept in UEM allows visualization of reversible materials dynamics up to few hundreds of femtoseconds. This mode is often referred to as stroboscopic imaging mode and usually contains 1 to 10^3 electrons in a

photoelectron packet as shown in Figure 2.12 [48]. Imaging irreversible materials phenomenon is also possible with UEM but in a different mode referred as single-shot (Figure 2.12) [46, 48]. However, the temporal resolutions achievable in the single-shot mode are currently up to nanoseconds. Using both stroboscopic and single-shot modes could provide a comprehensive view of the structural dynamics of materials. In the present work, only stroboscopic UEM mode has been used.

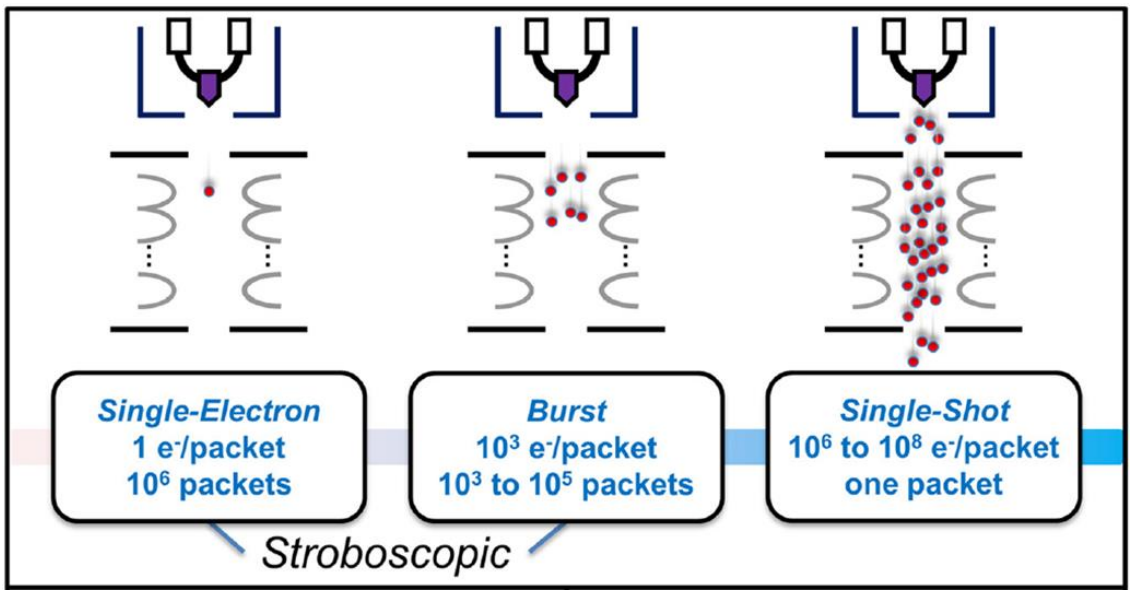

Figure 2.12 A schematic showing the three distinct modes of UEM operation and their corresponding parameters. Adapted from ref [48].

2.5 Specimen Preparation Techniques

2.5.1 Focused Ion Beam.

Specimen preparation is an integral part of conducting high-quality electron microscopy research. In the present work, focused ion beam (FIB) machining was used to a great extent. LaFeAsO and iron-nitride specimens obtained for the present studies were bulk crystals on the order of few millimeters in width and height and a thickness of approximately 100 μm. Therefore, a unique approach was adopted as summarized in Figure 2.13 where bulk crystals were directly attached to a TEM grid and were polished in the FIB. After attaching the bulk crystals to the TEM grids with silver epoxy, they were cured for 2-3 hours on a hot plate at 100 ºC or were left at room temperature for at least a day. This allowed for a nearly permanent attachment of crystals to the TEM grid.

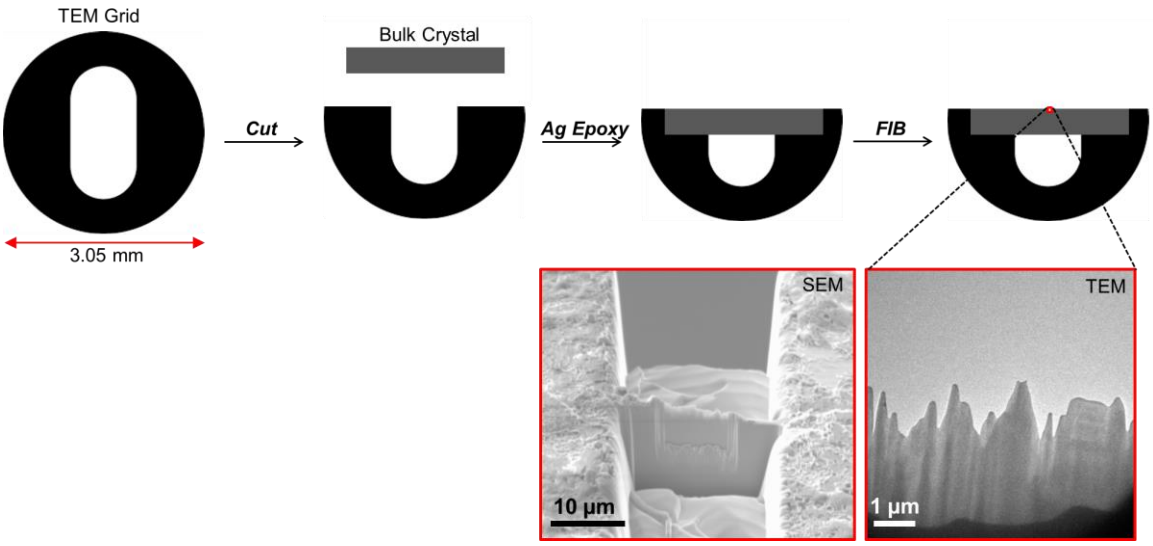

Figure 2.13 A schematic showing the TEM specimen preparation via FIB to make electron transparent regions in bulk crystals without lifting-out the specimen with Omniprobe® micromanipulator. The resulting SEM and TEM images of an electron region are also shown.

On multiple occasions when iron-nitride specimens had thicknesses of few millimeters and were irregular shaped (other than close to rectangular), a standard FIB lift-out approach shown in Figure 2.14 was adopted where Omniprobe® micromanipulator was used to lift the lamella out of the bulk crystals and attach them to TEM grids. This approach was very useful for the iron-nitride specimens because their magnetic nature severely deflected the TEM electron beam when the specimen approach described in Figure 2.13 was used. The lift-out approach was also useful for preparing LaFeAsO specimens with crystal orientations other than their original [001] orientation.

LaFeAsO crystals obtained from the collaborators at Oak Ridge National Lab had [001] orientation perpendicular to the plane of paper, therefore the approach shown in Figure 2.13 was useful to get [001] oriented TEM specimens. To get [100] oriented LaFeAsO specimens with similar boundary conditions (i.e., clamped on three sides and free on the fourth side) as that of [001] oriented LaFeAsO specimens prepared via non-lift-out FIB approach, an additional step is proposed. It would be useful to cut the crystals along their edges followed by careful flipping and attachment such that [100] crystal orientation is perpendicular to TEM grid plane. After this step, the usual FIB protocol shown in Figure 2.13 could be used. This would be useful to compare the ultrafast structural dynamics of [001] and [100] oriented LaFeAsO in future.

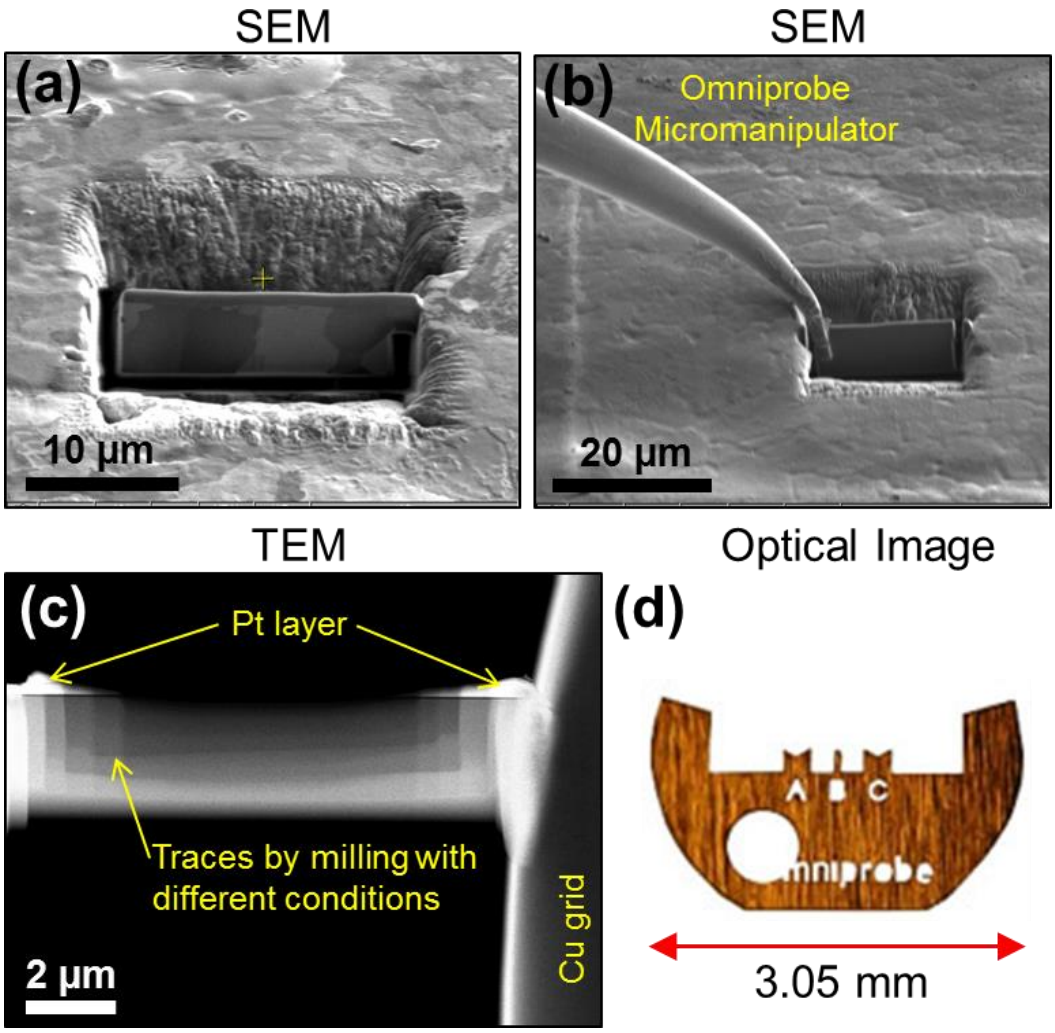

Figure 2.14 (a) A SEM image of lamella prepared via FIB in a bulk crystal. The contrast in the lamella is due to grain boundaries. (b) A SEM image showing a lift-out of lamella with Omniprobe® micromanipulator. Platinum welding via gallium ion beam was employed to attach micromanipulator to the lamella. (c) A TEM image of a lamella after final polishing and attached to a Omniprobe® lift-out copper TEM grid with three posts. The contrast in the lamella is due to a variable specimen thickness in the centre and on the sides. (d) An optical image of the Omniprobe® lift-out copper TEM grid. In the present work, all the lamellae were attached to the central post indexed as B.

2.5.2 Mechanical Wedge Polishing.

The wedge-polishing technique is described in detail by Voyles *et al.* [49]. This method is useful to examine specimen cross-sections of thin films, hetero-structures, bulk crystals whose substrates could be well-bonded to a glass polishing stub. An Allied Multiprep™ Polishing System was used. Samples are cleaved into small sections of nearly 1 cm × 1 cm, and two small sections are glued together using M-Bond™. The glue-line thickness should be minimized to ensure mechanical stability of the sample during polishing, and this is achieved by applying an external pressure using a custom made spring-loaded clamping system. The clamping system is then placed in a vacuum oven at 100 ºC for 1 hour to cure the glue. The specimen is then attached to microscope slide using Crystalbond™ wax. The specimen is cut into small pieces about 2 mm × 2 mm with a dicing saw and then attached to a glass stub with Crystalbond™ wax. The specimen is then polished on both sides as described by Voyles *et al.* [49]. Once the specimen is sufficiently thin, optical fringes could be seen at the edges as shown in Figure 2.15(b), which suggest that polishing could be stopped. After finishing the second side polishing, the polished specimen attached to glass stub is glued using M-Bond to a slot copper TEM grid as shown in Figure 2.15(a) and then cured in the vacuum oven for 1 hour at 100 ºC. After curing, the whole assembly shown in Figure 2.15(a) could be detached from glass stub by immersing it in acetone for 5-10 minutes. Finally, a wedge-polished specimen attached to TEM grid is ready to use in TEM.

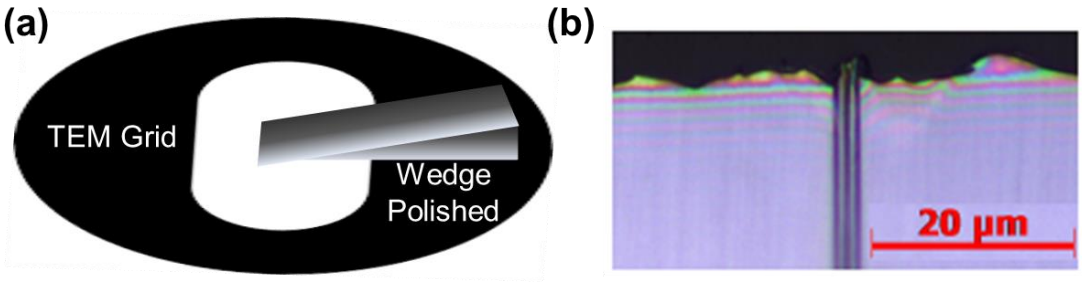

Figure 2.15 (a) A schematic of a wedge-polished specimen attached to a slot copper TEM grid having 1 mm × 2 mm slot dimensions. (b) An optical image of a silicon wedge (having silicon dioxide at the interface running vertically) after final polishing. Note the presence of optical fringes at the edge of wedge, which hints a 'thin' electron transparent region.

2.5.3 Drop-Casting.

This technique was used for depositing MgO nanocubes and iron-nitide nanoparticles on substrates and TEM grids. The nanoparticles are mixed in organic solutions (e.g., isopropanol, ethanol, and propanol) which are non-reactive to the particles. Then the whole solution was ultra-sonicated for 30-120 minutes to detach the agglomerated particles. Finally, using a thin hypoderm needle few drops of ultrasonicated solution was immediately dropped on substrates or TEM grids, which were left to dry in ambient conditions.

2.5.4 Direct Deposition of Nanoparticles.

MgO nanocubes synthesized by burning Mg turnings were sometimes directly deposited onto TEM grids or sapphire substrates by letting them face the burning plume.

At some occasions, the collected dry smoke or dry nanoparticles in a vial were scraped with a sharp needle and then sprinkled onto the TEM grids and substrates.

2.6 Scanning Electron Microscopy

SEM produces images of a specimen by scanning a focused beam of electrons. Electron beam interaction with the specimen produces various signals including secondary electron (SE), back-scattered electron (BSE), and X-rays. SE signals are especially useful for determining the specimen surface topography. SEM images are produced by combining the electron beam position with the detected signals and can reveal details less than 1 nm in size. SEMs are frequently interfaced with XEDS for investigating the chemical composition of the specimen. A major advantage of SEM over TEM is that it does not require a preparation of electron transparent specimens but it can only probe the surface properties. In the present study, JEOL 6500 and 6700 FEG SEMs were used in SE mode along with XEDS whenever required.

2.7 Nanoindentation

Indentation testing is a method that consists of touching the materials of interest whose mechanical properties, such as elastic modulus and hardness, are unknown with another material whose properties are known [43]. Mechanical characterization of nanoscale volumes is based on nanoindentation. The prefix “nano” in nanoindentation refers to the fact that the length scale of the indenter penetration is on the order of nanometers. Figure 2.16(a) represents a schematic of nanoindentation for a bulk sample

and for a cube on substrate. Indenters, generally made up of the hardest-known material, diamond, and having different geometries with varying radius of curvature (r_{tip}), are used according to experimental needs.

A Hysitron Triboindenter® in the UMN Characterization Facility (Figure 2.16(c)) was used to perform nanoindentation, which is referred to as *ex-situ* indentation because the facility of simultaneously capturing images and load-displacement data is not available. It consists of an optical microscope, a piezoelectric XYZ scanner, a translating stage, and a 2-dimensional (2D) transducer. The TriboIndenter® uses top-down optics with a maximum resolution of 50 μm to locate areas of interest on the sample. The indentation location can be further refined using the TriboIndenter® scanner, which is controlled by piezoelectric ceramics and allows placement of indents within ±20 nm. The scanner can be also used to image the surface topography similar to scanning probe microscopy. The resolution, however, is limited by the sharpness of the indenter tip. The indentation is performed using a high voltage, parallel plate transducer. The load-displacement curves can be generated using load or displacement feedback control. Nanoindentation allows for observation of events during testing, such as formation of cracks and nucleation of discrete numbers of dislocations. These events correspond to load drops in displacement feedback control and displacement jumps in load feedback control. Figure 2.16(b) shows a representative load-displacement curve in the load feedback control on bulk (100) MgO. After reaching the applied maximum load P_{max} or displacement δ_{max}, the diamond tip retraces back and follows the unloading segment of the load-displacement curve leaving a residual displacement in the sample. The

unloading slope can be analyzed using the Oliver-Pharr method [43, 50, 51] based on Hertzian contacts in order to calculate hardness and elastic modulus.

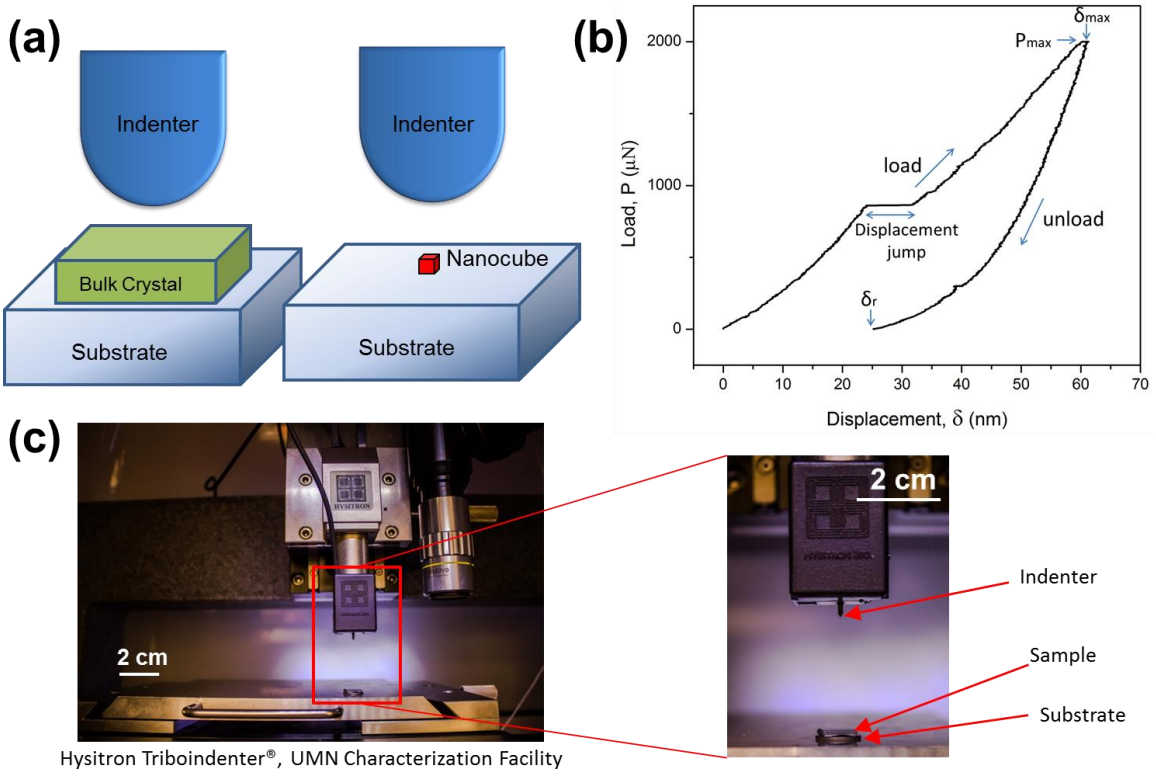

Figure 2.16 (a) A schematic showing the layout of nanoindentation experiment for bulk crystal and nanocube. (b) A representative load-displacement plot from a bulk MgO crystal in a load feedback control mode. P_{max} is the maximum load applied, δ_{max} is the displacement of the indenter in the crystal at P_{max} and δ_r is the residual displacement in the crystal after unloading of the indenter. (c) A close-up view of the Hysitron Triboindenter® showing the experimental stage and the transducer for load-displacement measurements. Red rectangle highlights the indenter and the sample attached to a magnetic substrate with epoxy.

2.8 Atomic Force Microscopy

Atomic force microscopy is a method to see the shape of a surface in three dimensional (3D) details down to the nanometer scale [52]. The surface morphology is determined by measuring surface height at each point or pixel within a 2D array over the surface using a sharp solid force probe. In the present project AFM was utilized for comparing the surface morphology of nanocubes before and after *ex-situ* indentation.

Chapter 3

Effects of Dynamical Scattering on Atomic-Resolution TEM Images and Electron Diffraction Patterns of Orthorhombic and Tetragonal LaFeAsO

3.1 Introduction

Observation of superconductivity in the iron pnictides [*e.g.*, $LaFeAsO_{1-x}F_x$] opened a new avenue to study high-temperature superconductors [53-55]. Indeed, the normal states of the undoped parent compounds (*e.g.*, LaFeAsO), have received much attention owing to the possibility that understanding their properties may shed light on the superconducting state [56, 57]. Inspection of the general temperature-composition phase diagram of the iron pnictides reveals the suppression of both a structural and a magnetic phase-transition temperature with increased electron doping of the parent compound [55, 58-61]. For example, for undoped LaFeAsO, a structural phase transition [orthorhombic (*Cmme*; a = 5.682 *Å*, b = 5.710 *Å*, c = 8.719 *Å)* ↔ tetragonal (*P4/nmm*; a = 4.032 Å, b = 8.741 Å)] occurs at approximately 160 K, while a magnetic transition (antiferromagnetic ↔ paramagnetic) occurs somewhat below this near 140 K [62-64]. The relationship of these transitions and their potential link to superconductivity are of particular interest owing to the proposal that the structural transition is not driven by the

lattice but by electronic degrees of freedom that spontaneously undergo a mesoscale organization into a nematic phase analogous to those observed in liquid crystals [65-68]. In particular, the electronic nematic phase is characterized by an inhomogeneous ordering of electrons such that translational symmetry is preserved while rotational symmetry is broken [69, 70]. Indeed, electronic nematicity in the iron pnictides is thought to be present over a wide doping and temperature range, bordering the superconducting dome within a particular phase space [71-73], thus suggesting this state may influence superconductivity.

In the layered iron pnictide compounds, the change in unit-cell symmetry due to nematic order results in in-plane (FeAs) anisotropic behavior arising in several observables. For example, such behavior has been observed in the *a* and *b* lattice parameters [74], the magnetic susceptibility and electrical resistivity [65, 67, 75], and the density of states [66, 76]. Accordingly, much attention has been focused on experimentally probing the correlated structural and electronic nature near this phase transition. Indeed, a variety of methods have been employed to study these and other aspects of LaFeAsO, including transport measurements [64, 77, 78], spectroscopic techniques [79, 80], and structural probes (*e.g.*, X-ray and neutron scattering) [62, 64, 81, 82]. In contrast, transmission electron microscopy (TEM) has been employed to a lesser extent, with some studies reporting the observation of the structural phase transition via bright-field imaging and parallel-beam diffraction [77, 83-87]. In this regard, the appearance and disappearance of particular Bragg spots, as well as variation in diffraction contrast, have been pointed to as indicators of a phase change. One might expect,

however, that artifacts arising from thickness-dependent effects (*e.g.*, multiple scattering, electron channeling, *etc*.) [8, 88] and deviations of sample orientation due to temperature-dependent tilting [89] would be convoluted with changes arising from the phase transition, thus rendering direct interpretations challenging. Despite such challenges, the relative dearth of TEM studies on LaFeAsO is noteworthy because the technique enables local probing of electronic properties, chemical composition, and lattice structure, all with atomic-scale spatial resolutions [90, 91]. Further, the effects of time-varying experimental parameters – namely, temperature, strain, and electrical bias – on such properties can be directly followed *in situ* with little to no compromise on spatial resolution [11, 92]. Consequently, high-resolution *in situ* TEM is potentially well-suited for studying nanoscale processes associated with the structural and electronic phase transitions in LaFeAsO and the iron-based superconductors in general.

In this chapter, we report the effects of crystal thickness and dynamical scattering on atomic-resolution TEM images and diffraction patterns for low-temperature (90 K) orthorhombic and room-temperature tetragonal LaFeAsO. Via aberration-corrected high-angle annular dark-field scanning TEM (HAADF-STEM) of LaFeAsO single crystals oriented along the [001] zone axis, we observe modulation of atomic-column *Z*-contrast strength in the tetragonal structure arising from dynamical electron scattering with varying lamella thickness. In relatively thin specimen regions, intensity differences in the (Fe,O) and (La,As) atomic columns is observed, with commensurate Bragg-spot-intensity variations also apparent in parallel-beam electron diffraction patterns (PBEDs). With HAADF-STEM, a crystalline transition region is identified, demarcating relatively thin

and thick specimen sections. At room-temperature, HAADF-STEM images from the thick region show a leveling of intensity, independent of the chemical composition of the atomic column, thus obscuring spatial differentiation of the (Fe,O) and (La,As) columns. This, too, is apparent in PBEDs, resulting in an apparent disappearance of particular Bragg spots, which could be inadvertently interpreted as a manifestation of a structural phase transition with decreasing temperature. To illustrate this effect, we performed cryo-conventional TEM experiments on the relatively thick and thin lamellae, the results of which demonstrate the challenges associated with intensity-only interpretations and highlighting the importance of variations in *d*-spacing (as opposed to Bragg-spot intensity) as an indicator of the structural phase transformation.

3.2 Methods

3.2.1 Specimen Preparation.

Single crystals of undoped LaFeAsO were grown following previously-reported methods [93]. For TEM studies, LaFeAsO single crystals were attached to a copper slot grid (1 mm × 2 mm) using silver epoxy. Electron-transparent lamellae were prepared for TEM studies using an FEI Quanta 200 3D focused-ion-beam system (FIB) operated at 30 kV with a gallium-ion source. For all specimens, a protective coating of polycrystalline platinum (1.5-μm thick) was deposited from a trimethyl(methylcyclopentadienyl) platinum(IV) [$(CH_3)_3Pt(C_pCH_3)$] precursor gas via gallium-ion sputtering in the FIB prior to milling in order to avoid excess ion damage to the crystal surface.

3.2.2 TEM Imaging, Diffraction, and Spectroscopy.

The HAADF-STEM images, X-ray dispersive spectroscopy (XEDS; Super-X EDX spectrometer) elemental mapping and line scans, and electron energy-loss spectra (EELS; Gatan Enfinium ER) were acquired with a probe-corrected FEI Titan G2 60-300 (S)TEM microscope operated at 200 kV. A probe convergence angle of 18 mrad was used, producing an electron-beam probe size of approximately 0.8 Å on the specimen. A detector collection angle of 46.8 to 200 mrad was used for the HAADF-STEM images. A probe convergence angle of 25.3 mrad and a collection angle of 43 mrad were used for low-loss EELS. An FEI double-tilt holder was used for the room-temperature HAADF-STEM, XEDS, and EELS experiments.

The PBED and conventional TEM (CTEM) images were obtained with an FEI Tecnai G2 F30 microscope operated at 300 kV. For *in situ* experiments conducted on tetragonal and on orthorhombic LaFeAsO, a Gatan 626 single-tilt cryo-transfer holder was used. In order to minimize drift, to ensure the crystallographic phase transition was complete, and to ensure the entire specimen had reached thermal equilibrium for the low-temperature studies, the holder and specimen were kept at 90 K for four hours prior to image and diffraction-pattern acquisition. For PBED experiments, selected-area apertures of 1,200 and of 200 nm (diameter, as measured on the image plane) were used. In order to enhance signal-to-noise in the atomic-resolution images, a series of 10 HAADF-STEM *Z*-contrast images were acquired, cross-correlated, and summed. An additional method involving Fourier filtering was also used to enhance signal-to-noise,

wherein spatial-frequency spots in fast-Fourier transforms (FFTs) of the acquired images were masked followed by image reconstruction.

3.2.3 Image and Bragg-Spot Intensity Simulations.

Simulations of atomic-resolution HAADF-STEM images and diffraction-spot intensities were performed using a multislice computational method [88, 94]. For simulated HAADF-STEM images and PBED patterns, the same instrument parameters as those employed in the experiments were used. Atomic thermal vibrations at 300 K were simulated by averaging 10 frozen-phonon configurations for each image [95]. Root-mean-square (RMS) thermal displacement values of 0.052, 0.054, 0.051, and 0.060 Å at 300 K for La, Fe, As, and O were used, respectively [96]. For PBED simulations, thermal effects were not included, as phonons only weakly dampen the diffraction spots at 300 K for atomic vibrations with RMS values of 0.1 Å and smaller [95].

3.3 Results and Discussion

Methods aimed at initially characterizing structure and composition were performed on electron-transparent lamellae prepared from bulk LaFeAsO crystals, the results of which are summarized in Figure 3.1. Via relatively low-magnification bright-field imaging, a region of interest was identified in the tetragonal phase at 300 K and was found to be structurally well ordered and compositionally homogeneous. Using a selected-area aperture, PBEDs were generated from the edge of a lamella along the [001] direction, and it was consistently observed for this particular region that the *100* forbidden reflection (space group *P4/nmm*; No. 129) was present [Fig. 1(b)]. As will be

illustrated in detail below, observation of forbidden reflections is attributed to dynamical- or multiple-scattering events, the particular appearance of which is sensitive to crystal thickness [8]. Within this particular region of interest, atomic-resolution HAADF-STEM images were acquired, the appearance of which further illustrate the structural ordering. Importantly, the (Fe,O) and (La,As) columns are resolved and can be differentiated in the image [Figure 3.1(f)]. Because contrast in high-resolution HAADF-STEM images arises from differences in *Z* of the elements comprising the columns, the intensity modulations for sufficiently thin crystal sections are due to differences in chemical composition, where larger-*Z* elements (*e.g.*, La and As) will give rise to brighter columns in dark-field mode [42]. This, coupled with chemical mapping, enables unambiguous assignment of the structure when compared to the crystallographic information file for tetragonal LaFeAsO [53], provided one is approximately within the kinematic regime.

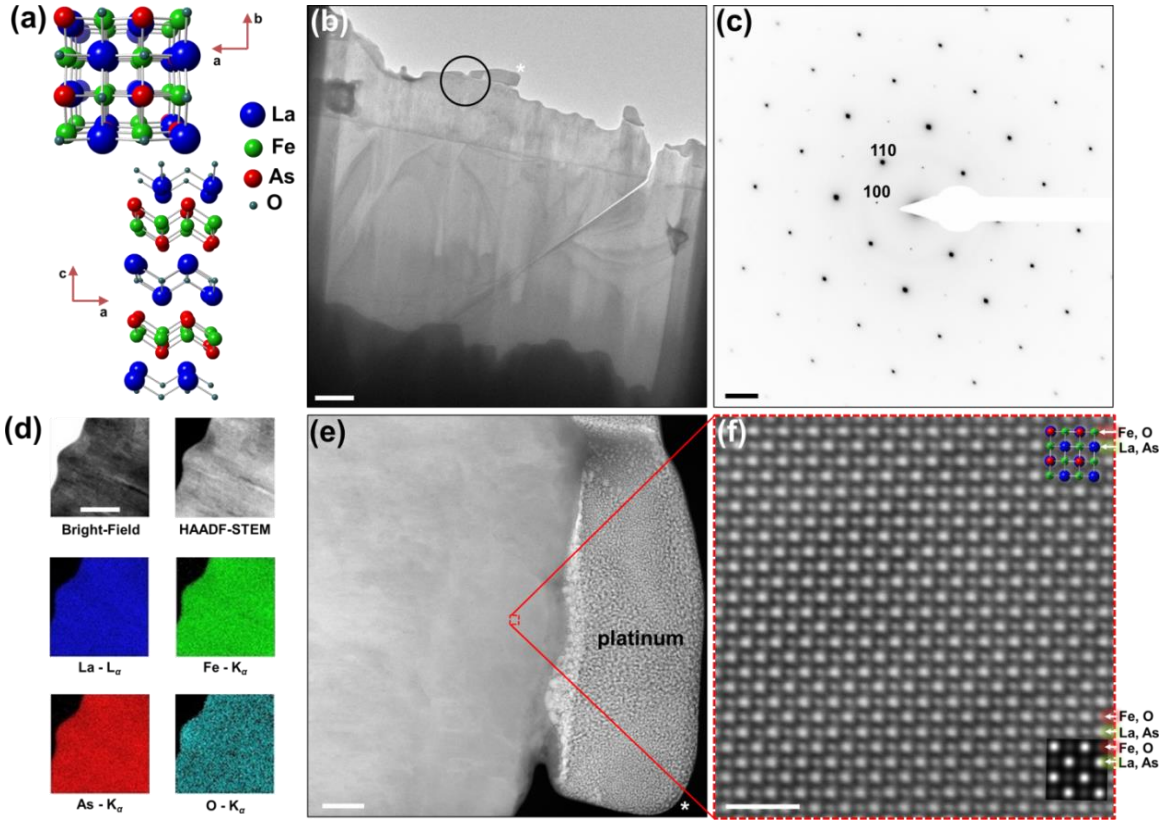

Figure 3.1 Overview of the crystalline order, atomic structure, and chemical composition of the tetragonal LaFeAsO specimen at 300 K. (a) Crystal structure of tetragonal LaFeAsO as viewed along the [001] (top) and [010] (bottom) zone axes, as generated from the crystallographic information file [53]. (b) Bright-field image of an LaFeAsO lamella. The black ring denotes the position of the selected-area aperture used to generate the PBED pattern in panel (c), and the white asterisk to the right of the ring is to orient the reader to the specimen configuration with respect to the higher-magnification image shown in panel (e). The scale bar represents 1 μm. (c) A PBED pattern obtained along the [001] zone axis. The allowed *110* and forbidden *100* diffraction spots are labeled. The contrast has been reversed for added clarity, and the scale bar represents 5 nm^{-1}. (d) Bright-field STEM image, HAADF-STEM image, and

corresponding XEDS elemental maps of La (blue, L_α), Fe (green, K_α), As (red, K_α), and O (teal, K_α). The scale bar in the CTEM image represents 500 nm and is applicable to all frames. (e) A HAADF-STEM image of the region of interest in this study. The red dashed square denotes the region from which the atomic-resolution HAADF-STEM image in panel (f) was generated. The platinum protective capping layer is labeled. The white asterisk in the lower-right corner of the panel is to orient the reader to the specimen configuration with respect to the lower-magnification image in panel (b). The scale bar represents 100 nm. (f) An atomic-resolution HAADF-STEM image obtained along the [001] zone axis, with the (Fe,O) and (La,As) atomic columns labeled. An overlaid schematic crystal structure viewed along the [001] zone axis is shown in the upper-right corner of the panel, with the color coding matching that in panel (a). A simulated HAADF-STEM image, with atomic columns labeled, is shown in the lower-right corner of the panel. The scale bar represents 1 nm; the separation between the (Fe,O) and (La,As) columns is 2.02 Å.

The remainder of the studies focused on the region of interest shown in Figure 3.1(e). Within this region, it was found that two distinct areas [labeled (i) and (ii) in Figure 3.2(a)] could be identified, which appear in the HAADF-STEM images to have distinct morphologies separated by a relatively narrow (~5 nm) transition region running approximately vertically with respect to the frame orientation [Figure 3.2(a,b)]. That is, the identified transition region is distinct, in that the structure does not appear in the images to match either area (i) or (ii). Further, the region does not correspond to a grain

boundary, as no additional Bragg spots were observed in the PBED pattern obtained from the overall region of interest [Figure 3.1(b,c)].

In order to determine whether this apparent structural variation across the transition region arises from thickness and/or compositional effects, which could then affect the observed contrast, both EELS and XEDS were employed. In low-loss EELS, comparison of the intensity of the zero-loss peak and entire low-loss region to 50 eV can be used to determine specimen thickness [97]. The result of such an approach applied to the LaFeAsO specimen region of interest is shown in Figure 3.2(c). It can be seen that the specimen thickness was found to decrease from 80 to less than 60 nm spanning a 550-nm distance and moving toward the crystal edge (*i.e.*, from the interior of the crystal to the platinum capping layer). Such a gradient is known to arise during FIB milling, as beam intensity decreases with increasing specimen depth - in the milling direction - owing to increased scattering. In addition to the observed thickness variation, this process could result in creation of a step, where the atomic columns are not oriented along the [001] zone axis, as in areas (i) and (ii), and would therefore not be discernible in the images. The results of the XEDS chemical map, however, indicate the composition is uniform across the transition region [Figure 3.2(d)]. Thus, it was concluded from this and the structural-overview studies discussed above that any apparent modulation in contrast across the transition region stems from the effects of thickness and morphology on electron scattering rather than on the presence of different phases or compositions.

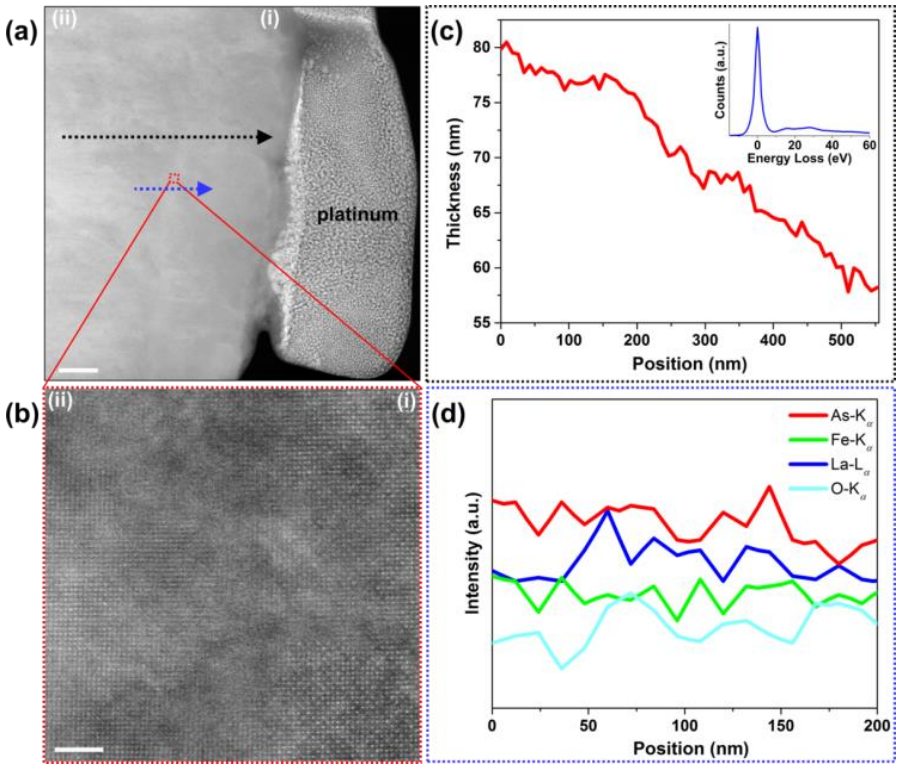

Figure 3.2 Transition region spatial-thickness variation and spatial chemical composition in the LaFeAsO region of interest. (a) Low-magnification HAADF-STEM image. The transition region runs roughly vertically from the top to the bottom of the panel and passes through the dashed red box and the approximate centers of the horizontal dashed arrows. Areas to the right and to the left of this region are labeled (i) and (ii), respectively, at the top of the panel. The polycrystalline platinum capping layer is also labeled. The position and direction from which the thickness and chemical composition were spatially characterized [panels (c) and (d), respectively)] are denoted with a dashed black and dashed blue arrow, respectively. The scale bar represents 100 nm. (b) Higher-magnification HAADF-STEM image of the specimen region outlined with the dashed red box in panel (a). Regions (i) and (ii) are again labeled, as defined above. The scale bar represents 2 nm. (c) Thickness variation of the LaFeAsO crystal in

moving from area (ii) to area (i), as illustrated with the dashed black arrow in panel (a). Note that the position at 0 nm corresponds to the origin of the arrow. The inset shows a representative low-loss EEL spectrum used to determine crystal thickness. (d) An XEDS line scan showing the spatial dependence of composition across the identified transition region, as illustrated with the dashed blue arrow in panel (a). Note that the position at 0 nm corresponds to the origin of the arrow.

To investigate the effects of specimen thickness on image contrast and diffraction-pattern appearance, HAADF-STEM and PBED experiments were performed at 300 K on areas (i) and (ii) (Figure 3.3). As can be seen, differences in both the HAADF-STEM *Z*-contrast images and the intensity of the forbidden *100* reflection in the PBED patterns obtained from each region are apparent. For the HAADF-STEM images, this behavior was consistent throughout the overall region of interest [*i.e.*, both areas (i) and (ii) produced HAADF-STEM images similar in appearance to that displayed in Figure 3.3(a) and (b), respectively], with variations only in total intensity. That is, the behavior of the relative intensities of the atomic columns, while clearly different from area (i) to (ii), were the same within each area. Note, however, that the PBED patterns were observed to have variable *100* Bragg-spot intensities regardless of area. That is, isolation of the two areas with a selected-area aperture proved challenging owing to the relatively large specimen area over which signal was averaged. Accordingly, patterns containing both strong and weak *100* reflections could be obtained across the overall region of interest. Nevertheless, this illustrates the precarious nature of relying solely on

Bragg-spot intensities and appearance/disappearance for following the tetragonal ↔ orthorhombic phase transition.

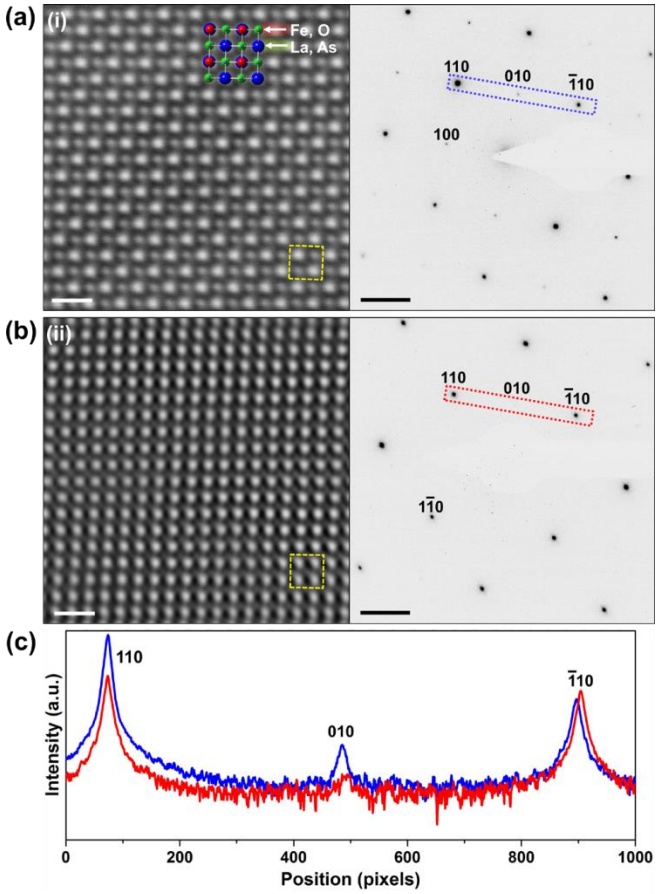

Figure 3.3 Atomic-resolution HAADF-STEM images and PBED patterns from areas (i) and (ii) (defined in Figure 3.2). (a) A HAADF-STEM image (left) and a PBED pattern (right) from area (i) (labeled in upper-left corner of the panel), obtained along the [001] zone axis. An overlaid schematic crystal structure viewed along the [001] zone axis is shown in the upper region of the left panel, with the colors corresponding to those shown in Figure 3.1(a). The (Fe,O) and (La,As) atomic columns are labeled. The dashed yellow square represents the unit cell *ab*-plane (4.03 x 4.03 Å). The scale bar represents 5 Å. In

the corresponding PBED pattern (right), the allowed *110* and $\bar{1}10$ and the forbidden *100* and *010* Bragg spots are indexed. The dashed blue rectangle represents the region of interest from which the intensity profile (blue) in panel (c) was generated. The contrast is reversed for added clarity. The scale bar represents 2 nm^{-1}. (b) A HAADF-STEM image (left) and a PBED pattern (right) from area (ii) (labeled in upper-left corner of the panel), obtained along the [001] zone axis. The dashed yellow square represents the unit cell *ab*-plane. The scale bar represents 5 Å. In the corresponding PBED pattern (right), the allowed *110*, $\bar{1}10$, and $1\bar{1}0$ and the forbidden *010* Bragg spot are indexed. The dashed red rectangle represents the region of interest from which the intensity profile (red) in panel (c) was generated. The contrast is reversed for added clarity. The scale bar represents 2 nm^{-1}. (c) Spatial intensity profiles generated from the dashed rectangles in the PBED patterns in panels (a) and (b). Peaks arising from the *110*, *010*, and $\bar{1}10$ spots are labeled for orientation purposes. Note the significant reduction in intensity of the forbidden *010* spot from area (ii) compared to area (i). The apparent slight shift in *d*-spacing (compare the $\bar{1}10$ peaks) is attributed to a minor variation in the specimen eucentric height from one experiment to the next. This could also arise from slight variations in alignment or the presence of lens hysteresis, with potential contributions from each resulting in an effective change in camera length and corresponding expansion or contraction in the observed PBED pattern.

Inspection of the atomic-column spacings in the HAADF-STEM images, as well as the PBED patterns in Figure 3.3, generally match those expected from the LaFeAsO

tetragonal structure, as viewed along the [001] zone axis. For example, the dashed yellow squares shown in both HAADF-STEM images are the same size, each representing one unit cell (*ab*-plane) of the tetragonal structure. Likewise, the PBED patterns from areas (i) and (ii) match those expected from the tetragonal structure along the [001] direction and the allowed reflections for *P4/nmm* (*hk*0: $h + k = 2n$; *h*00: $h = 2n$). Further, the position of the forbidden *100* reflection also matches that expected for the tetragonal structure with $a = 4.032$ Å and $b = 8.741$ Å. Thus, despite the differences in atomic-column contrast and the presence or absence of the forbidden *100* reflection, it was concluded that the entire region of interest is single-crystal LaFeAsO oriented along the [001] direction. This structural information, in addition to the XEDS chemical mapping, which indicated a homogeneous composition within the region of interest, indicates the contrast variations and appearance of the *100* reflection arise from thickness effects, dynamical scattering, and electron channeling.

To determine the effects of LaFeAsO crystal morphology and thickness on the images and PBED patterns, multislice simulations were performed [88, 94], the results of which are summarized in Figure 3.4. In the simulated HAADF-STEM images of one LaFeAsO unit cell along the [001] direction, it can be seen that the normalized intensity of the (Fe,O) atomic columns increase with crystal thickness (from 20 to 200 nm) relative to the (La,As) columns. This observed monotonic decrease in contrast strength is due to the dependence of electron-beam-channeling behavior on specimen thickness [98-100]. Note that it is not straightforward to compare the thicknesses reported in the simulations to the experimental results, as additional effects arising from the generation of an

amorphous layer during FIB preparation of the lamellae are not taken into account, nor are effects arising from spatial incoherence [100-102]. Such effects can significantly reduce contrast strength in atomic-resolution HAADF-STEM images, especially for relatively thick specimen regions. Further, it is known that contrast strength is also dependent on the particular crystal structure being studied, precise orientation along a zone axis, and the chemical composition of the atomic columns [103]. Accordingly, differences in the atomic-resolution HAADF-STEM images between areas (i) and (ii) are attributed to the combined effects of specimen-thickness variation, the presence of an amorphous layer, and possible mis-orientation with respect to the precise [001] zone axis.

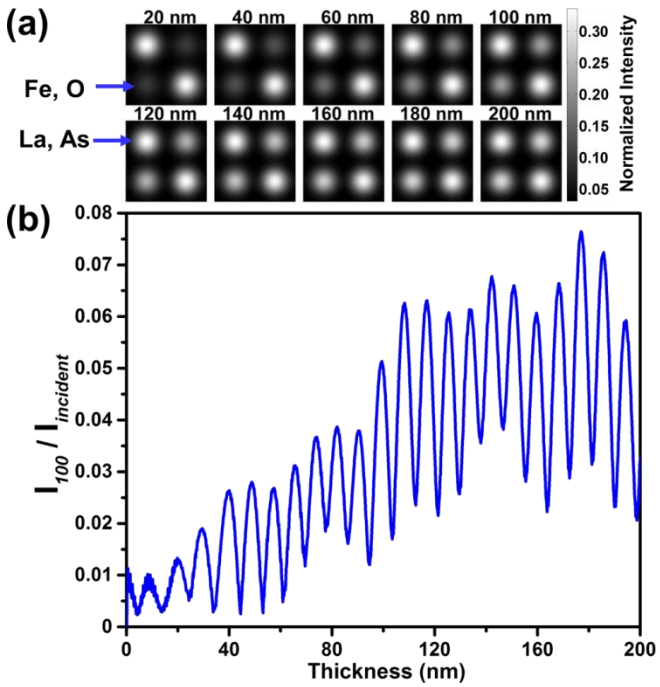

Figure 3.4 Simulated *Z*-contrast images and relative *100* Bragg-spot intensities as a function of LaFeAsO lamella thickness. (a) Simulated HAADF-STEM images representing one unit-cell of the LaFeAsO tetragonal phase along the [001] direction.

The corresponding crystal thicknesses are labeled. Atomic-column intensities are normalized to the incident beam intensity. The positions of the (Fe,O) and the (La,As) columns are labeled. (b) Relative *100* Bragg-spot intensity as a function of lamella thickness. Intensity is normalized to that of the incident beam.

In addition to HAADF-STEM images, the intensity of the *100* forbidden reflection as a function of specimen thickness was simulated [Figure 3.4(b)]. There are two distinct behaviors to note. The first is that the overall normalized intensity increases with specimen thickness, as is expected to occur due to dynamical diffraction [8]. Second, the normalized intensity oscillates with a thickness period of approximately 10 nm; that is, the intensity goes from a local minimum to a local maximum and back to a local minimum over a specimen-thickness range of 10 nm. The particular behavior shown in Figure 3.4(b) is unique to the LaFeAsO tetragonal crystal structure, as such periodic intensity oscillations depend on the chemical composition of the material [104]. Experimentally, the intensity of the *100* reflection was also found to vary across the region of interest owing to variations in specimen thickness. In addition, as with the HAADF-STEM images, mis-orientation of the specimen with respect to the zone axis will affect the intensity of the dynamically-diffracted Bragg spot [8]. Accordingly, matching the simulations to experiments with respect to absolute specimen thickness is challenging.

The results discussed thus far are meant to: (1) illustrate the challenges associated with identifying structural phase changes from atomic-resolution TEM images and

electron-diffraction patterns and (2) to provide information specific to the tetragonal LaFeAsO phase at 300 K for comparison to similar studies conducted on the orthorhombic phase at 90 K. Accordingly, Fourier-filtered atomic-resolution CTEM images and corresponding spatial FFTs of orthorhombic LaFeAsO at 90 K, also oriented along the [001] zone axis, were acquired with a liquid-nitrogen specimen holder (see Methods). As with the tetragonal structure at 300 K, images were acquired within areas (i) and (ii), the results of which are summarized in Figure 3.5. So that direct comparisons can be made, Fourier-filtered CTEM images and corresponding spatial FFTs of tetragonal LaFeAsO at 300 K were also acquired on the same specimen regions. As with the tetragonal structure [Figure 3.5(a,b)], intensities of forbidden reflections were observed to vary for the orthorhombic structure (*e.g.*, the *110* spot; space group *Cmme*, No. 67; *hk*0: $h, k = 2n$) and were dependent upon position within the overall region of interest [Fig. 5(c,d)]. That is, the appearance and disappearance of forbidden reflections occurs independent of the structural phase transition. It is important to emphasize here that the images in Figure 3.5(a) and Figure 3.5(c) (tetragonal and orthorhombic LaFeAsO, respectively) were acquired from the same area in the specimen, as was the case for the images in panels (b) and (d).

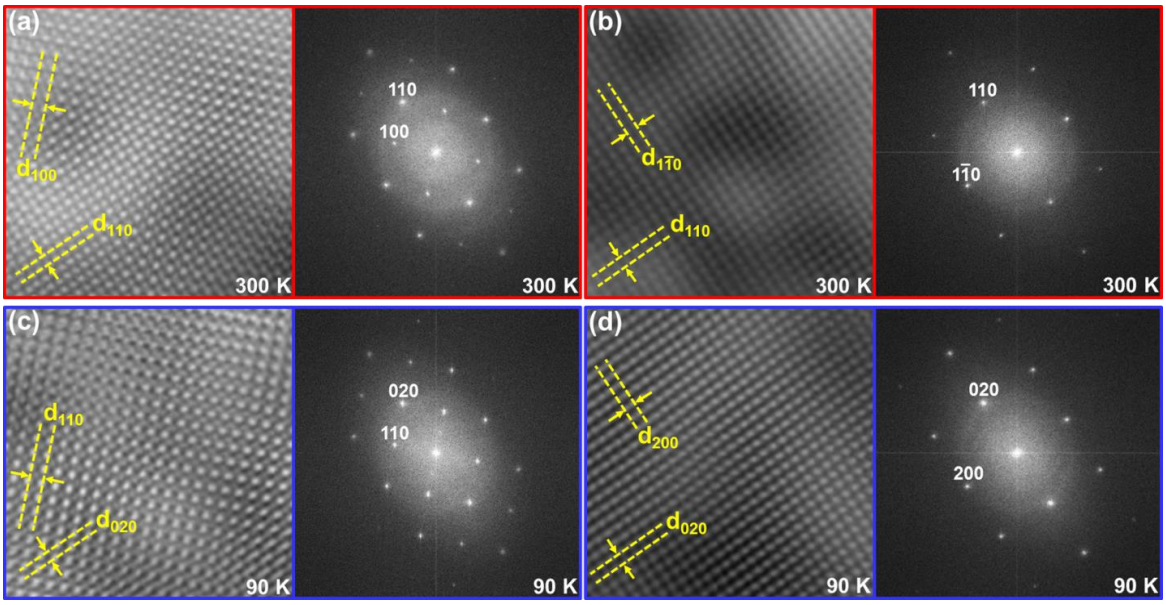

Figure 3.5 *In situ* CTEM images and corresponding FFTs of tetragonal and orthorhombic LaFeAsO illustrating the independence of forbidden-reflection intensity and pattern appearance on structural phase transition. (a) Fourier-filtered CTEM image and corresponding FFT of tetragonal LaFeAsO at 300 K. The *d*-spacings of particular (*100*) and (*110*) planes are labeled. The allowed *110* and forbidden *100* reflections are indexed in the corresponding FFT. (b) Fourier-filtered CTEM image and corresponding FFT of tetragonal LaFeAsO at 300 K but from a different crystal region than that shown in panel (a). The *d*-spacings of particular ($1\bar{1}0$) and (*110*) planes are labeled, and these allowed reflections are also indexed in the corresponding FFT. Note the absence of a forbidden *100* reflection. (c) Fourier-filtered *in situ* CTEM image and corresponding FFT of orthorhombic LaFeAsO at 90 K acquired from approximately the same region as shown in panel (a). The *d*-spacings of particular (*110*) and (*020*) planes are labeled. The allowed *020* and forbidden *110* reflections are indexed in the corresponding FFT. (d) Fourier-filtered CTEM image and corresponding FFT of orthorhombic LaFeAsO at 90 K

from approximately the same region as shown in panel (b) but from a different region than that shown in panel (c). The *d*-spacings of particular (*200*) and (*020*) planes are labeled, and these allowed reflections are also indexed in the corresponding FFT. Note the absence of a forbidden *110* reflection.

The results summarized in Figure 3.5 indicate that the appearance or disappearance of forbidden reflections, or an overall change in the FFT itself, can occur independent of the LaFeAsO structural phase transition. Rather, variations in the images and FFTs can be entirely dependent upon the region from which the data is acquired. This behavior is especially noteworthy when one considers the non-trivial shifting of specimen position and tilt orientation that can occur during *in situ* heating and cooling experiments [89]. This becomes particularly challenging when noting the extreme sensitivity of diffraction contrast and Bragg-spot intensity on changes in either reciprocal-lattice orientation or Ewald-sphere position [8].

The similar overall appearance of the CTEM images, corresponding FFTs and PBED patterns [Figure 3.6] of the two structural phases of LaFeAsO is to be expected considering the minor differences in lattice *d*-spacings, as viewed along the [001] zone axis. Note for example, that in the tetragonal phase, *d*-spacings giving rise to the forbidden *100* and allowed *110* and $1\bar{1}0$ reflections are similar to the forbidden *110* and allowed *020* and *200* reflections from the orthorhombic phase (tetragonal: d_{100} = 4.033 *Å*, $d_{110} = d_{1\bar{1}0}$ = 2.852 *Å*; orthorhombic: d_{110} = 4.028 *Å*, d_{020} = 2.855 *Å*, d_{200} = 2.841 *Å*) [63, 64]. This – in addition to the challenges associated with the presence of forbidden

reflections detailed above – suggests that differentiation of the two phases (and observation of the phase change *in situ*) requires a stable system and a large camera length, such that few-pixel (or even sub-pixel) shifts in Bragg-spot positions can be observed and differentiated from artifacts arising from variations in specimen eucentric height and lens hysteresis. Differentiation and deconvolution of such effects with respect to observing the structural phase change *in situ* will be the focus of a future study.

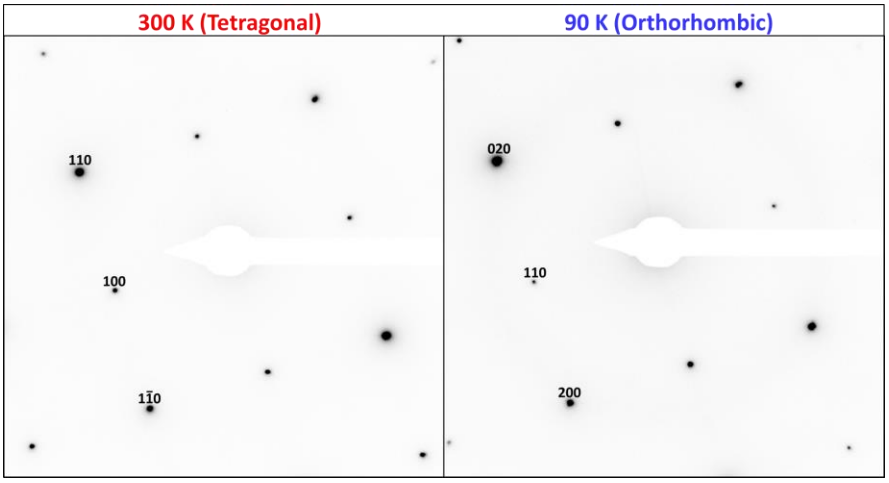

Figure 3.6 *In situ* PBED patterns of tetragonal and orthorhombic LaFeAsO illustrating the independence of forbidden-reflection intensity on structural phase transition. (Left) PBED pattern of tetragonal LaFeAsO at 300 K. The allowed *110*, $1\bar{1}0$ and forbidden *100* reflections are indexed. (Right) PBED pattern of orthorhombic LaFeAsO at 90 K. The allowed *200*, *020* and forbidden *110* reflections are indexed.

3.4 Conclusion

The effects of specimen-thickness on atomic-resolution HAADF-STEM and Fourier-filtered CTEM images and PBED patterns of [001]-oriented LaFeAsO single crystals at 300 and 90 K (*i.e.*, the tetragonal and orthorhombic phases, respectively) have been studied. It was shown that nanoscale thickness variations in LaFeAsO lamellae can produce significant variations in contrast strength of (La,As) and (Fe,O) atomic columns in the HAADF-STEM images, as supported by multislice simulations. In addition to thickness effects, it was speculated that the presence of an amorphous layer arising from FIB preparation of the lamellae, as well as specimen mis-orientation with respect to the [001] zone axis, could also be contributing factors to the observed atomic-column intensity modulations. Additionally, the appearance and disappearance of forbidden reflections in the PBED patterns was attributed to dynamical diffraction (as supported by simulations) and was found to be independent of the phase transition. Importantly, it was found by direct comparison of the tetragonal and orthorhombic phases via atomic-resolution Fourier-filtered CTEM across different specimen regions that the phase change did not produce a change in the observed spatial FFT; the appearance of the image contrast and corresponding FFTs was independent of the structural phase change. These results indicate that processes associated with dynamical diffraction and electron channeling in high-resolution and *in situ* TEM studies must be quantified and deconvoluted from images and diffraction patterns in order to identify effects arising from structural phase changes in LaFeAsO and other materials.

3.5 Future Directions

Foremost work should aim to differentiate and deconvolute specimen eucentric height and lens hysteresis effects from the *in situ* structural phase change along [001] orientation. It was also noticed in the preliminary testing that the *in situ* structural phase change could be observed more easily along [100] crystal orientation of LaFeAsO than the [001]. Figure 3.7 summarizes these preliminary results. A significant shift of approximately 30-40 pixels could be seen at sufficiently large camera lengths along [100] orientation because the lattice spacing of diffraction spots from tetragonal and orthorhombic phases are apparently very different. Therefore in the future, [100] oriented specimens could prove more useful than the [001] oriented specimens in understanding the *in situ* structural phase transition of LaFeAsO after carefully understanding the specimen eucentric height and lens hysteresis effects.

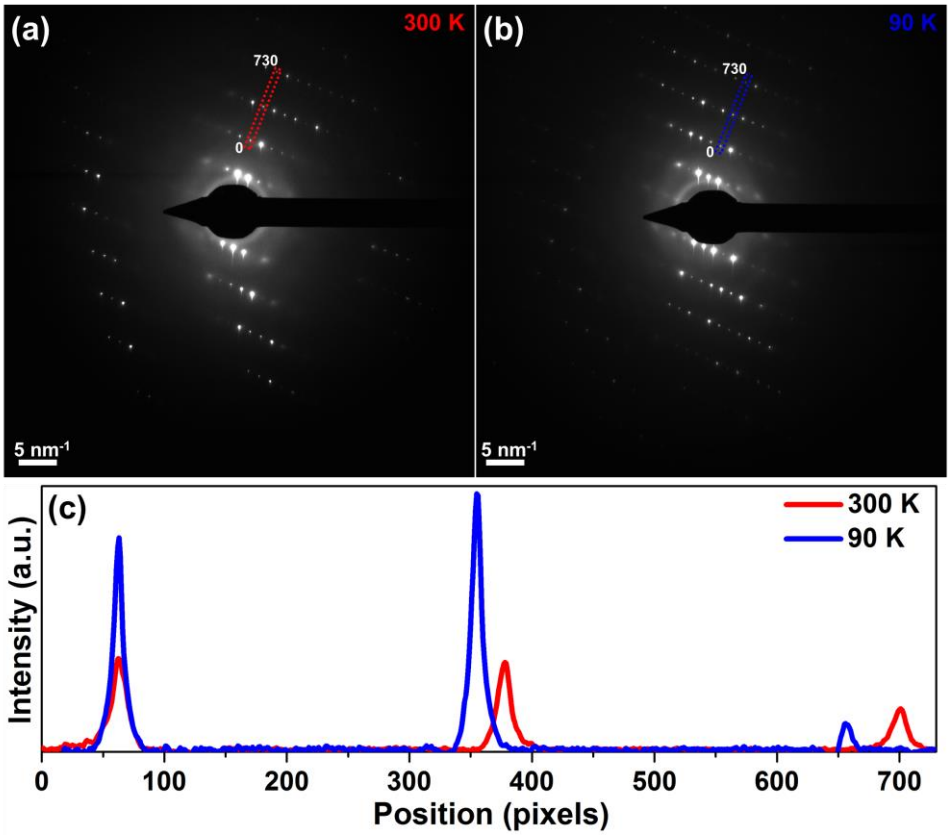

Figure 3.7 (a) A PBED pattern obtained close to the [100] zone axis of tetragonal LaFeAsO at 300 K. The dashed red rectangle represents the region of interest from which the intensity profile (red) in panel (c) was generated. (b) A PBED pattern obtained close to the [100] zone axis of orthorhombic LaFeAsO at 90 K. The dashed blue rectangle represents the region of interest from which the intensity profile (blue) in panel (c) was generated. (c) Spatial intensity profiles generated from the dashed rectangles in the PBED patterns in panels (a) and (b). Note the significant shift in peak position due to the structural phase transition.

At 300 kV, significant specimen damage was found in the STEM imaging and, therefore, all the experiments to study dynamical effects were conducted at 200 kV.

Figure 3.8 summarizes the electron beam damage results. Another avenue to explore would be to systematically carry out an electron beam damage study on layered LaFeAsO at 300 kV, as performed on other layered materials like zeolites [105]. This would expand the atomic-resolution imaging space of LaFeAsO.

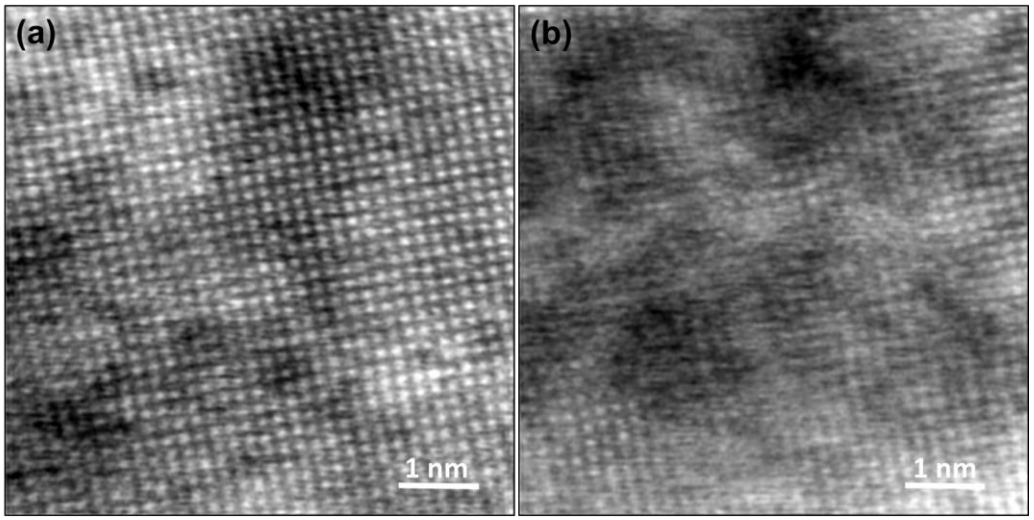

Figure 3.8 (a) A raw HAADF-STEM image, after a 10 s acquisition at 300 kV, from relatively thicker region of LaFeAsO and not showing *Z*-contrast in atomic columns. Note that the STEM probe was not rastered onto this region before acquisition. (b) Raw HAADF-STEM image acquired right after the acquisition in panel (a) with a 10 s integration time. Note that the disappearance of atomic-columns is a consequence of electron beam damage, not a deposition of carbon contamination on TEM specimen with electron beam because this disappearance of atomic-columns was not observed at 200 kV.

To experimentally understand the proposed electronic origins of nematic

fluctuations in literature, an *in situ* EELS study would be useful because EELS has the capability to study the electronic properties and density of states of a wide variety of materials at the atomic-scale [97, 106, 107]. By performing cryo-EELS and analyzing the near-edge fine structure of Fe, O, La edges various interesting electronic properties of LaFeAsO could be discovered *in situ*. In the present study, EEL spectra from LaFeAsO were acquired at room temperature on multiple occasions, and a representative spectrum in Figure 3.9 clearly shows the O *K*, Fe L_3, La M_4 and La M_5 EEL edges of tetragonal LaFeAsO.

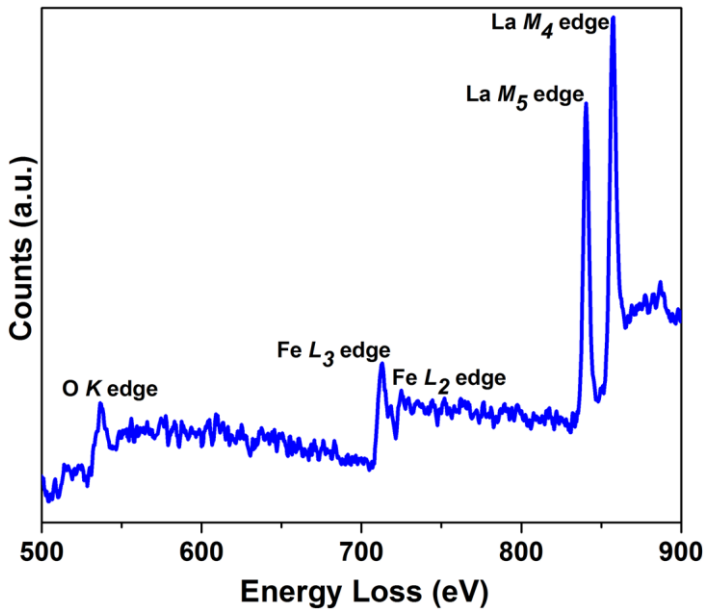

Figure 3.9 Core-loss EEL spectrum of tetragonal LaFeAsO.

It was also seen in the present study while examining the *Z*-contrast strength in the atomic-columns of HAADF-STEM images that the roles of amorphous layer around FIB-milled TEM specimens and of crystal mis-orientation varies from material to material and

are not clearly known for tetragonal LaFeAsO. Therefore, to quantitatively understand the role of amorphous layer and crystal mis-orientation on the *Z*-contrast strength of LaFeAsO atomic-columns, an in-depth multislice simulation study on HAADF-STEM images could be carried out as done in literature for other materials [102, 103].

Chapter 4

Ultrafast Structural Dynamics of the Iron-Pnictide Parent Compound LaFeAsO

4.1 Introduction

Unconventional superconductors are known to exhibit superconductivity by undergoing a spin density wave (SDW) transition at low temperatures. The SDW state is a low-energy ordered state of solids that occurs at low-temperature in anisotropic, low-dimensional materials and in metals having a high density of states at the Fermi level. The orthorhombic phase of LaFeAsO is one such SDW phase. It is not known whether the tetragonal-to-orthorhombic transition is a regular structural transition driven by lattice vibrations (phonons) or driven by electronic origins [70, 108]. Moreover, if electrons are driving this transition, charge/orbital fluctuations or spin fluctuations may be responsible [70, 108]. Figure 4.1 shows the theoretical nematic order and fluctuations present above the structural phase transition temperature, but these nematic phases have never been observed in real-space. The holy grail of performing the ultrafast studies on LaFeAsO is to observe these nematic phases using UEM by heating the liquid-nitrogen cooled specimens with laser above their structural phase transition temperature and to determine the timescales involved with these reversible transitions. This chapter lays the foundation

for imaging the nematic phases by studying the structural dynamics of tetragonal undoped LaFeAsO in UEM.

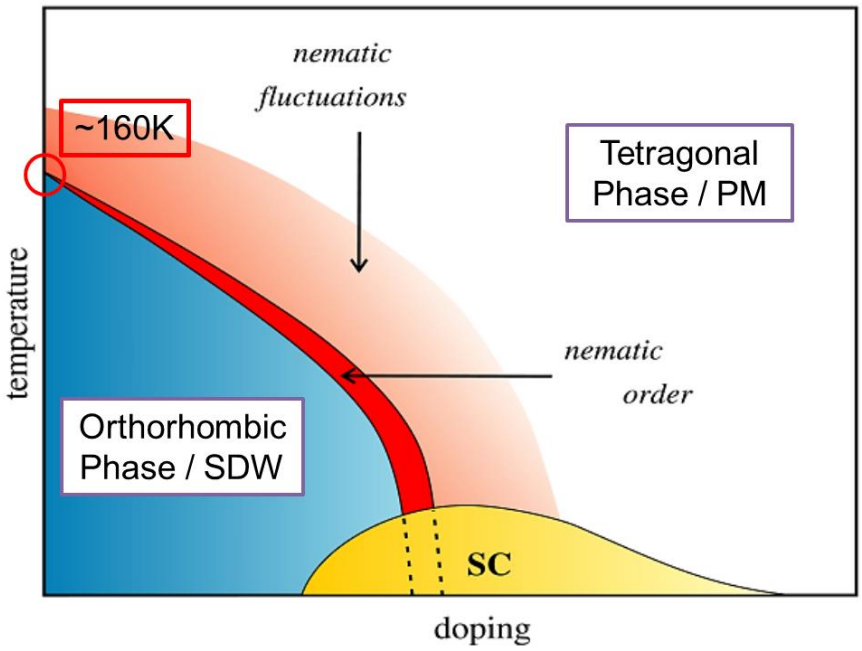

Figure 4.1 Schematic phase diagram of the iron pnictides. SDW denotes the spin-density wave state, SC the superconducting phase, PM the paramagnetic phase. Structural phase transition (orthorhombic ↔ tetragonal) occurs around 160 K in undoped LaFeAsO. Adapted from ref [108].

4.2 Methods

4.2.1 Specimen Preparation.

Single crystals of undoped LaFeAsO were grown following previously-reported methods [93]. For UEM studies along [001] orientation, LaFeAsO single crystals were attached to a copper slot grid (1 mm × 2 mm) using silver epoxy. Electron-transparent

lamellae were prepared for UEM studies using an FEI Quanta 200 3D focused-ion-beam system (FIB) operated at 30 kV with a gallium-ion source. For UEM studies along [100] orientation, LaFeAsO lamella were cut from the single crystals with gallium-ion beam and lifted-out with Omniprobe® micromanipulator inside FIB, and attached to a Omniprobe® lift-out TEM copper grid with three posts and then finally milled with gallium-ion source to get an electron transparent LaFeAsO lamella. For all specimens, a protective coating of polycrystalline platinum (1.5-μm thick) was deposited from a trimethyl(methylcyclopentadienyl) platinum(IV) [$(CH_3)_3Pt(C_pCH_3)$] precursor gas via gallium-ion sputtering in the FIB prior to milling in order to avoid excess ion damage to the crystal surface.

4.2.2 Microscope Parameters.

All the UEM experiments, thermionic imaging and diffraction were performed in a Tecnai Femto ultrafast electron microscope (FEI Company) operated at 200 kV in both thermionic and photoelectron modes. In these emission modes, a truncated, 150 μm flat LaB_6 cathode (Applied Physics Technologies) was used. A Gatan Orius 2048 × 2048 CCD camera was used to record the images with integration times ranging from 1 to 15 seconds per frame. A custom 1,250 μm condenser aperture was employed for all the femtosecond experiments in order to maximize the capture of photoelectrons on the CCD camera. Low-Loss EELS experiments for specimen thickness measurement were performed in an FEI Tecnai G2 F30 microscope operated at 300 kV and equipped with a Gatan Enfina spectrometer. Scanning Electron Microscopy (SEM) imaging was

performed in the secondary electron mode at 5 kV in a FEG-SEM JEOL 6500 microscope at around 10 mm working distance.

4.2.3 Laser Parameters.

LaFeAsO TEM specimens were optically excited *in situ* with a pump pulse of 250 fs duration full-width at half-maximum (FWHM), centered at 515 nm for nanosecond experiments and centered at 1030 nm for femtosecond experiments. A Yb:KGW (1030 nm fundamental output), diode-pumped solid-state laser and a custom harmonics generation module were used to generate the pump pulses for both nanosecond and femtosecond experiments. Pump fluences of 31.6 mJ/cm^2 were incident on the specimen for nanosecond bright-field imaging and PBED experiments. For femtosecond UEM studies along [001] orientation, pump fluences of 5.1 mJ/cm^2 were incident on the specimen for bright-field imaging and PBED experiments with 5 ps (-160 to 240 ps) and 20 ps (-360 to 2040 ps) time-steps, and pump fluences of 4.6 mJ/cm^2 were incident on the specimen for PBED experiments with 0.5 ps (-20 to 100 ps) time-steps. For femtosecond UEM studies along [100] orientation, pump fluences of 1.5 mJ/cm^2 were incident on the specimen for bright-field imaging experiments.

Probe pulses were generated with a Nd:YAG (1064 nm fundamental output), Q-switched, diode-pumped solid-state laser for nanosecond experiments. The fourth harmonic was generated on the laser table and was used to generate the photoelectrons out of the LaB_6 cathode for image formation. To generate the probing photoelectron packets in femtosecond experiments, the pump line was split, and a portion of the 515 nm pulses was frequency doubled to 257.5 nm and focused into the gun region of the

microscope. Nanosecond and femtosecond UEM experiments were performed at a repetition rate of 5 kHz and 50 kHz respectively to ensure maximum mechanical and thermal relaxation before each subsequent excitation. Nanosecond UEM bright-field imaging experiments were performed with 1 ns time-steps, and PBED experiments were performed with 1 ns (-56 to 184 ns) and 10 ns (-116 to 9984 ns) time-steps. For [001] orientation, femtosecond UEM bright-filed imaging experiments were performed with 1 ps time-steps, and PBED experiments were performed with 5 ps (-160 to 240 ps), 20 ps (-360 to 2040 ps) and 0.5 ps (-20 to 100 ps) time-steps. For [100] orientation, femtosecond UEM bright-filed imaging experiments were performed with 2 ps time-steps.

4.2.4 Control Experiments.

A series of control experiments were performed immediately after the scans in which femtosecond bright-field and PBED dynamics was observed along [001] orientation. These experiments were performed at the same experimental parameters to exclude artifacts and instabilities of the UEM experimental system as the reason of the observed propagating contrast waves in bright-field imaging and PBED dynamics in the femtosecond experiments along [001] orientation. (1) Control experiments to replicate the dynamics were performed by acquiring bright-field images and diffraction patterns with randomized time-points. This resulted in similar dynamics as non-randomized acquisitions. (2) Control experiments, for the origin of bright-field dynamics at the vacuum-specimen interface and the downward propagation direction of waves, were conducted by rotating the specimen 180º on TEM holder and then carrying out the

experiments. This resulted in similar dynamics as without rotating the specimen. (3) Control experiments for probe beam instabilities in both bright-filed imaging and PBED due to movement of delay stage were performed by acquiring 61 images four times without specimen excitation but still translating the delay stage as if a UEM scan (-100 to 200 ps with 5 ps steps) was being performed. This resulted in no dynamics of any kind. (4) Control experiments for specimen drift/tilt in both bright-filed imaging and PBED were conducted by acquiring 111 images each at four constant time delays of -150, -75, -50 and 50 ps to emulate the duration of a scan. This resulted in no dynamics of any sort. (5) Control experiments for image intensity fluctuations due to LaB_6 filament instabilities in both bright-filed imaging and PBED were performed by acquiring 101 images (-50 to 50 ps with 1 ps steps) without specimen excitation but delay stage moving. This again resulted in no dynamics of any sort.

4.2.5 Data and Image Processing.

In order to accurately depict and analyze the real-space UEM dynamics, all the raw bright-field images were drift-corrected with sub-pixel resolution and then passed through a 2-pixel Gaussian 3D low-pass filter. Frequency maps in Figure 4.2 for bright-field images were obtained by first drift-correcting all the images and then performing a fast Fourier transform (FFT) on the image intensity versus time plot for each pixel. The image intensities were normalized with respect to a vacuum region in the images to exclude instabilities in the probe beam intensities with time.

Finite element method (FEM) simulations in Figure 4.3 were performed with Structural Mechanics module of COMSOL Multiphysics®. An LaFeAsO plate (clamped

on three sides and free on one end) of dimensions 8.5 μm × 4.5 μm × 70 nm with Young's modulus of 141.5 GPa, Poisson's ratio of 0.259 and mass density of 6.7 g/cm^3 was taken into account for simulations. The length and width of the plate were measured from the bight-field images, and a constant thickness of 70 nm was assumed. Young's Modulus and Poisson's ratio values were taken of polycrystalline LaFeAsO from the work of Shein and Ivanovskii [109], and mass density was calculated from the unit-cell of LaFeAsO.

A Gaussian fitting was done to all the diffraction spots in PBED patterns and the distances between the various diffraction spots were tracked with time to observe their dynamics. Normalized reciprocal *d*-spacing changes in Figures 4.5-4.7 and 4.21-4.23 were obtained by taking an average of data-points over negative time (called d_{avg}^{-1}) and then calculating the reciprocal *d*-spacing changes with respect to that average value based on the following equation:

$$\frac{\Delta d^{-1}}{d^{-1}}(\%) = \frac{d(t)^{-1} - {d_{avg}}^{-1}}{{d_{avg}}^{-1}} \times 100$$

All the *d*-spacing changes were calculated on the reciprocal space (or diffraction space). The error bars are the standard deviation values from the multiple scans/experiments performed. Same procedure was adopted for calculating the normalized diffraction spot intensity changes in Figures 4.18-4.20 based on the following equation:

$$\frac{\Delta I}{I}(\%) = \frac{I(t) - I_{avg}}{I_{avg}} \times 100$$

Megahertz frequencies in panel (c) of Figures 4.5-4.7 were obtained by fitting a third order polynomial to the data-points in panel (b) over positive time and then performing the FFT on the residual data-points. Space-time plots in Figures 4.9, 4.11 and 4.15 were calculated by drawing a line in the direction of propagating contrast waves and integrating image intensity over 50 pixels across that line at every pixel of its length. The integrated image intensity in that 1 pixel × 50 pixel box is tracked with time. This was done for the whole dashed blue and red box regions in Figures 4.8 and 4.14.

4.3 Results and Discussion

4.3.1 Nanosecond Bright-Field Imaging.

UEM imaging and diffraction were performed on electron-transparent lamella prepared from bulk LaFeAsO crystals. The results are shown in Figure 4.2 and this area was selected as the region of interest for all the nanosecond bright-field imaging and PBED experiments. Diffraction contrast and an absence of *100* forbidden reflections can be clearly seen in the UEM bright-field image and PBED pattern, respectively.

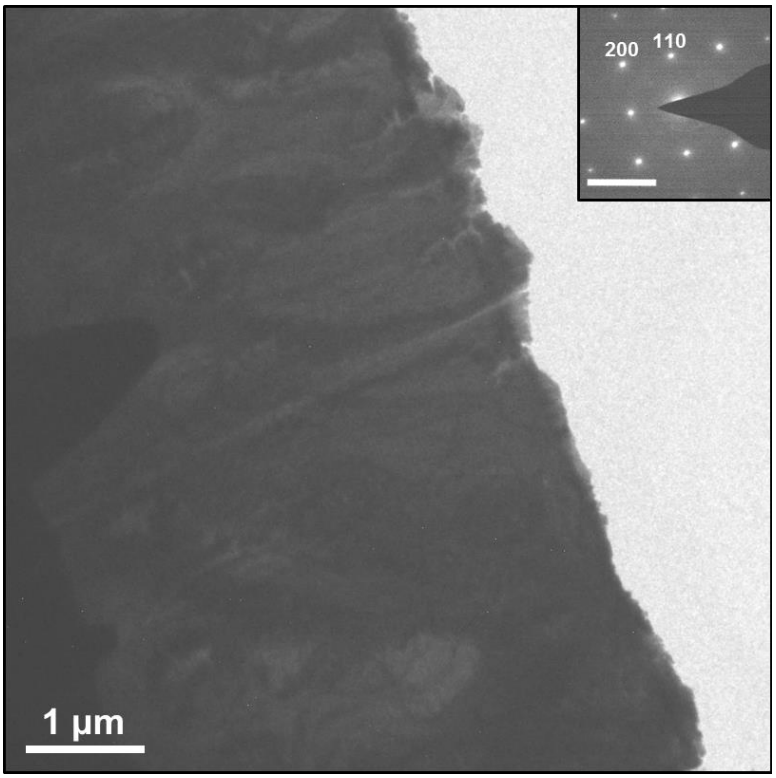

Figure 4.2 A representative UEM bright-field image and a UEM PBED pattern along [001] orientation (inset) of a LaFeAsO TEM lamella for nanosecond experiments. The inset scale bar is 5 nm^{-1}.

Nanosecond bright-field imaging dynamics (over -57 to 483 ns) were observed in the region of interest. It was seen that for negative time-points there was not any change in the diffraction contrast features, but for positive time-points severe changes in the diffraction contrast were seen. Frequency mapping (see Methods section for details) was performed to extract the frequencies associated with the movement of the diffraction contrast features. The results are summarized in Figure 4.3. Frequencies on the order of tens of megahertz were observed in the dynamics.

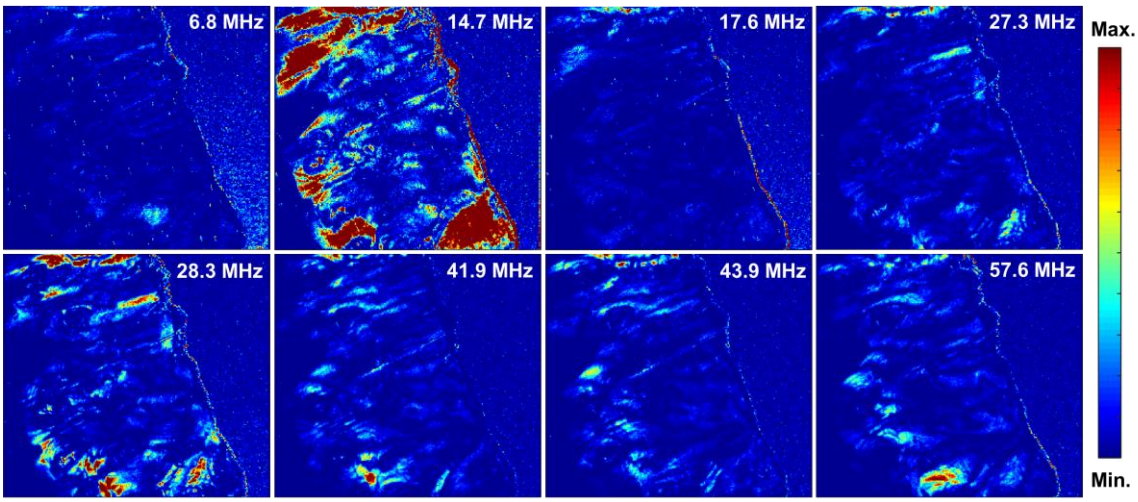

Figure 4.3 Frequency maps from a UEM bright-field imaging data-set showing the nanosecond dynamics. Each image depicts the spatial distribution of a frequency, written on its top right.

In conjunction with experiments, FEM simulations were conducted to understand the origin of the diffraction contrast motion and to see if there is a direct correlation between the experimentally observed frequencies of diffraction contrast motion and the Eigen frequencies of a vibrating plate. Figure 4.4 summarizes the Eigen modes and frequencies associated with a vibrating LaFeAsO plate. Interestingly, a close match between the experimental and simulation frequencies was found. This suggests that the origin of the diffraction contrast motion and the nanosecond dynamics is the oscillatory nature of the LaFeAsO TEM lamella upon laser illumination which continuously changes the angle between the specimen and the probing electron pulse. This causes a continuous change in the Bragg condition of the lamella resulting in a change in local bright-field

intensity and hence leading to a relocation of the diffraction contrast feature with time, as illustrated by the Howie-Whelan equation.[41] It is important to note here that the spatial and temporal resolutions offered through UEM resulted in the determination of these megahertz photoinduced mechanical vibrations in real-space which is currently not possible with other ultrafast techniques.

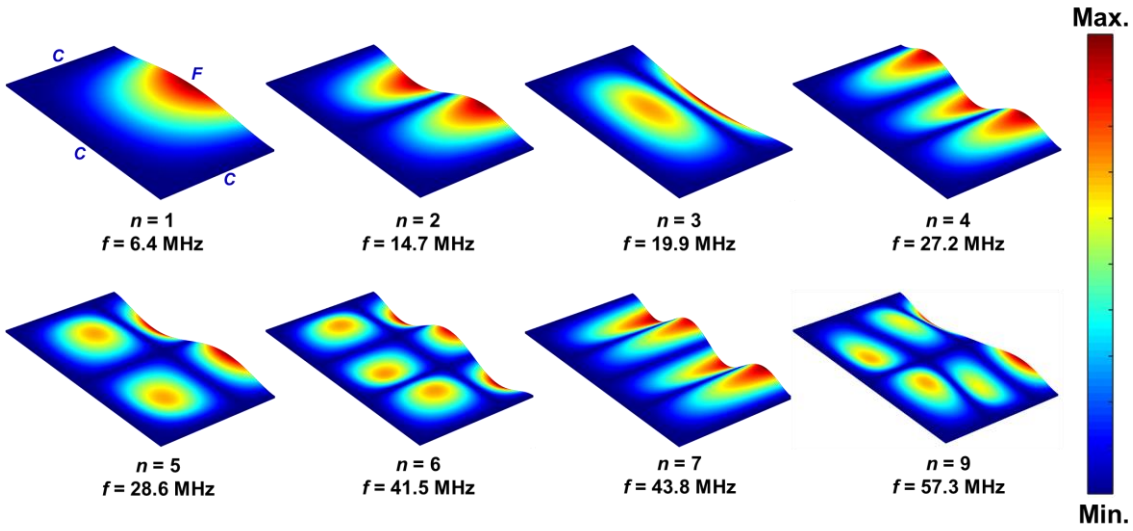

Figure 4.4 FEM simulation results showing the transverse Eigen frequencies and Eigen modes of a thin vibrating plate of LaFeAsO which is clamped on three sides and free on one end. F denotes a free boundary, C denotes a clamped (also known as a fixed) boundary, and *n*, *f* stand for Eigen mode and Eigen frequency respectively.

4.3.2 Nanosecond Electron Diffraction.

The response of the LaFeAsO TEM lamella, used to understand the nanosecond bright-field dynamics, was also studied in reciprocal-space on nanosecond time-scales.

Figures 4.5-4.7 summarize the results. It can be clearly seen from the panels (a) and (b) of Figures 4.5-4.7 that that there is a reduction in reciprocal lattice vector, which suggests an expansion in the LaFeAsO lattice upon laser illumination. This decrease is followed by an oscillatory behavior and can be clearly seen up to 10,000 ns in panels (b). The relaxation of the curve to nearly 0 in panels (b) of Figures 4.5 and 4.6 signifies a thermal recovery of the lattice heating in 10,000 ns.

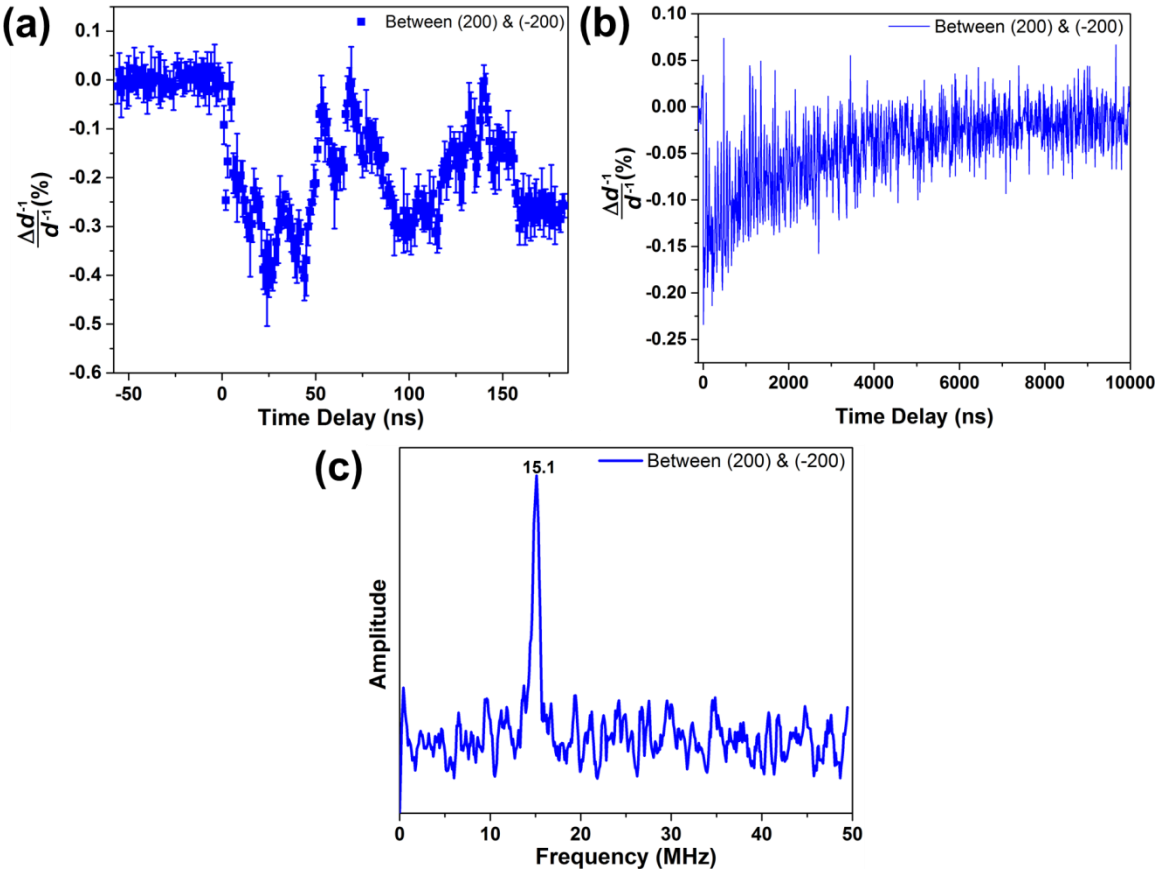

Figure 4.5 (a, b) Nanosecond PBED dynamics showing the changes in distance between *200* and $\bar{2}00$ diffraction spots on the reciprocal space (or diffraction space). The error bars in panel (a) are standard deviation values from 5 scans/experiments. The plot in

panel (b) shows the average values from two scans/experiments. (c) FFT of the dynamics shown in panel (b).

A FFT from Figure 4.5(b) yields megahertz frequencies which is in close proximity to the Eigen frequency for n = 2 of a LaFeAsO vibrating plate. No clear frequency was observed in the FFT of Figure 4.6(b) which might be due to a noisy data. A FFT from Figure 4.7(b) yields megahertz frequencies which are in close proximity to the Eigen frequencies for n = 2, 5, 7 of a LaFeAsO vibrating plate. This points to the presence of mechanical vibrations which were also seen in the bright-field dynamics and hence not surprising. Therefore, it can be concluded from the PBED dynamics that there is a convolution of thermal recovery with the mechanical vibrations in the LaFeAsO TEM lamella. The results from PBED dynamics point-out that there are *d*-spacing changes at megahertz frequencies associated with mechanical vibrations.

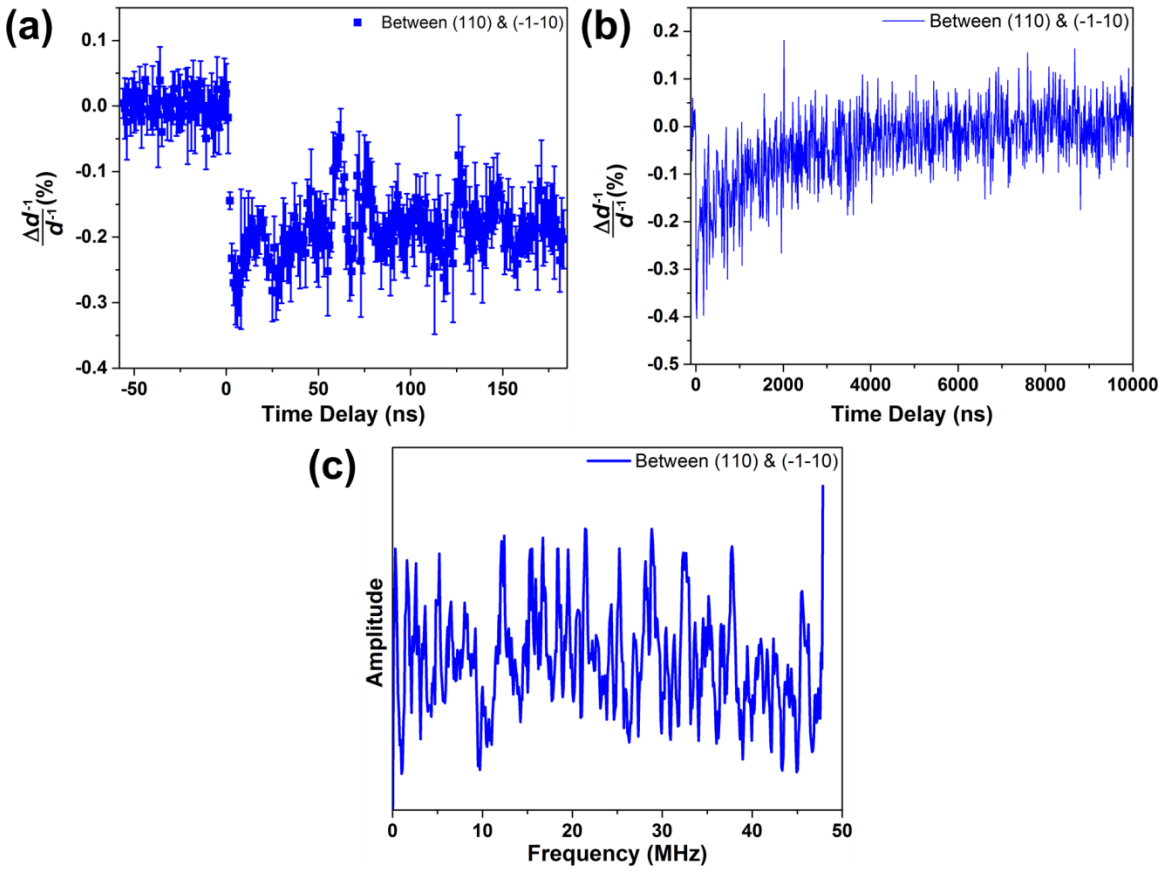

Figure 4.6 (a, b) Nanosecond PBED dynamics showing the changes in distance between *110* and $\bar{1}\bar{1}0$ diffraction spots on the reciprocal space (or diffraction space). The error bars in panel (a) are standard deviation values from 5 scans/experiments. The plot in panel (b) shows the average values from two scans/experiments. (c) FFT of the dynamics shown in panel (b).

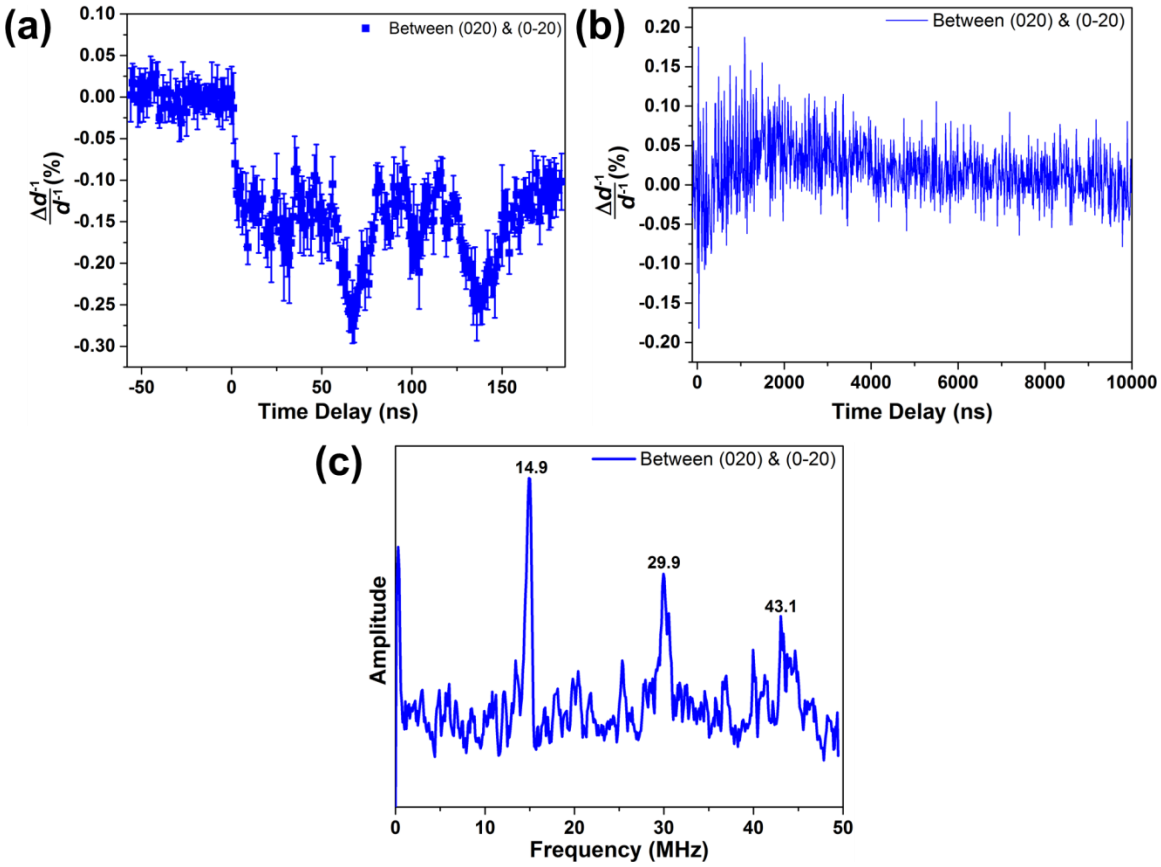

Figure 4.7 (a, b) Nanosecond PBED dynamics showing the changes in distance between *020* and *0$\bar{2}$0* diffraction spots on the reciprocal space (or diffraction space). The error bars in panel (a) are standard deviation values from 5 scans/experiments. The plot in panel (b) shows the average values from two scans/experiments. (c) FFT of the dynamics shown in panel (b).

4.3.3 Femtosecond Bright-field Imaging.

Femtosecond experiments were performed on a different LaFeAsO TEM lamella than the one used for nanosecond experiments. Figure 4.8 shows the lamella used in the femtosecond experiments. It would be ideal to use a relatively thinner TEM lamella for

femtosecond experiments than nanosecond, owing to a lowered number of photoelectrons in a femtosecond probing packet. In the present study, the exact thickness of TEM lamella used in the nanosecond experiments was not measured.

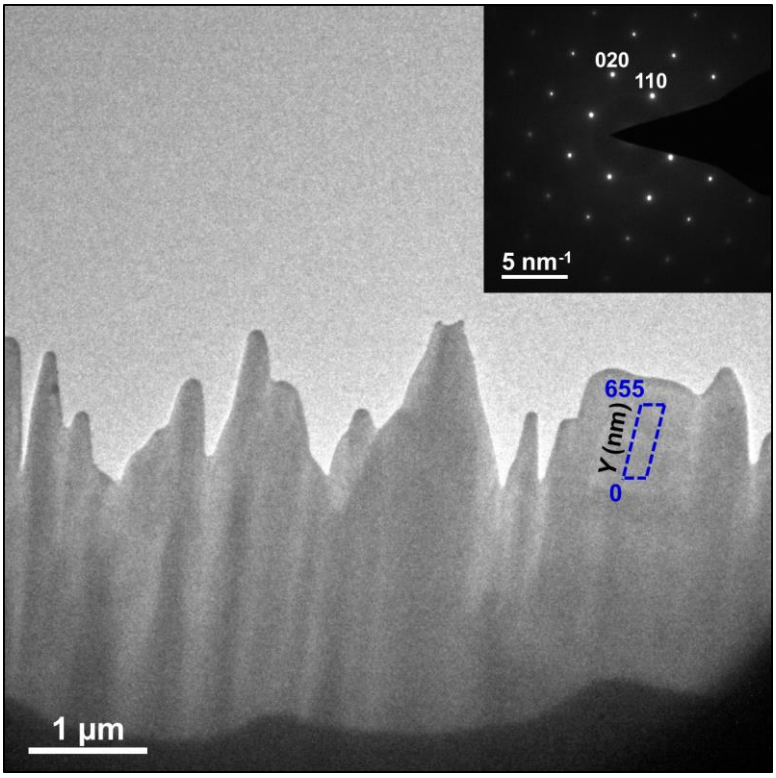

Figure 4.8 A representative UEM bright-field image obtained with femtosecond photoelectrons and a CTEM PBED pattern along [001] orientation (inset) obtained with thermionic electrons from a LaFeAsO TEM Lamella. The dashed blue box represents the region to calculate the time-resolved integrated image intensity in panel (a) of Figures 4.9, 4.11 and 4.12.

In the femtosecond experiments, an altogether different dynamics was observed in comparison to the nanosecond experiments (refer Video S4.1). Coherent propagating contrast waves, originating at the vacuum-specimen interface and moving down towards the thicker regions of the lamella, were seen. The origination of dynamics at the vacuum-specimen interface and the wave propagation direction was found to be independent of the specimen orientation on TEM holder with respect to the probing electron beam. The results are plotted in the panel (a) of Figure 4.9 as a 3D space-time plot. It can be seen from the space-time plot that there are certain intensity maximas originating after time-zero and going downwards in space while oscillating with time. Each of these intensity maxima going down in space is referred here as a wave-front and there are nearly 7 such wave-fronts noticeable in the space-time plot which are also indexed in Figure 4.12. It can also be noticed from the panel (a) of Figure 4.9 that the slope of each subsequent wave-front changes. Also, the width of individual wave-fronts and the time delay among wave-fronts seem to change spatially from top to bottom of the plot, which is reflected as the spatially varying FFT frequencies in the panel (b).

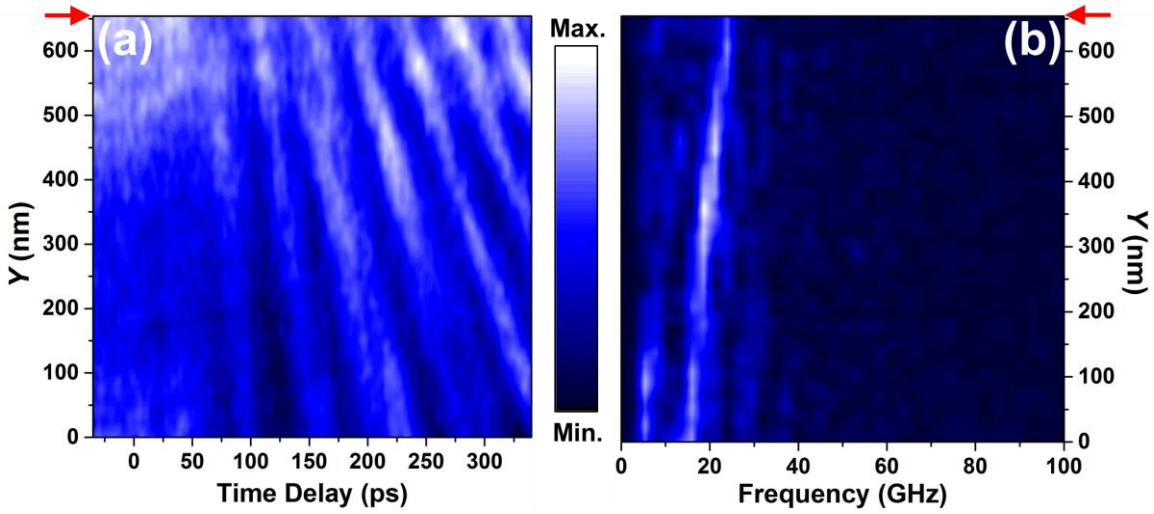

Figure 4.9 (a) Space-time plot of the integrated image intensity obtained from the dashed blue box in Figure 4.8 up to 340 ps. Complete video of the real-space dynamics out to 340 ps can be found in Video S4.1 of the Supporting Information. (b) FFT of the space-time plot in panel (a). The red arrows in panels (a) and (b) highlight the topmost region/slice for the plots in Figure 4.10.

From the 2D plot in Figure 4.10, intensity modulations can be easily seen with time. Interestingly, this intensity modulation doesn't start right after time-zero and initiates around 30 ps. The exact reasons for this delay in dynamics are not known yet. Once the dynamics start after 30 ps, each intensity maxima represents a wave-front and the frequency of this intensity modulation is on the order of gigahertz, three orders of magnitude larger than the frequencies observed in the nanosecond experiments. This suggests that the coherent contrast wave propagation in the specimen is not from the transverse Eigen modes.

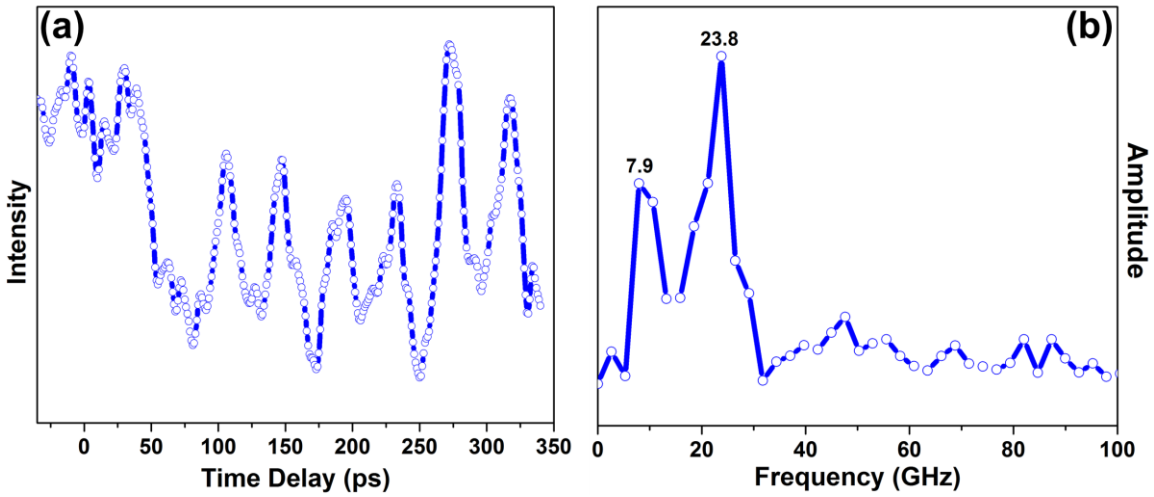

Figure 4.10 (a) Plot showing the variation of image intensity with time for the region/slice highlighted with red arrow in panel (a) of Figure 4.9. (b) Plot depicting the FFT from the region/slice highlighted with red arrow in panel (b) of Figure 4.9.

Importantly, the intensity modulation due to coherent contrast wave propagation decays after 500 ps in the thicker regions of the specimen and can be seen in the Figure 4.11 (refer Video S4.2). Therefore, 500 ps could be approximately considered as the relaxation time for the decay of coherent contrast wave propagation (in the thicker regions) in the bright-field femtosecond dynamics of LaFeAsO. This relaxation time would be useful in the future to understand the role of lattice vibrations (phonons) on the tetragonal-to-orthorhombic transition by comparing the time-scales involved with the structural transition and the phonon relaxation.

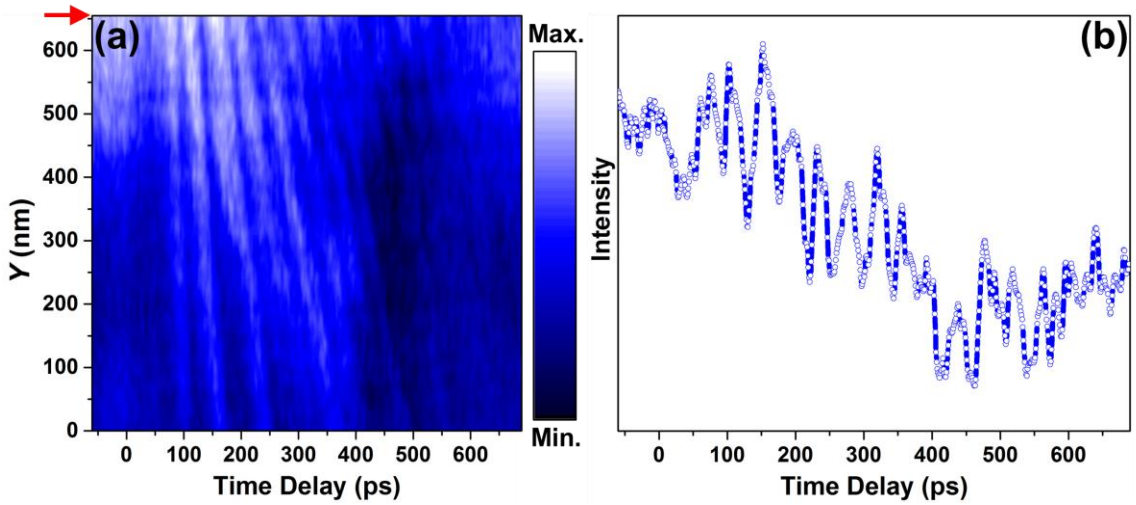

Figure 4.11 (a) Space-time plot of the integrated image intensity obtained from the dashed blue box in Figure 4.8 up to 689 ps. The red arrow highlights the region/slice for the plot in panel (b). Complete video of the real-space dynamics out to 689 ps can be found in Video S4.2 of the Supporting Information. (b) Plot showing the variation of image intensity with time for the region/slice highlighted with red arrow in panel (a).

Wave-front velocities were estimated from Figure 4.12 and are in the range 6 – 22 nm/ps (or 6000 – 22000 m/s). It can be seen from the panel (b) that the estimated velocities decrease with subsequent wave-front number due to a decrease in the slope. In other words, wave-front velocity is decreasing over time (Figure 4.12 (b)) and the frequency of their oscillation is decreasing as we move towards the thicker regions of the specimen (Figure 4.9 (b)). Although the order of the estimated velocity (except 22 nm/ps and 12 nm/ps) is close to the theoretical speed of sound (longitudinal 5090 m/s and shear 2900 m/s) in polycrystalline LaFeAsO [110], but a more rigorous velocity calculation approach is required to quantify the wave-front velocity from experiments because the

longitudinal speed of sound in diamond is 18000 m/s and the present estimated velocity of 22 nm/ps is exceeding it. Currently, an absence of the literature value of speed of sound in single-crystal LaFeAsO doesn't allow for an explanation of the very high values of 22 nm/ps and 12 nm/ps. But the close correspondence of the high-order wave-front velocities to the bulk, in-plane speed of sound indicates that the contrast dynamics arise from propagating acoustic phonons in LaFeAsO.

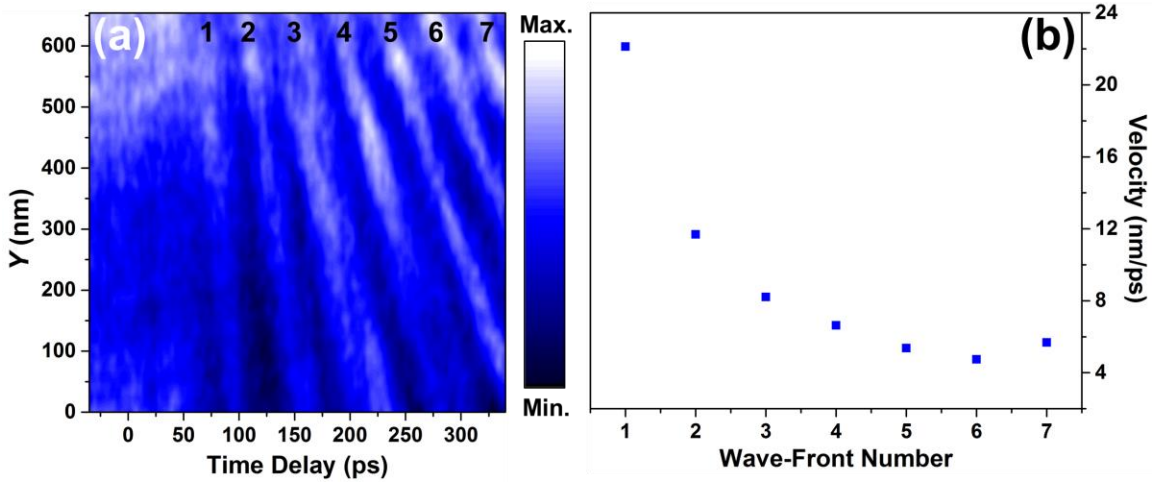

Figure 4.12 (a) Plot from panel (a) of Figure 4.9. The numbers highlight the sequence of wave-front originating at the top of the dashed blue box in Figure 4.8. (c) Velocity estimation for each wave-front marked in panel (a) based on the slope of line passing through the intensity maxima of each wave-front from top to bottom of the dashed blue box in Figure 4.8.

To quantify the spatial variation of specimen thickness, a low-loss EELS line-scan was acquired in the direction of contrast wave propagation which yielded a relative

variation in thickness. To get the absolute thickness values, SEM images along the top-view of LaFeAsO TEM lamella were taken to elucidate the thickness of the topmost part of TEM lamella. Therefore, low-loss EELS in conjunction with SEM images showed the complete spatial thickness variation as summarized in Figure 4.13. This spatial thickness mapping is helpful in comprehending the slowing down of the acoustic phonon frequencies in the thicker specimen regions, and suggests a presence of multiple phonon modes leading to morphologically dependent dispersion and hence splitting of phonon modes in the thicker regions. Similar behavior was observed on another layered materials WSe_2 [111].

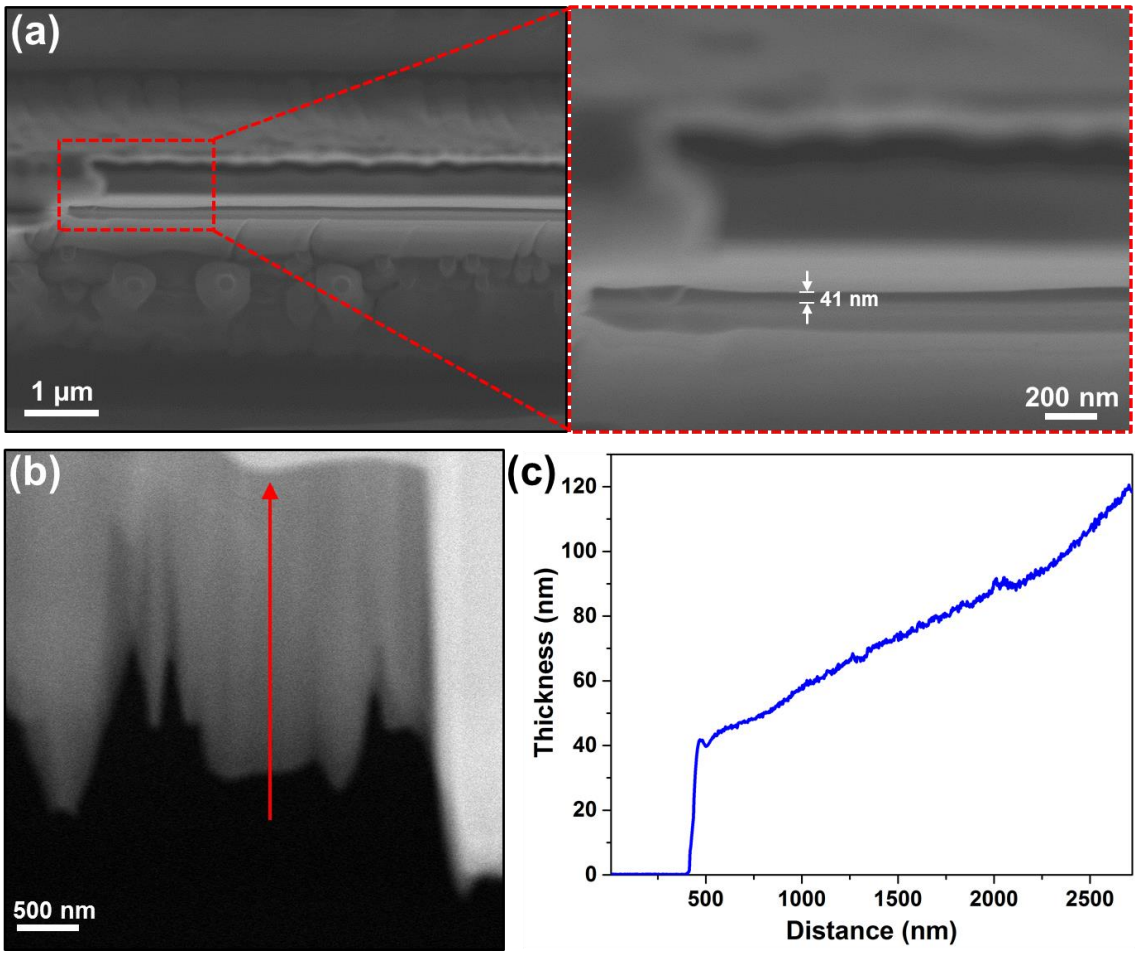

Figure 4.13 (a) SEM images showing the top-view of the LaFeAsO TEM lamella. The dashed red box represents the region of interest for the low-loss EELS measurement in panel (b). The thickness of the top-most part of lamella is 41 nm as marked in the zoomed view of the red dashed box. (b) A HAADF-STEM image showing the side-view of the region of interest in the dashed red box of panel (a). The red arrow shows the direction of low-loss EELS measurement. (c) Plot showing the thickness of the LaFeAsO TEM lamella along the red arrow in the panel (b). Note that the position at 0 nm corresponds to the origin of the arrow.

Femtosecond bright-field imaging experiments were also performed along a different crystal orientation of LaFeAsO which is very close to [100] as depicted in the inset PBED pattern of Figure 4.14. In this configuration also the propagating contrast features were observed similar to that of [001] orientation, but not originating from the vacuum-specimen interface (refer Video S4.3). The exact reasons for the origin of dynamics at another interface are not clear yet. Spatial variation of specimen thickness has not been studied yet along this crystal orientation with low-loss EELS.

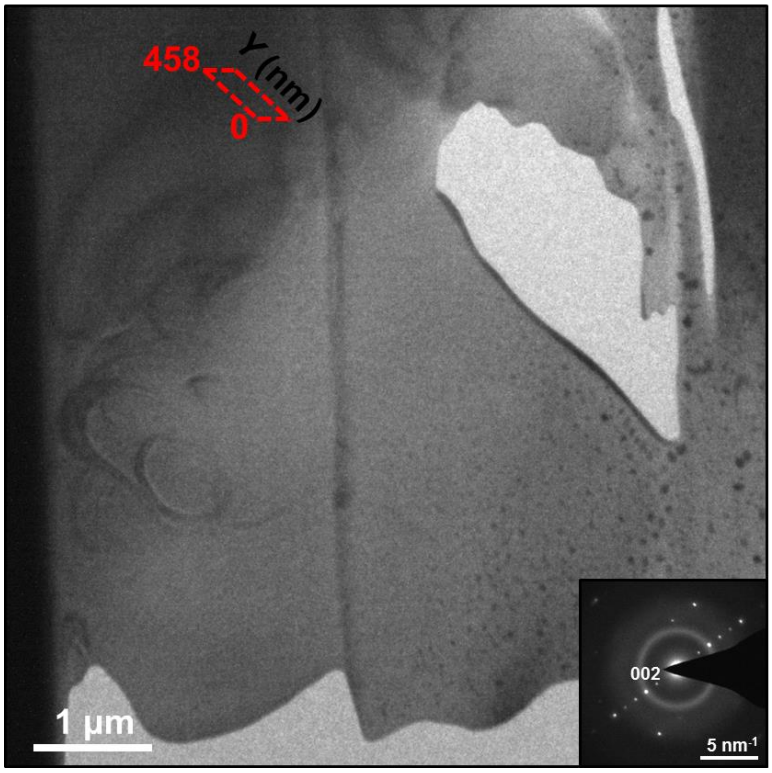

Figure 4.14 A UEM bright-field image obtained with femtosecond photoelectrons and a CTEM PBED pattern nearly along [100] orientation (inset) obtained with thermionic electrons from a LaFeAsO TEM Lamella. Note that this TEM lamella was made based

on the lift-out technique. The dashed red box represents the region to calculate the time-resolved integrated image intensity in panel (a) of Figures 4.15 and 4.16.

Interestingly, spatial and temporal variations in the intensity of propagating contrast waves can be seen from the panel (a) of Figure 4.15 which again leads to a morphologically dependent dispersion and hence splitting of phonon frequency modes (Figure 4.15 (b)). Velocity estimation for various wave-fronts yield 8 – 58 nm/ps (Figure 4.16), which is significantly higher than the longitudinal speed of sound in diamond. This again suggests the development of a more rigorous method for velocity estimation.

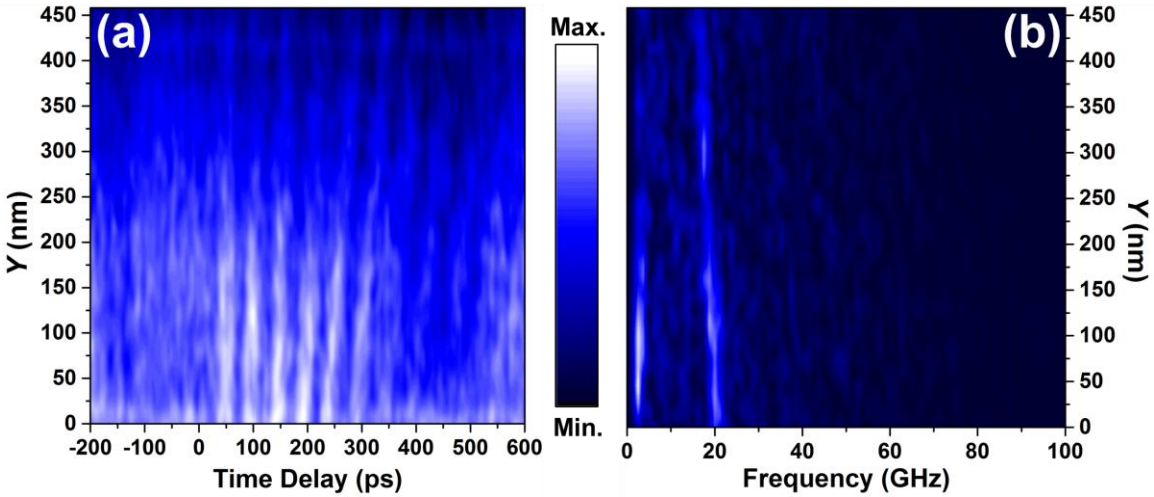

Figure 4.15 (a) Space-time plot of the integrated image intensity obtained from the dashed red box in Figure 4.14 up to 600 ps. Complete video of the real-space dynamics out to 600 ps can be found in Video S4.3 of the Supporting Information. (b) FFT of the space-time plot in panel (a).

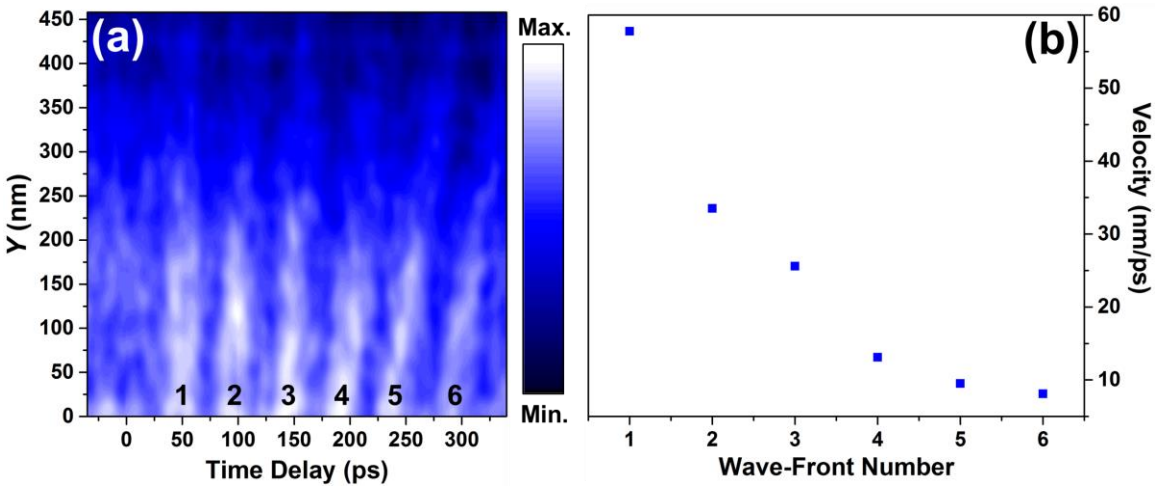

Figure 4.16 (a) Plot from panel (a) of Figure 4.15 up to 340 ps. The numbers highlight the sequence of wave-front originating from the bottom of the dashed red box in Figure 4.14. (c) Velocity estimation for each wave-front marked in panel (a) based on the slope of line passing through the intensity maxima of each wave-front from bottom to top of the dashed red box in Figure 4.14.

4.3.4 Femtosecond Electron Diffraction.

The LaFeAsO response in reciprocal-space was also studied along [001] orientation. Figures 4.17-4.23 summarize the results. In Figures 4.18-4.20 diffraction spots from three different crystallographic families – {220}, {110} and {200} – were studied over 3 different time regimes. In Figures 4.21-4.23 three pairs of diffraction spots symmetric about the central beam were studied over 2-3 different time regimes. This was done to get a comprehensive picture of the diffraction behavior for each low-index diffraction spot.

A decrease in diffraction spot intensity upon laser illumination depicts lattice heating as suggested by the Debye Waller effect studied with UEM previously [112]. This was clearly seen for the {220} family of diffraction spots (Figure 4.18 (a)), but not precisely for {110} and {200} family of diffraction spots (Figure 4.19 (a) and Figure 4.20 (a)). An increase or an oscillation in diffraction spot intensity after time-zero doesn't convey a physical meaning yet. Moreover, a thermal recovery after lattice heating is expected which means a relaxation of the decreased diffraction spot intensity to the pre-time-zero values. This behavior is not obvious for {220}, {110} and {200} family of diffraction spots (panel (c) of Figures 4.18-4.20). Therefore, more experiments are required to get better statistics and/or improvements in the present data analysis techniques might give a clearer picture.

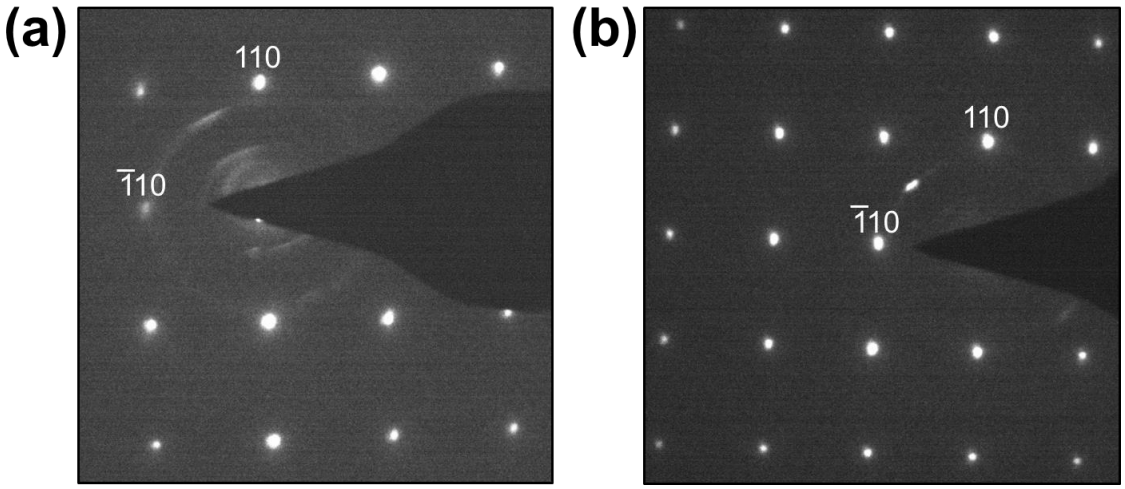

Figure 4.17 (a) A representative PBED pattern for experiments with 5 ps (-160 to 240 ps) and 20 ps (-360 to 2040 ps) time-steps and acquired with femtosecond photoelectrons. (b) A representative PBED pattern for experiments with 0.5 ps time-steps (-20 to 100 ps)

and acquired with femtosecond photoelectrons. The faint circles around the beam block in panel (a) and (b) might be due to the photoelectrons ejected from the uneven surfaces on the LaB_6 filament and/or due to amorphous layers around LaFeAsO crystal in the TEM lamella from FIB specimen preparation.

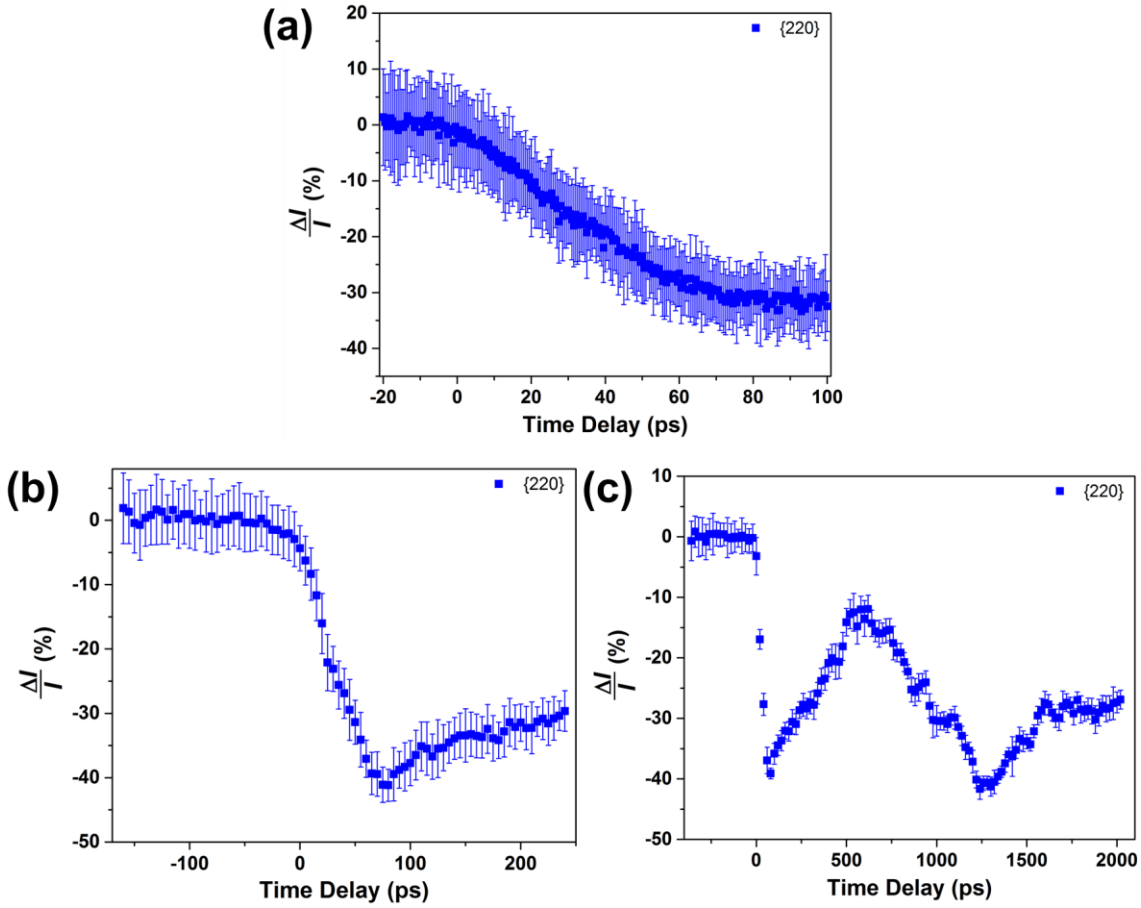

Figure 4.18 (a, b, c) Femtosecond PBED dynamics showing the changes in intensity of *220* family of diffraction spots over three different time regimes. The error bars in panels (b) and (c) are standard deviation values from 10 scans/experiments, and in panel (a) from 6 scans/experiments.

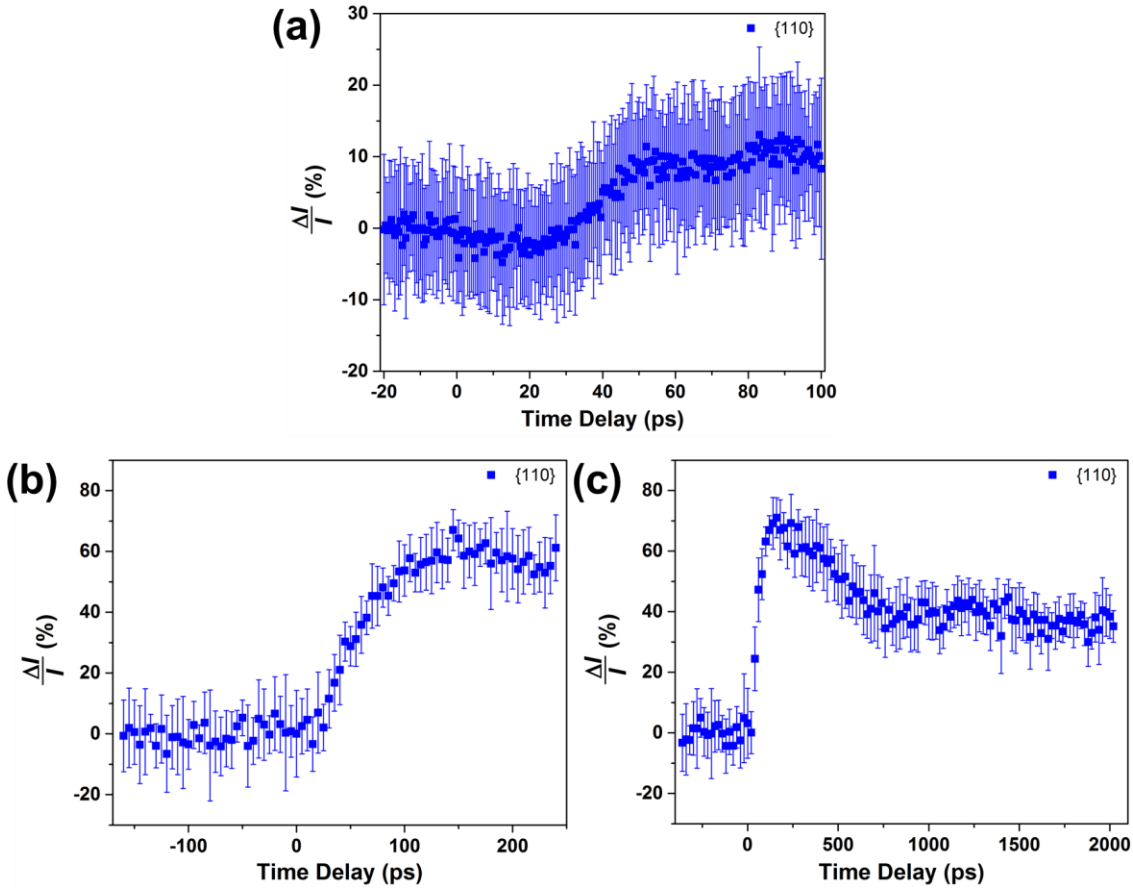

Figure 4.19 (a, b, c) Femtosecond PBED dynamics showing the changes in intensity of *110* family of diffraction spots over three different time regimes. The error bars in panels (b) and (c) are standard deviation values from 10 scans/experiments, and in panel (a) from 6 scans/experiments.

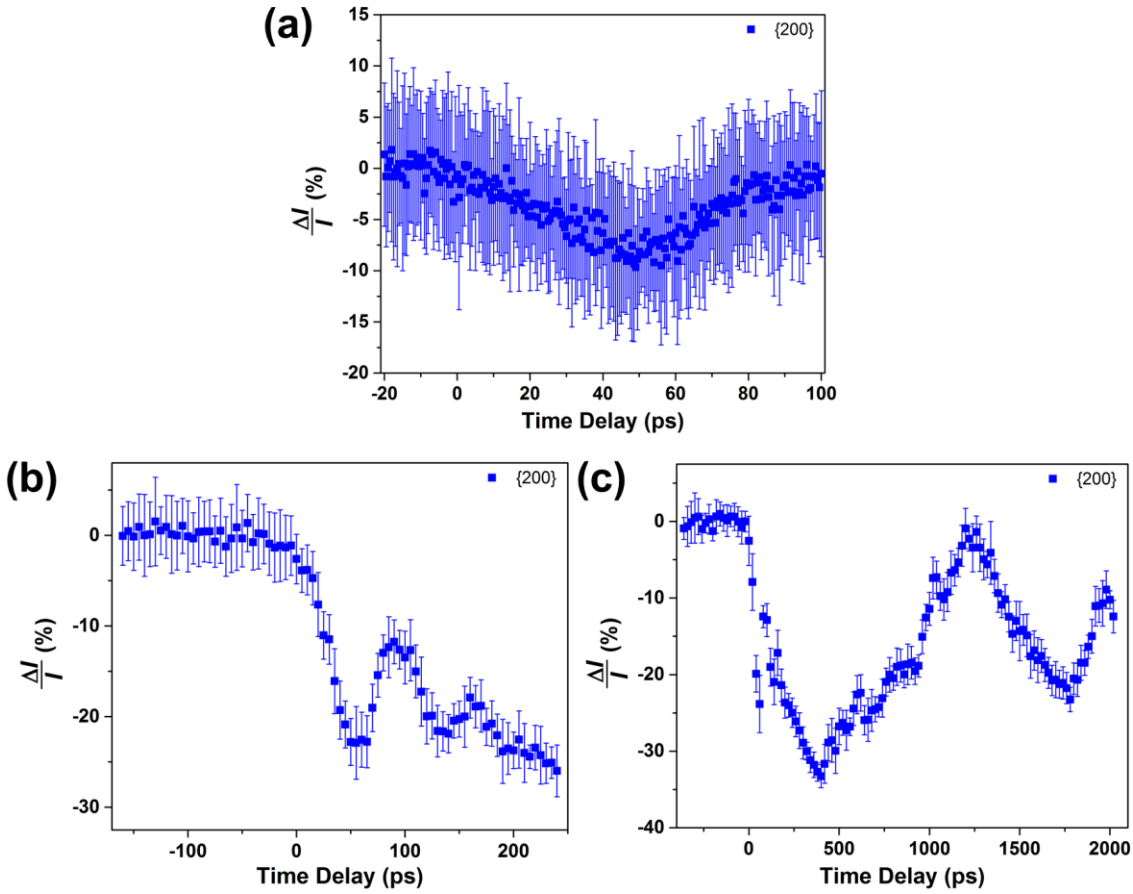

Figure 4.20 (a, b, c) Femtosecond PBED dynamics showing the changes in intensity of *200* family of diffraction spots over three different time regimes. The error bars in panels (b) and (c) are standard deviation values from 10 scans/experiments, and in panel (a) from 6 scans/experiments.

Changes in the *d*-spacing values were also tracked in the reciprocal space for 3 pairs of diffraction spots. A decrease in the magnitude of the reciprocal space vector after laser illumination indicates lattice heating which can be seen in Figures 4.21-4.23 but significant oscillations after time-zero can't be explained yet for all the 3 pairs and no physical explanation could be attributed to it now. Therefore, more experiments and/or

improvements in the present data analysis techniques are recommended to get a clearer picture.

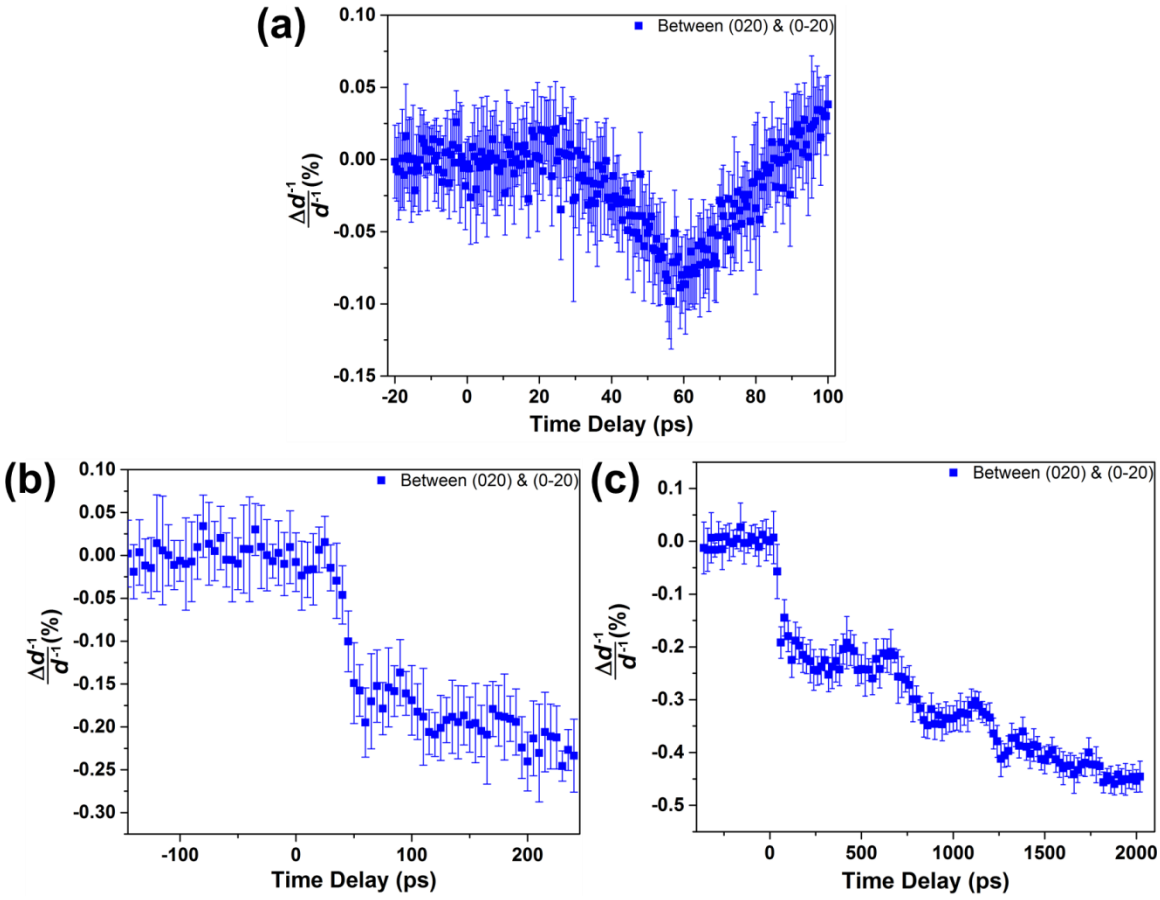

Figure 4.21 (a, b, c) Femtosecond PBED dynamics showing the changes in distance between *020* and *0$\bar{2}$0* diffraction spots on the reciprocal space (or diffraction space) over three different time regimes. The error bars in panels (b) and (c) are standard deviation values from 10 scans/experiments, and in panel (a) from 6 scans/experiments.

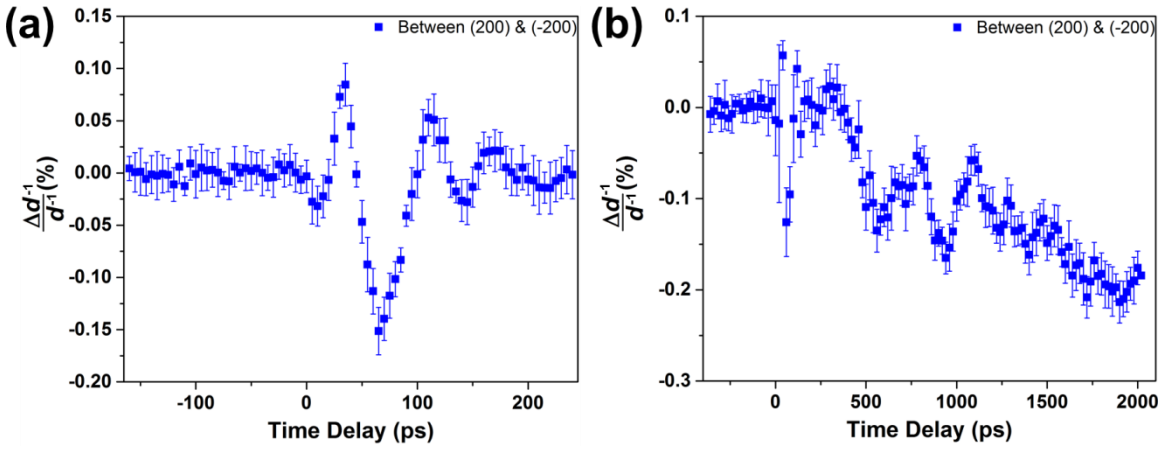

Figure 4.22 (a, b) Femtosecond PBED dynamics showing the changes in distance between *200* and $\bar{2}00$ diffraction spots on the reciprocal space (or diffraction space) over two different time regimes. The error bars in panels (a) and (b) are standard deviation values from 10 scans/experiments.

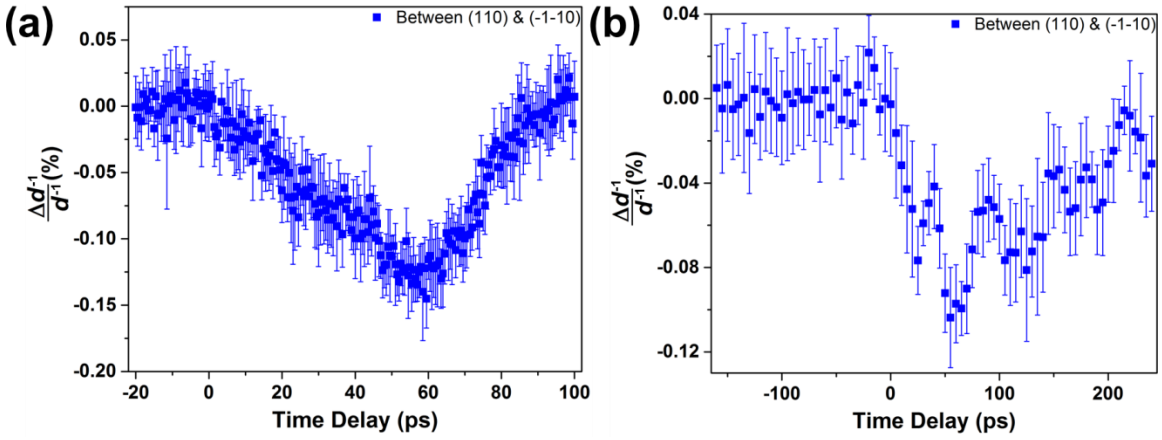

Figure 4.23 (a, b) Femtosecond PBED dynamics showing the changes in distance between *110* and $\bar{1}\bar{1}0$ diffraction spots on the reciprocal space (or diffraction space) over

two different time regimes. The error bars in panels (a) and (b) are standard deviation values from 10 scans/experiments.

4.4 Summary

Nanosecond bright-field imaging and PBED structural dynamics along [001] crystal orientation of LaFeAsO suggest that there are transverse vibrational megahertz frequencies present after laser illumination. Thermal recovery of LaFeAsO happens in nearly 10 μs and is coupled with the megahertz transverse mechanical vibrations. Nanomechanical vibrations result in *d*-spacing variations at megahertz frequencies in the diffraction patterns due to the changes in the eucentric height of the specimen on TEM holder, and this should not be considered as a new structural phase and not be confused with the *d*-spacings of nematic phases in future studies.

Femtosecond bright-field imaging dynamics along [001] and [100] crystal orientations show the propagation of acoustic phonons in the form of coherent contrast feature movement. For the [001] oriented crystals, initiation of the phonon dynamics occurs at the vacuum-specimen interface in the absence of initial bend contours, and the acoustic phonon wave propagation direction is towards the thicker regions of the TEM specimen irrespective of the specimen orientation on TEM holder. Phonon dynamics were found to decay after 500 ps in the thicker specimen regions. For the [100] oriented crystals, phonon dynamics appear to originate inside the TEM specimen rather than at the vacuum-specimen interface and to propagate towards the thicker specimen regions. Spatially varying specimen thickness was found in the TEM lamella of [001] oriented

crystal which is expected to result in variable phonon frequencies and suggest a presence of multiple phonon modes in different parts of the crystal. PBED dynamics are not fully understood at this time, but more experiments and refinement in the present data analysis techniques is underway. The current, real-space, ultrafast results on LaFeAsO are the first of its kind and could provide a reference starting point for future detailed studies.

4.5 Future Directions

There are multiple future research possibilities with the femtosecond experiments. Firstly, it would be interesting to understand why dynamics appear to originate at the vacuum-specimen interface for [001] oriented tetragonal LaFeAsO crystal but not at the vacuum-specimen interface for [100] oriented crystal. This might require fabrication of TEM specimens of [100] orientation with the same boundary condition as that of [001] orientation (clamped on three sides and free on one end) to eliminate the additional variables. With bright-field imaging experiments, understanding the presence of various phonon modes and their frequencies in tetragonal LaFeAsO along different orientations – [001], [100], [110] – as a function of crystal thickness might be interesting to look into. This could be a stepping stone towards understanding the role of electron-phonon coupling in the correlated magnetic and structural phase transitions via experiments. Performing PBED femtosecond experiments in tandem with bright-field imaging could also provide further insights into the electron-phonon coupling in tetragonal LaFeAsO since diffraction spot intensities are a good measure of lattice heating. Similar studies on another iron-pnictide parent compound, $BaFe_2As_2$, have already been conducted [113,

114].

Performing all the above experiments with a liquid-nitrogen TEM holder could allow the real- and reciprocal-space observation of structural phases around the nematic ordering. These time-resolved experiments could also determine the rate of the structural transitions around nematic ordering, which is a topic of intense debate [70]. Ultrafast studies on the low-temperature orthorhombic phase of $BaFe_2As_2$ have already been carried out in the literature, which suggests a way to quantify the coupling between structural and nematic degrees of freedom [115]. If femtosecond EELS experiments [116-118] could be performed around the nematic ordering, the electronic and structural transitions can be clarified and may explain the unconventional superconductivity in iron-pnictides. Carrying out the femtosecond experiments on doped LaFeAsO and comparing the rate of structural and electronic transitions with undoped LaFeAsO may also be necessary to understand the origins of unconventional conductivity. Ab initio calculations to support the UEM data might also be necessary [117].

Chapter 5

Visualization of Laser-Induced Mechanical Motion in a HAMR Lamella with Ultrafast Electron Microscopy and Mass Density Mapping via Static TEM

5.1 Introduction

Metal-dielectric interfaces have found far-reaching applications in the electronics industry, especially in ICs and FETs [119]. Much emphasis has been placed on understanding the thermal and electrical stability of these interfaces [119]. Due to their unique electrical, thermal and photonic properties, these interfaces are being tested extensively for their use as an optical near-field transducer in an emerging technology called heat-assisted magnetic recording (HAMR) [120, 121]. This technology aims to increase the storage capacity of magnetic hard drives by several orders of magnitude. To make HAMR feasible for commercial applications, an understanding of the interfaces' reliability and response to laser irradiation on ultrafast (femtosecond to microsecond) timescales is required because this technology uses temporary laser heating at these ultrafast timescales to boost the hard drive storage density [120, 122]. There are various studies focused on understanding the optical energy conversion and heat transfer across these metal-dielectric interfaces [121, 123-125]. However, the mechanical stability of

these interfaces on the order of picoseconds to microseconds has never been studied due to the lack of techniques that can non-destructively test the devices comprising the metal-dielectric interfaces, but photomechanical actuation of various types have been reported for numerous crystals [126].

Modern electron microscopes and direct-electron detection cameras can probe the dynamics of material systems at the atomic-scale with millisecond temporal resolution [6, 127]. However, the limited read-out rate of these state-of-the-art cameras prevents traditional electron microscopes from observing motion with frequencies on the order of kilohertz to gigahertz [127]. On the other hand, ultrafast techniques (e.g. spectroscopy, diffraction) can indirectly probe material dynamics with frequencies on the order of kilohertz to terahertz, but do not provide direct real-space visualization of phenomena occurring on these fast timescales [47, 128]. UEM combines the spatial resolution of electron microscopy with the temporal resolution of other ultrafast techniques, offering an unprecedented, stroboscopic, nondestructive method to observe motion on nano- and femto-second timescales [31, 34-36, 46].

Using UEM, various nanomechanical vibrations with frequencies on the order of megahertz have been observed, including the drumming of graphite sheets [129], the musical overtones of nanoharps and nanopianos [130], and the cantilever motion of individual copper 7,7,8,8-tetracyanoquinodimethane [Cu(TCNQ)] single crystals [131]. However, these systems, which have simple boundary conditions, were mostly prototypical demonstrations of UEM. In this chapter, UEM is employed on a more involved metal-dielectric system obtained out of a HAMR device having complex

boundary conditions and geometry. Mechanical vibrations were directly observed for the whole system in the form of an oscillating diffraction contrast and the frequencies of its vibrational modes are reported. Furthermore, finite element method (FEM) simulations were performed to calculate the natural frequencies of vibration for this complicated system and a close agreement between the simulated and observed frequencies is reported. The close match between UEM experiments and FEM simulations reveals the exact nature of the fundamental (resonance) oscillations in the gold-sapphire TEM specimens. This study provides insight on phenomena unobservable via other ultrafast techniques that could greatly enhance the performance of HAMR devices. In addition, three different signals – high-angle incoherently scattered electrons (HAADF-STEM), low-angle inelastically scattered electrons (EELS), X-rays (XEDS) – scattered off the HAMR lamella were collected via static TEM and were used to map the mass density of the gold near-field transducer (NFT), present in the HAMR devices. An inhomogeneous mass density distribution was found which could potentially prove useful in tailoring the synthesis process of gold NFT in HAMR devices.

5.2 Methods

5.2.1 Specimen Preparation.

The specimens were cut out of a HAMR device into TEM lamella using focused ion beam (FIB) milling and were transferred to silicon nitride TEM grids using a micromanipulator. A coating of platinum was applied during focused ion beam (FIB) milling to protect the gold-sapphire metal-dielectric system from gallium ion beam

damage. The TEM specimen preparation was done at Seagate Technology LLC, Bloomington, MN.

5.2.2 Microscope Parameters.

All the UEM experiments were performed in a Tecnai Femto ultrafast electron microscope (FEI Company) operated at 200 kV in both thermionic and photoelectron modes. In these emission modes, a truncated, 150 μm flat LaB_6 cathode (Applied Physics Technologies) was used. A Gatan Orius 2048 × 2048 CCD camera was used to record the images with integration times ranging from 1 to 20 seconds per frame.

HAADF-STEM imaging, low-loss EELS and XEDS experiments were performed in an FEI Tecnai G2 F30 microscope operated at 300 kV, and equipped with Gatan Enfina EEL spectrometer and EDAX rTEM XEDS system having an ultrathin-window Si(Li) detector. For HAADF-STEM imaging, a low camera length of 80 mm was employed to avoid the exposure of diffraction spots on the HAADF detector. This was needed to get intensity solely from the *Z*-contrast of specimen. Another FEI Technai G2 F30 operated at 300 kV and having a 4096 × 4096 ultrascan CCD camera was also used for bright-field imaging and selected area diffraction patterns.

5.2.3 Laser Parameters.

The gold-sapphire specimens were optically excited *in situ* with a pump pulse of 250 fs duration full-width at half-maximum (FWHM) and centered at 515 nm. A Yb:KGW (1030 nm fundamental output), diode-pumped solid-state laser and a custom harmonics generation module were used to generate the pump pulses. Pump fluences of

15.4 mJ/cm^2 were incident on the specimen. At these incident wavelengths, gold and platinum are the primary absorbers of the pump pulses.

Probe pulses were generated with a Nd:YAG (1064 nm fundamental output), Q-switched, diode-pumped solid-state laser. The fourth harmonic was generated on the laser table and was used to generate the photoelectrons out of the LaB_6 cathode for image formation. All the UEM experiments were performed at the slowest possible repetition rate of 2 kHz currently available in our system to ensure maximum mechanical and thermal relaxation before each subsequent excitation, and all the UEM images were acquired with 1 ns time-steps.

5.2.4 Data and Image Processing.

In order to accurately depict and analyze the real-space UEM dynamics, we first drift-corrected the raw images with sub-pixel resolution and then passed them through a 10-pixel Gaussian low-pass filter.

5.3 Results and Discussion

5.3.1 Visualization of Mechanical Vibrations via UEM.

The morphology of a HAMR lamella is depicted in Figure 5.1 where the electron transparent region at the center of the lamella contains sapphire, the gold NFT, and a platinum capping layer. The HAMR lamella is placed on a silicon nitride (Si_3N_4) TEM window. Furthermore, the geometry and crystalline order of the HAMR lamella before and after laser illumination is discussed in detail in Figures 5.2 and 5.3, respectively.

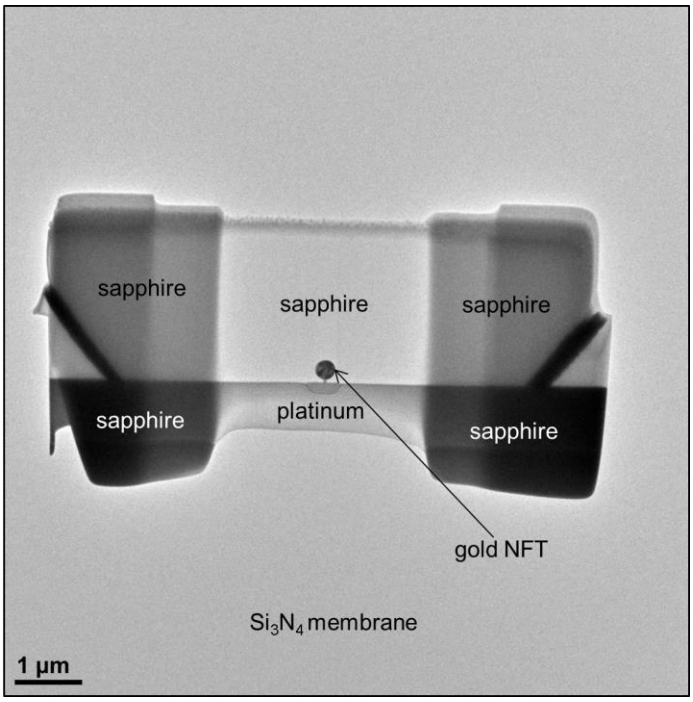

Figure 5.1 Bright-field TEM image showing an overview of HAMR lamella lying on silicon nitride TEM grid.

Figure 5.2(a) shows a HAMR lamella before performing the UEM pump-probe experiments with laser illumination on specimen. Figure 5.2(b) depicts a higher-magnification image of the lamella where the crystalline gold NFT is embedded in amorphous sapphire. The diameters of the gold NFTs studied were found to be between 200 and 300 nm. Figure 5.2(c) shows a higher-magnification image of the surrounding regions of gold NFT. Corresponding selected-area diffraction patterns (SADPs) from the representative regions of gold, tungsten and platinum confirm their crystalline nature. The platinum capping layer is polycrystalline as confirmed by the presence of Debye-Scherer rings for all the expected Bragg planes, as is the tungsten in proximity of gold NFT. The gold NFT embedded in the sapphire matrix is a randomly-oriented crystal (not

along a definite crystal zone-axis) having approximately 2-5 grains. The grain boundaries in the gold could be seen from the higher-magnification image in Figure 5.2(b). Sapphire surrounding the gold NFT was confirmed to be amorphous from the texture and Fourier transform of a higher-magnification bright-field image, and also from a complete absence of diffraction contrast.

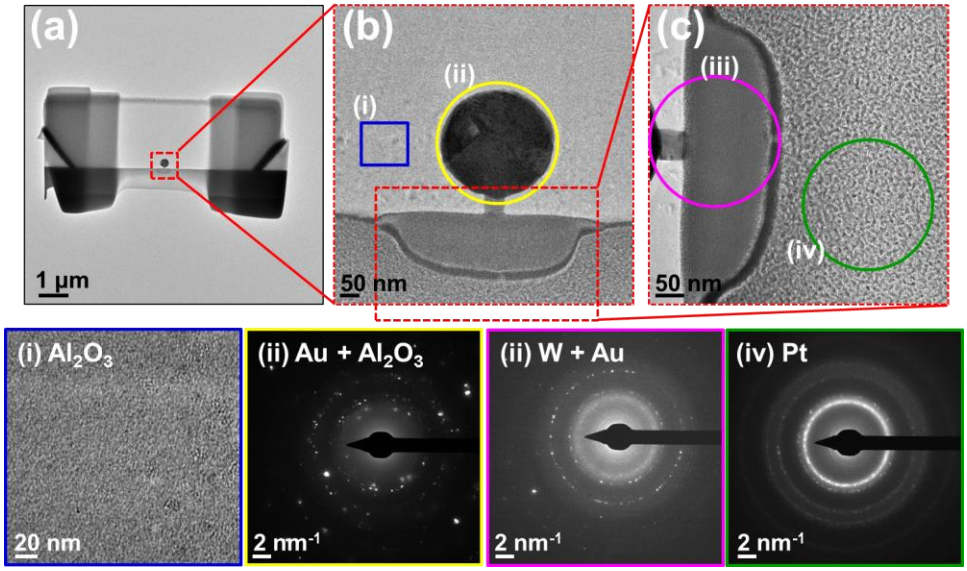

Figure 5.2 Geometry and crystalline order of the HAMR lamella before laser illumination. (a,b,c) Bright-field images of the HAMR lamella. The red, dashed square in (a) denotes the region for image acquisition of (b), and the one in (b) denotes the region for image acquisition of (c). The colored, solid square and circle in (b) - blue, yellow - depict the positions for image acquisition and of selected-area aperture for (i) bright-field image of amorphous sapphire (Al_2O_3) and for the acquisition of diffraction pattern from a representative region of (ii) crystalline gold embedded in amorphous sapphire (Au + Al_2O_3), respectively. The colored, solid circles in (c) – pink, green -

depict the positions of the selected-area aperture for the acquisition of diffraction patterns from a representative region of (iii) polycrystalline tungsten in proximity of gold (W + Au) and (iv) polycrystalline platinum (Pt), respectively. Note that the smallest selected area aperture is larger than the tungsten region in HAMR lamella.

Figure 5.3(a) shows the specimen used for UEM pump-probe experiments. Upon laser illumination, a transition in crystalline morphology occurred. Figure 5.3(b) depicts a higher-magnification image of the specimen where a gold disk approximately 260 nm in diameter is embedded in sapphire. Corresponding selected-area diffraction patterns (SADPs) from the representative regions of platinum, sapphire and gold confirm their crystalline order – the platinum is predominantly polycrystalline (incomplete formation of Debye-Scherer rings for all the expected Bragg planes), the sapphire is nearly polycrystalline (faint and missing Debye-Scherer rings for the expected Bragg planes), and the gold disk embedded in the sapphire is a randomly-oriented crystal (not along a definite crystal zone-axis). The small particles of the platinum were used as stationary reference points to drift-correct the raw images for showing UEM dynamics. It was concluded that a crystallization of sapphire (leading to an origin of diffraction contrast features around gold NFT) and a coalescence of small platinum grains into larger ones occurred after laser illumination. Damage to tungsten region can also be observed, and it is hypothesized that a diffusion of elements may have occurred after laser illumination. For the UEM studies, the specimen shown in Figure 5.3 was used.

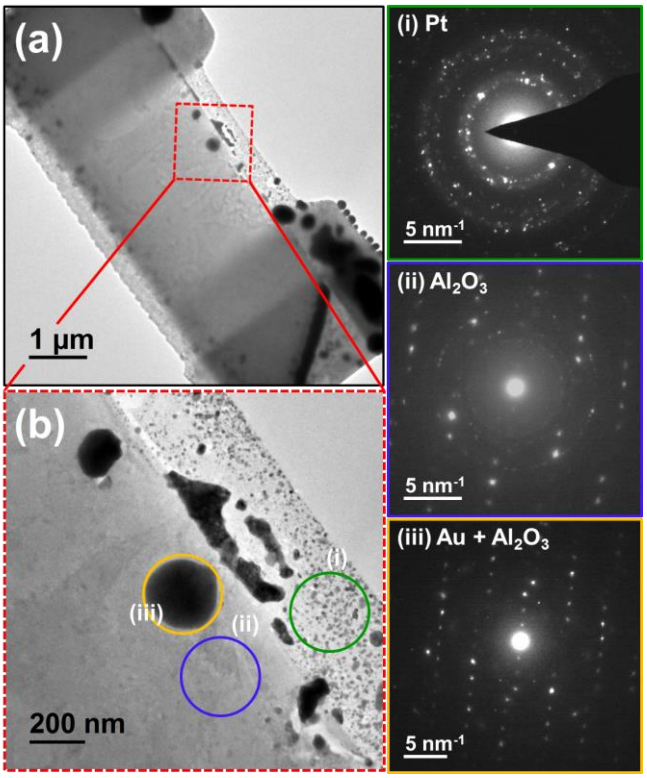

Figure 5.3 Geometry and crystalline order of the HAMR lamella after laser illumination. (a,b) Bright-field images of the metal-dielectric system. The red, dashed square in (a) denotes the region for image acquisition of (b). The colored, solid circles in (b) - green, blue, yellow - depict the positions of the selected-area aperture for the acquisition of diffraction patterns from a representative region of (i) platinum (Pt), (ii) sapphire (Al_2O_3), (iii) gold embedded in sapphire (Au + Al_2O_3), respectively.

Figure 5.4 shows the real-space dynamics of the specimen via a sequence of difference images. Images at negative values of time are taken before the arrival of the clocking (pumping) laser pulse, which strikes the specimen at t = 0 ns, and images at

positive values of time show the dynamics resulting from the laser excitation. The difference images are produced by subtracting the reference image, taken 10 ns before the arrival of the clocking laser pulse (t = -10 ns), from the images taken at the times specified by the timestamps in the upper-left corner of each frame. Each difference image corresponds to a point in time after the arrival of the clocking laser pulse. When features in the UEM images evolve with time, the features manifest as dark and bright regions in the difference images. The platinum particles and gold disk did not exhibit observable dynamics and hence appear stationary after the arrival of the clocking laser pulse.

The primary dynamic feature of the images in Figure 5.4 is the oscillatory motion of the diffraction contrast in the sapphire. The absence of contrast features in the difference image at t = 0 ns indicates that negligible motion was present before the arrival of the clocking laser pulse. After the arrival of the clocking laser pulse, the position of the diffraction contrast begins to oscillate. Figure 5.4(a) outlines the oscillations of the diffraction contrast shortly after the arrival of the clocking laser pulse, and Figure 5.4(b) shows the continued behavior over a longer period of time. It will be hypothesized later that this movement of the diffraction contrast results from mechanical vibrations within the specimen induced by the incident laser. As the specimen bends and rotates with time, the angle between the specimen and the probing electron pulse changes. Consequently, the region of the sapphire that satisfies the Bragg condition continuously changes, resulting in a change in local bright-field intensity and hence leading to a relocation of the diffraction contrast with time, as illustrated by the Howie-Whelan equation [41]. We

will demonstrate that the natural frequencies of mechanical vibration within the specimen agree with oscillation frequencies observed in the diffraction contrast.

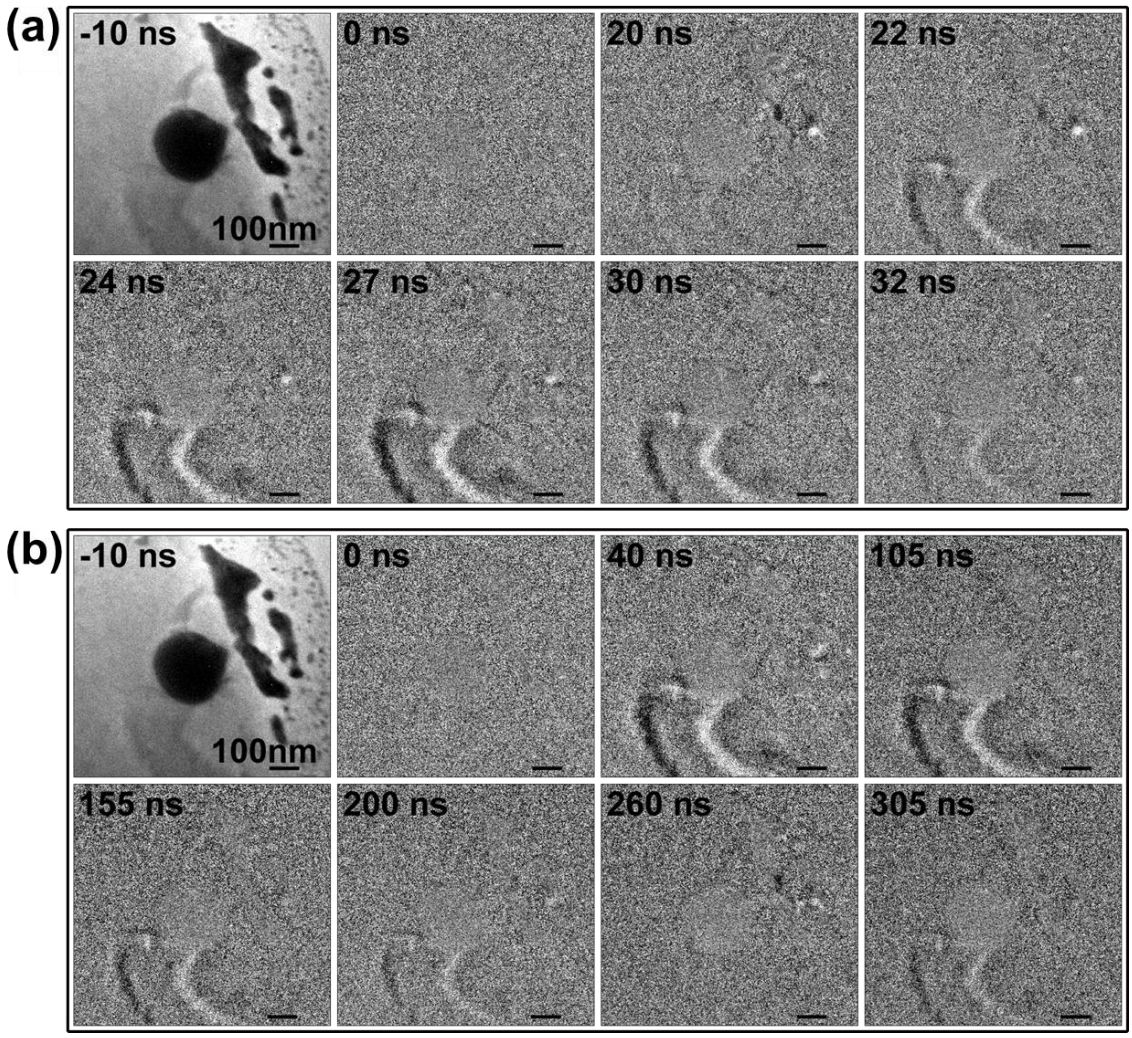

Figure 5.4 Ultrafast electron micrographs of an oscillating diffraction contrast within the polycrystalline sapphire. Two sequences of difference images outline the real-space dynamics observed via UEM. (a) A reference image at t = -10 ns and a sequence of difference images between t = 0 ns and t = 32 ns. The scale bar corresponds to 100 nm in all the images. (b) Long-term dynamics out to a time of 305 ns. The scale bar

corresponds to 100 nm in all the images. Complete videos of the real-space dynamics out to 500 ns and 2331 ns can be found in Videos S5.1 and S5.2, respectively, of the Supporting Information.

Figure 5.5 outlines the process by which the oscillation of the diffraction contrast is quantified. As shown in Figure 5.5(a) and 5.5(b), we begin to analyze the real-space dynamics by extracting a line-profile of integrated pixel intensity across the diffraction contrast in the sapphire. The horizontal-axis of Figure 5.5(b), labeled as X, corresponds to the X-axis of the red, solid rectangle in Figure 5.5(a). The integrated pixel intensity across this rectangle along the X-axis is plotted in red in Figure 5.5(b). We use the nearest neighbor interpolation for determining pixel intensity along diagonal lines. We then fit a Gaussian curve to the leftmost peak of the intensity profile. The center of this Gaussian fit defines the position of the left edge of the diffraction contrast, which is highlighted with a white, dashed ellipse in the inset of Figure 5.5(c). Our UEM imaging data-set comprises 2357 images, and we rotated the data-set such that the red, solid rectangle in Figure 5.5(a) was horizontal across the field of view. For each image we repeat the process of extracting the integrated pixel intensity and fitting a Gaussian curve. As the diffraction contrast displaces with time, the location of the center of the Gaussian fit also changes with time. We produce Figure 5.5(c) by plotting the change in the position of the center of the Gaussian fit, labeled as ΔX, with respect to time over the interval -20 to 500 ns. We define the reference value for calculating ΔX to be the average (mean) position of the Gaussian fits on the time interval -20 to 0 ns. As observed in

Figure 5.4 qualitatively, Figure 5.5(c) displays quantitatively a minimal displacement of the diffraction contrast before the arrival of the clocking laser pulse at t = 0 ns, at which point an oscillatory motion takes place.

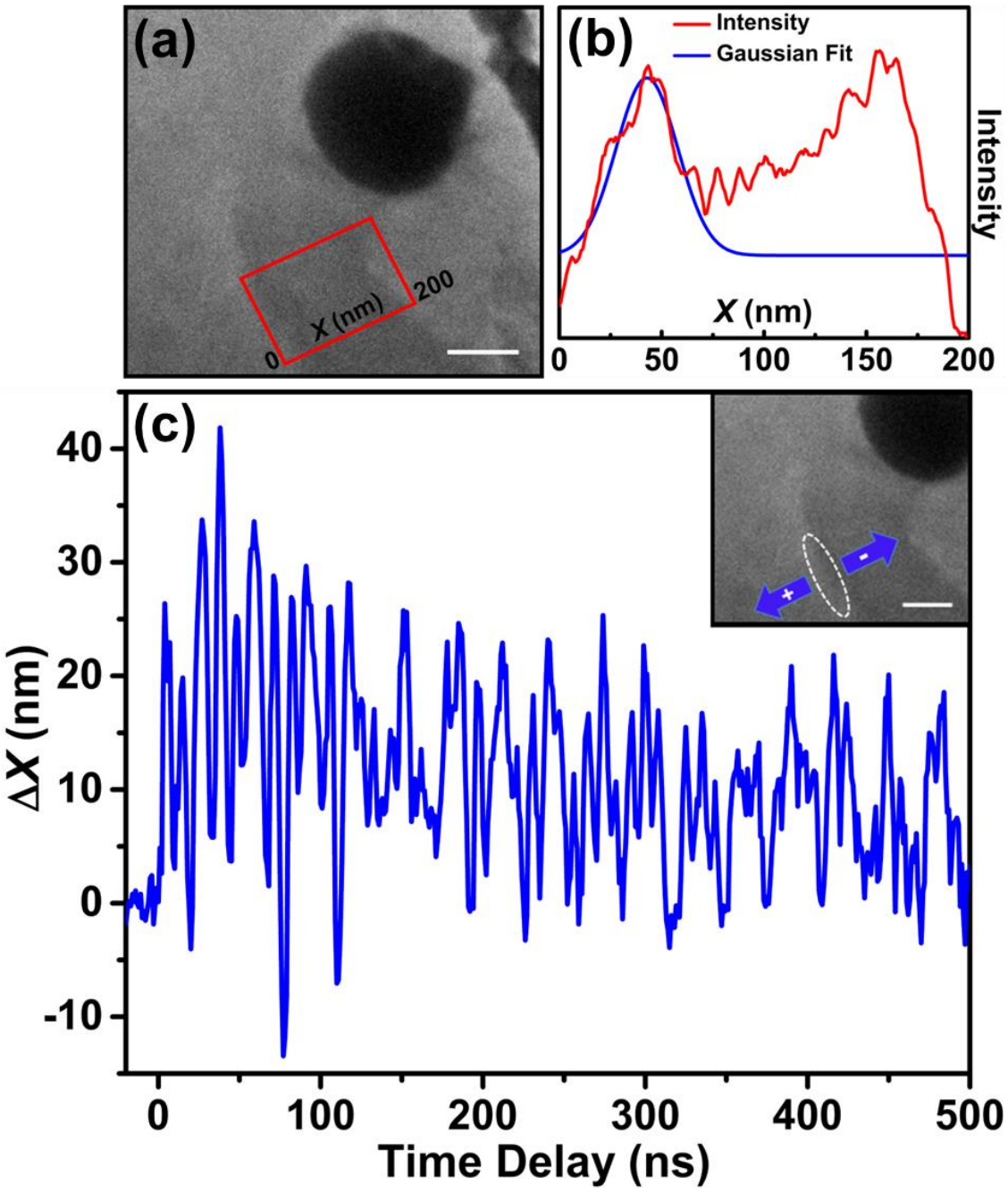

Figure 5.5 Quantification of the motion of the diffraction contrast with respect to time. (a) A representative ultrafast electron micrograph acquired at 400 ns time delay. The red, solid rectangle traversing the diffraction contrast represents the region over which pixel intensity is integrated along the marked *X*-axis. The scale bar corresponds to 100 nm. (b) Plot of integrated pixel intensity (in red) as a function of position along the *X*-axis of the red rectangle in (a) and a Gaussian fit (in blue) to the leftmost peak of the intensity profile. The integrated pixel intensity is plotted in an arbitrary unit in which darker pixels correspond to higher intensity. (c) Plot of relative position of the center of the Gaussian fit, defined as ΔX, for each image in the data-set as a function of time. The inset in (c) is a close-up of the region under inspection. The left edge of the diffraction contrast is highlighted by a white, dashed ellipse, and the two blue arrows with + and – symbols denote the directions of motion of the diffraction contrast which we associate with positive and negative ΔX. The inset scale bar corresponds to 100 nm.

Figure 5.6 extends the methodology outlined by Figure 5.5 to a set of images ranging from -20 to 2331 ns. A notable feature of Figure 5.6(a) is that the center of the oscillation does not remain around 0 nm, but initially displaces upward to approximately 10 nm then appears to settle at about -10 nm. We conceive two possible explanations for this behavior. First, there may be vibrational modes present in the metal-dielectric specimen at frequencies too low to observe using time points out to 2331 ns. Secondly, as heat dissipates from the gold disk to the polycrystalline sapphire, thermal expansion and/or development of residual stresses within the sapphire due to temperature rise may

result in a gradual shift in the location of the diffraction contrast. A more in-depth study of the thermal behavior of the system and a longer period of observation would be necessary to verify either of these possibilities. Nonetheless, the gradual change in position of the center of the oscillation occurs on a time-scale orders of magnitude slower than the high frequency vibrations that are the focus of the present study. Figure 5.6(b) shows a Fast Fourier Transform (FFT) of the plot in Figure 5.6(a) over the time period 0 to 2331 ns. We observe the fundamental frequency at 33.4 MHz, followed by a sequence of overtones at 63.9, 88.3, 114.5, and 119.6 MHz. These frequencies constitute a profile by which we can identify the physical mechanism underlying the mechanical vibrations that cause the oscillation of the diffraction contrast.

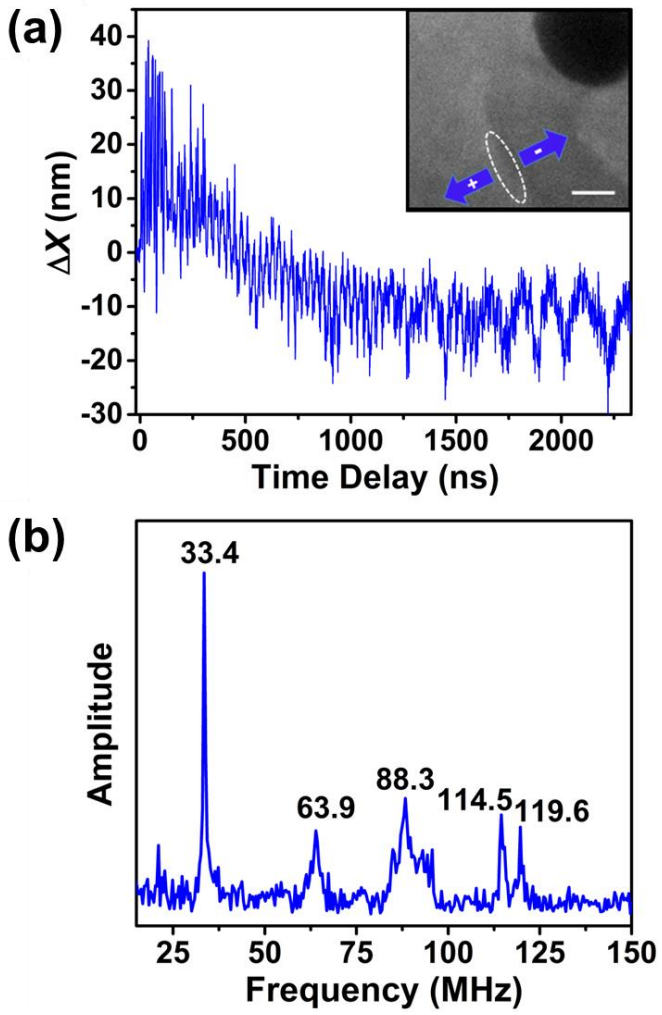

Figure 5.6 Real-space dynamics and vibrational frequencies of the diffraction contrast motion in the HAMR lamella. Using the method described in Figure 5.5, in (a) we plot the relative position of the diffraction contrast, ΔX, as a function of time over the interval -20 to 2331 ns with a step size of 1 ns. The inset scale bar corresponds to 100 nm. (b) shows the vibrational frequencies of the diffraction contrast motion, obtained by performing a FFT over all the positive time-points plotted in (A). We observe 5 prominent frequencies at 33.4, 63.9, 88.3, 114.5, and 119.6 MHz. The FFT has a sampling (or frequency) resolution of 0.2 MHz.

We account for the observed vibrational frequencies in the diffraction contrast by modeling the sapphire and platinum region of the specimen as a thin vibrating plate. As with other structures, such as Euler-Bernoulli beams, which have been the subject of other UEM studies [131], a given thin plate supports a unique set of natural frequencies [132]. The set of frequencies that a given thin plate can support depends on several structural parameters including geometric dimensions, boundary conditions, and material properties [132]. Figure 5.7(a) shows the geometry and boundary conditions that we use to approximate the vibrating region of the specimen. The thin region of the plate is highlighted with a blue, solid square. A solid, blue circle is used to indicate the orientation of the plate in the simulations. We measure this thin region to be a 3.2 μm square and assume a constant thickness of 60 nm. The sapphire region is 2.5 μm wide and the platinum edge is 0.7 μm wide. We model the gold disk as cylinder with a diameter of 260 nm and a thickness of 60 nm. As indicated by the letters C in Figure 5.7(a), we approximate the edges where the vibrating plate region adjoins to the thicker sapphire and platinum sides as clamped (also known as fixed) boundaries. The fixed boundary condition describes boundaries at which no rotation or transverse displacement occurs. We model the remaining two edges with the free boundary condition, denoted by the letter F in Figure 5.7(a), which describes boundaries at which there is neither applied force nor torque. Three material properties are necessary to determine the natural frequencies of a thin vibrating plate: Young's modulus (Y), Poisson's ratio (ν), and density (d). For the materials in our specimen, these material properties are well known

and were obtained from Wikipedia. For polycrystalline sapphire: Y = 390 GPa, v = 0.25, and d = 3.97 g cm^{-3}; for polycrystalline gold: Y = 79 GPa, v = 0.42, and d = 19.3 g cm^{-3}; for polycrystalline platinum: Y = 168 GPa, v = 0.39, and d = 21.45 g cm^{-3}. Here, we take the material properties of polycrystalline gold for simplicity, as the gold disk is randomly oriented along an undetermined crystal-axis.

Using the foregoing material properties, geometry, and boundary conditions to approximate our specimen as a vibrating thin plate, we perform a FEM simulation via COMSOL Multiphysics® to determine the natural frequencies of the transverse vibrations of the system. The finite element model produces a fundamental frequency for the first mode of vibration (n = 1) at 26.1 MHz and overtones at 62.9, 63.9, 88.8, and 113.8 MHz. We compare the simulated natural frequencies (n) to the observed frequencies graphically in Figure 5.7(b). There is excellent agreement between the simulated and observed frequencies, especially given the simplicity of our model. The thin plate defined by the above parameters serves as a first order approximation of the actual mechanical system; a more detailed analysis would account for non-ideal boundary conditions, inhomogeneous material properties, heat transfer, and geometric irregularities. The frequency agreement demonstrates that the observed oscillation in the diffraction contrast in the polycrystalline sapphire results from a mechanical drumming throughout the entire specimen. Figure 5.7(c) shows the mode shapes for each of the natural frequencies predicted by the FEM simulation. The actual vibration present in the specimen is a superposition of these mode shapes that causes the observed oscillation in the diffraction contrast.

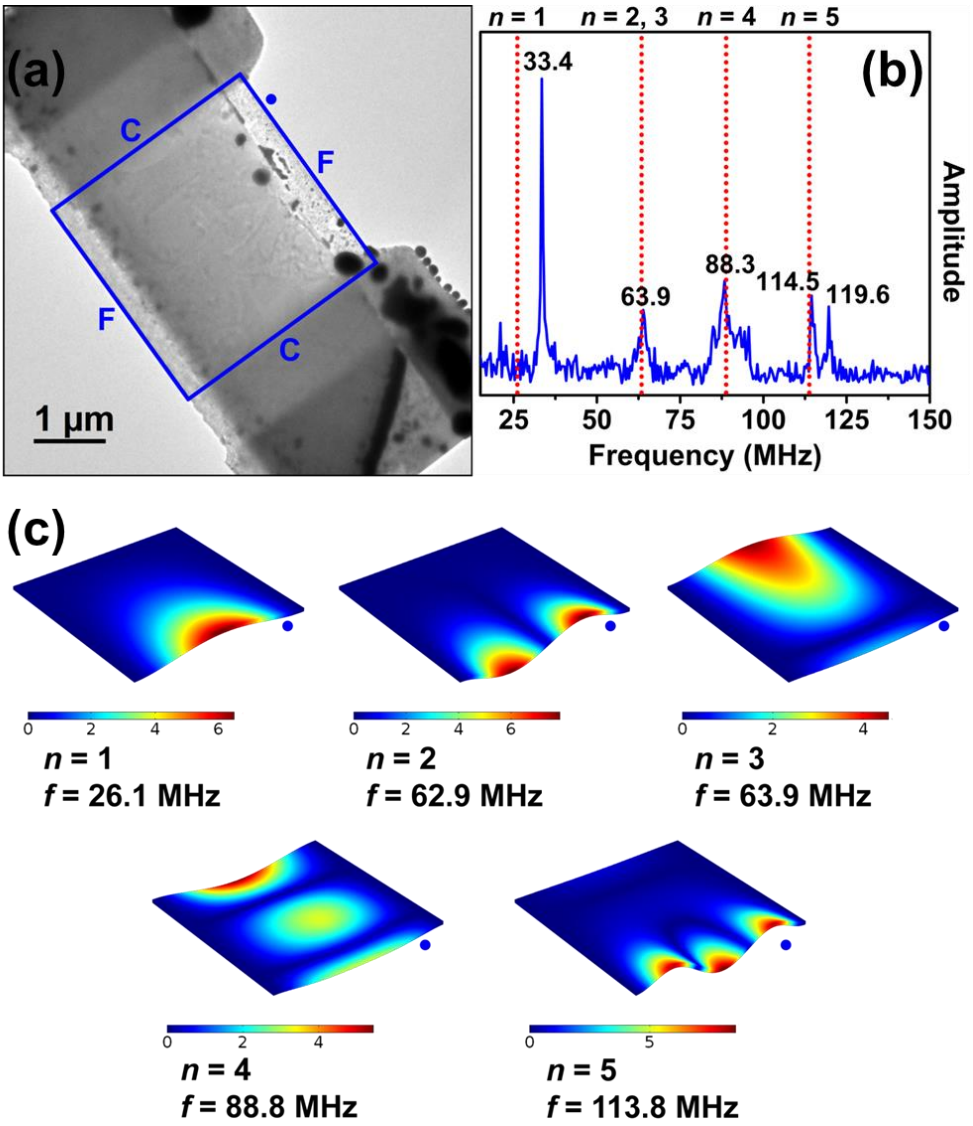

Figure 5.7 Comparison of the vibrational frequencies observed via UEM to the natural frequencies (*n*) given by a thin plate model of the specimen. The blue 3.2 μm square in (a) encloses the region that we model as a thin vibrating plate. The letters adjacent to each edge of the square indicate the boundary condition applied to each edge. F denotes a free boundary, and C denotes a clamped (also known as a fixed) boundary. A solid, blue circle is used to compare the orientation of the plate with the simulated images in

(C). In (a) we compare the natural frequencies of the FEM simulation to those observed via UEM. The blue curve is the FFT discussed in Figure 5.6(b), and the dotted red lines indicate the natural frequencies (*n*) given by the FEM simulation. Above each dotted line the mode number, *n*, for each natural frequency is given. In (c) there is a series of simulated images that illustrates the mode shape corresponding to each natural frequency.

The results shown here depict that there are certain transverse vibrational modes in HAMR TEM lamella upon laser illumination. We expect that if an actual device were operated at these resonant vibrational frequencies for a longer period of time, then there could be early failure, hence restricting their long-term use. The study shown here could be extended to other, similar interfaces and devices to determine their mechanical stability upon laser illumination.

5.3.2 Mass Density Mapping via Static TEM

Another study determining the density variation in gold NFT was carried out via static TEM imaging and spectroscopy capabilities. This was necessary to understand the outcome of the gold NFT synthesis process. In order to do that, three different signal scattered off the gold NFT were collected inside TEM using a HAADF detector, EEL spectrometer and an X-ray energy dispersive spectrometer. The high-angle incoherent electrons signal (HAADF-STEM) intensity is shown in Figure 5.8 which represent a relative density map in gold NFT, assuming that there is a uniform specimen thickness of NFT and there is only one element – gold – present. This is possible because contrast in

HAADF-STEM images arises from differences in *Z* of the elements comprising the specimen for sufficiently thin crystal sections [42], and if a uniform specimen thickness and elemental composition is assumed then the image intensity is a representation of mass density or packing of material.

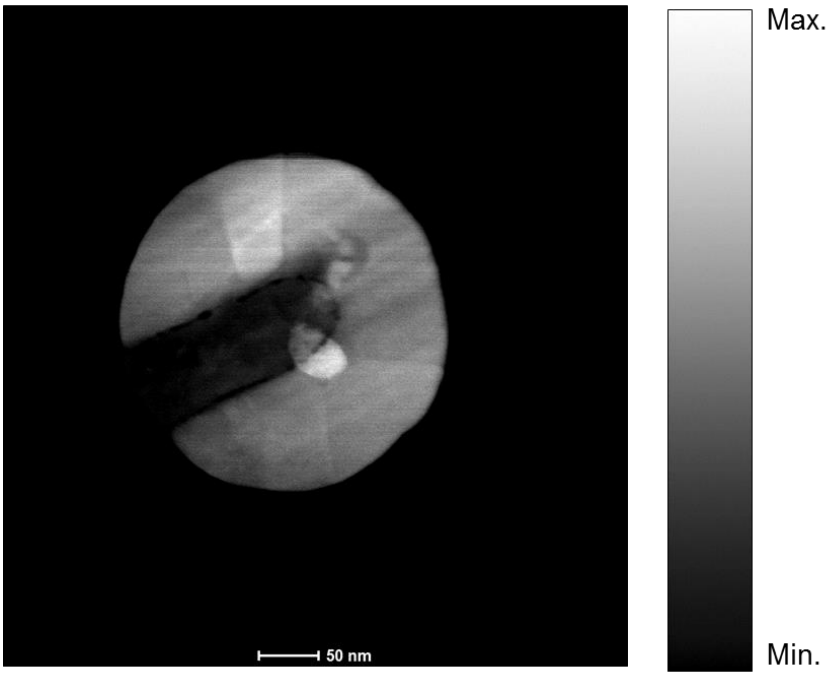

Figure 5.8 Contrast enhanced HAADF-STEM image showing the spatial distribution of HAADF-STEM intensity in gold NFT.

To quantify the relative mass density of material across gold bead, a line scan in the HAADF-STEM image was performed and the results are summarized in Figure 5.9. To support the results of HAADF-STEM imaging, a low-loss EEL spectra was also acquired across the gold NFT along the same line and the results are presented in Figure 5.10. It can be clearly from Figures 5.9(b) and 5.10(b) that both the high-angle

incoherently scattered electrons signal (HAADF-STEM) and low-angle inelastically scattered electron signal (EELS) show a similar trend. This confirms that the brighter regions in HAADF-STEM image have larger mass density, considering uniform specimen thickness of gold NFT.

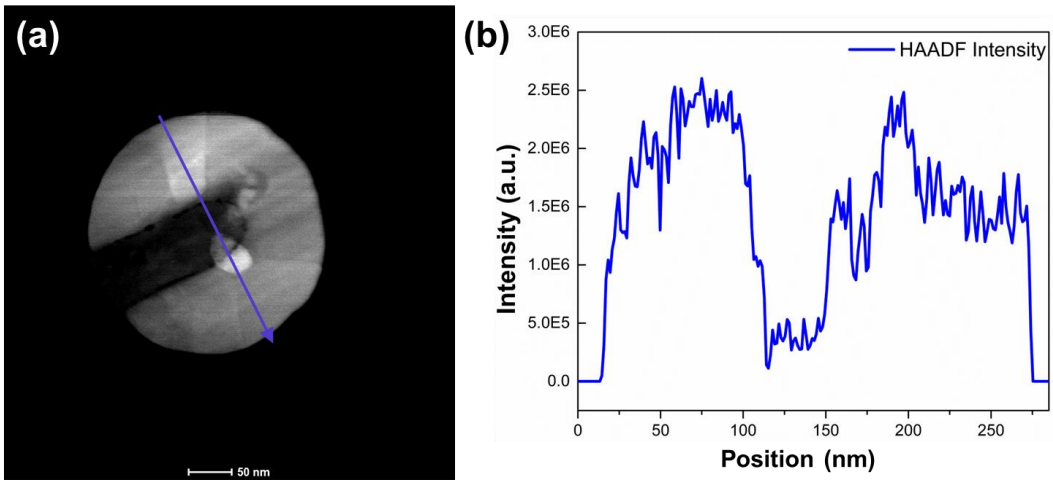

Figure 5.9 (a) Contrast enhanced HAADF-STEM image of gold NFT. The blue arrow shows the direction for HAADF-STEM intensity measurement. (b) A HAADF-STEM intensity line scan showing the spatial dependence of mass density across the gold NFT, as illustrated with the blue arrow in panel (a). Note that the position at 0 nm corresponds to the origin of the arrow.

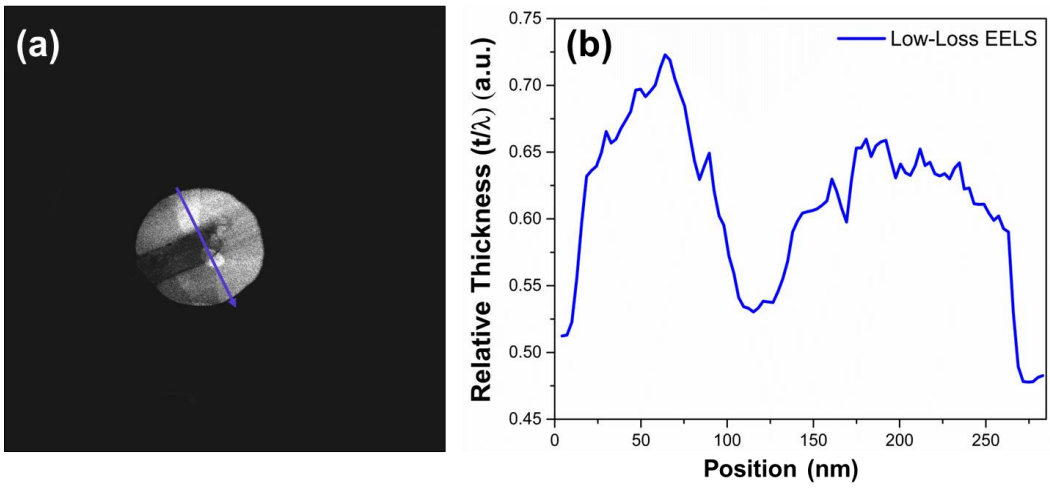

Figure 5.10 (a) Contrast enhanced HAADF-STEM image of gold NFT. The blue arrow shows the direction for low-loss EELS measurement. (b) A low-loss EELS line scan showing the relative thickness variation across the gold NFT, as illustrated with the blue arrow in panel (a). Note that the position at 0 nm corresponds to the origin of the arrow.

X-ray signals scattered off the gold NFT were also analyzed using XEDS and the results show a similar trend as that of HAADF-STEM intensity distribution (Figure 5.11) which again points that the brighter regions in HAADF-STEM image have larger mass density, considering uniform specimen thickness of gold NFT. Here, the assumption of uniform thickness of gold NFT seems to be reasonable because NFT dimensions are relatively very small (200-300 nm diameters). For other specimens having larger dimensions, this approach for density mapping should be used with a caution considering that a drastic variation in specimen thickness and elemental composition could happen.

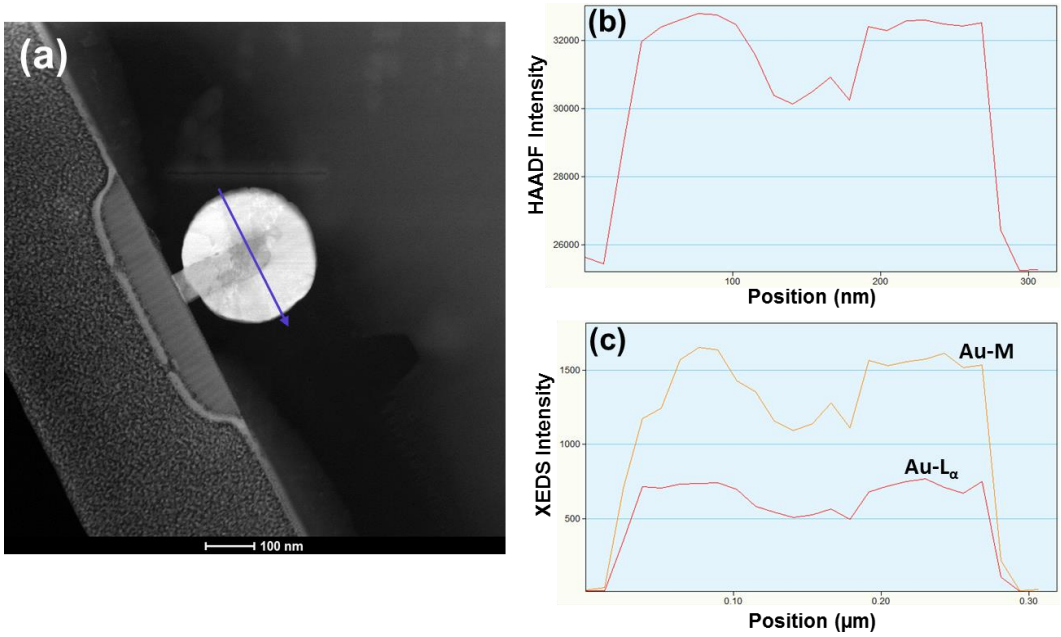

Figure 5.11 (a) HAADF-STEM image acquired at 15º alpha tilt in TEM holder. The blue arrow shows the direction for HAADF-STEM intensity and XEDS measurement. (b) A HAADF-STEM intensity line scan showing the spatial dependence of mass density across the gold NFT, as illustrated with the blue arrow in panel (a). Note that the position at 0 nm corresponds to the origin of the arrow. (c) An XEDS line scan showing the spatial dependence of gold M and L_α signal intensity across the NFT, as illustrated with the blue arrow in panel (a). Note that the position at 0 nm corresponds to the origin of the arrow.

5.4 Conclusion

In this study, we used UEM to observe nanomechanical vibrations within a metal-dielectric system. The metal-dielectric system of HAMR lamella consists of a 260-nm diameter gold disk embedded in a sapphire plate with a protective platinum layer on one

edge. We characterized the geometry and crystalline order of the specimen via TEM. A pulsed laser induced a mechanical response in the specimen. Using real-space, bright-field UEM images with 1 ns time steps, we observed oscillatory motion in the diffraction contrast surrounding the gold disk. Subsequently, we applied image analysis techniques to the ultrafast electron micrographs, revealing vibrational frequencies at 33.4, 63.9, 88.3, 114.5, and 119.6 MHz. An FEM simulation of the specimen identified the natural frequencies of mechanical vibration at 26.1, 62.9, 63.9, 88.8, and 113.8 MHz. The strong agreement between the simulated and observed frequencies indicates that the observed oscillations in the diffraction contrast surrounding the gold disk were direct manifestations of mechanical vibrations throughout the entire sapphire plate. In short, we utilized the high spatial-temporal resolution of UEM to observe ultrafast nanomechanical vibrations of a metal-dielectric system.

A quantitative and qualitative approach to map the density of gold NFT was demonstrated using HAADF-STEM, EELS and XEDS signals. From the present study, it is clear that any of the three signals could be used to get the density maps in gold NFT. For specimens with larger dimensions, non-uniform elemental composition and non-uniform specimen thickness, this approach should be used with a care.

5.5 Future Directions

Because the UEM at the University of Minnesota is routinely exciting acoustic phonons in diverse materials, it would be very interesting to look at the femtosecond phonon dynamics around gold NFT. For such studies, thinner specimens than the present

ones would be helpful since photoelectron intensity is lower in femtosecond imaging compared to nanosecond. Moreover, these thick specimens currently necessitate the use of a slow repetition rate of 2 kHz for maximum thermal and mechanical recovery before subsequent laser excitation, which results in poor signal-to-noise ratio when performing femtosecond imaging and hence not ideal. A systematic study to elucidate the laser fluences and repetition rates that do not damage the HAMR lamella upon laser excitation would be also useful for future UEM work and for actual operational devices. This could be helpful in understanding the crystallization behaviour of sapphire too.

It might be beneficial in future to know how diffusion of various elements in HAMR lamella happens upon laser heating. This is necessary to understand the temporal variation of elemental composition and could be studied via a combination of UEM with static TEM spectroscopy capabilities (STEM-EELS, STEM-XEDS) to map the elemental distribution before and after laser incidence. Another approach could be to perform *in situ* TEM heating experiments with a Gatan heating holder or a Protochips Aduro heating holder, combined with analytical techniques of STEM-EELS or STEM-XEDS for elemental mapping before and after heating.

Determination of thermal boundary conductance (TBC) [133] of the gold-sapphire interface via time-resolved convergent beam electron diffraction (CBED) experiments in UEM could reveal the thermal transport behaviour across the metal-dielectric interface in HAMR devices. In literature, UEM-CBED approach was demonstrated on silicon as thermometry [112] and could be used with HAMR lamella too, seeing the advantage of a nanometer sized probe in CBED for localized temperature

monitoring of gold NFT. This study was already initiated in the present work via a finite difference modelling simulation to see a temporal temperature variation in gold and sapphire upon laser heating in UEM. The simulation results are summarized in Figure 5.12, and show a temperature decay in gold bead and temperature rise in sapphire upon laser illumination, as a function of TBC. A laser fluence of 101.9 mJ/cm^2, incident laser wavelength of 1030 nm and an incident laser spot size of 50 µm were assumed in the simulations as UEM parameters, which are experimentally possible to achieve. The gold bead is the primary absorber at 1030 nm laser wavelength, so there is an initial temperature rise from 298 K to 387 K in gold instantaneously upon laser incidence. These simulations results, when fitted with UEM-CBED experimental results, could lead to determination of TBC and could open a new regime of thermal transport studies in HAMR devices.

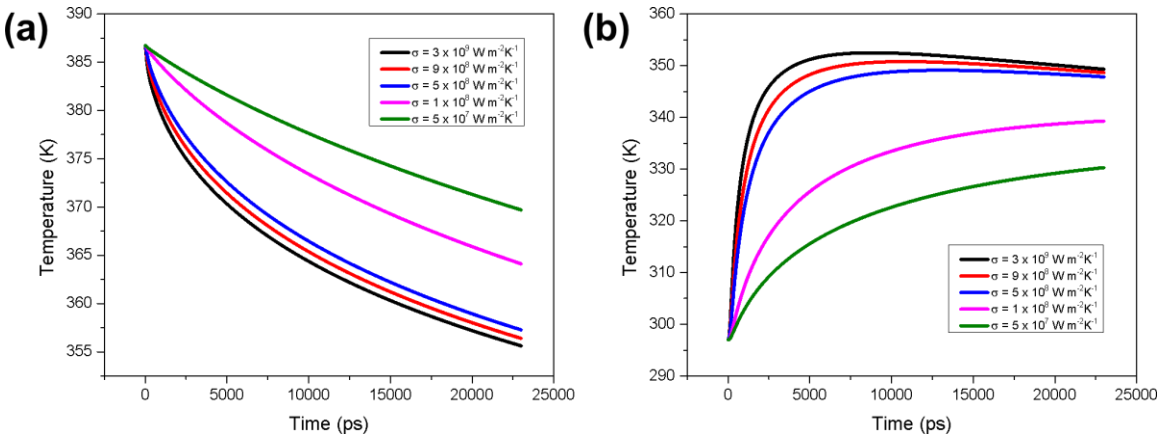

Figure 5.12 (a,b) Temporal variation of temperature decay and rise instantaneously after laser incidence in gold NFT and sapphire matrix, respectively, for various TBC values.

Chapter 6

Size-Dependent Plastic Response of Single-Crystal MgO Nanocubes

6.1 Introduction

It is known that beyond the brittle-ductile transition temperature (BDTT) brittle materials become ductile and can develop substantial plasticity. Therefore, developing ductile ceramics and semiconductors at room temperature has always been a challenging and active area of research [134-138]. Recent studies on Si [136] and GaAs [134] pillars have shown that the BDTT can be brought to room temperature by decreasing the size of the specimen, but the possibility of micro- and nano-scale ductile ceramics has been explored by few studies [139-144]. Reduction in size has been shown to enhance both the ductility as well as the yield strength [145, 146]. This behavior has been extensively studied using both *in situ* and *ex situ* scanning electron microscopy (SEM) and transmission electron microscopy (TEM) for various metals [147-150] and alloys [147, 151, 152]. These studies have been conducted at the micro- and nano-scale for different specimen geometries in compression and tension. With dimensional and microstructural constraints the change in mechanical behavior is often referred to as 'size effects' [145, 153]. Few semiconductor materials like Si spheres [154], Si and GaAs pillars [135, 136]

have also exhibited a size-dependent changes in yield strength and ductility. Several studies [147, 154-156] have offered explanations for this size-dependent mechanical behavior for metals, metallic alloys and semiconductors ranging from 50 nm to 50 μm.

Ceramics, unlike metals and semiconductors, being prone to cracking and fracture at room temperature are more difficult systems for plasticity studies, and hence micro- and nano- scale ceramics' geometries have not been explored extensively. Additionally, very limited conductivity of ceramics makes it almost impossible to utilize Focused Ion Beam (FIB) machining to prepare micro- and nano-scale specimens. In the present study we report the compression testing experiments on individual MgO cubes obtained by burning Mg and collecting smoke particles, thereby avoiding the difficulties and damage of FIB machining. This has enabled the size regime of 100-350 nm, not achieved previously. Additionally, the one-step synthesis of nano-scale MgO cubes with uniform cross-sectional area and aspect ratios of one enable homogenous deformation making them excellent candidates for size-dependent plasticity studies of ceramics at room temperature. Moreover, single crystal MgO does not show any phase transition up to 227 GPa [157], so it is easy to attribute any permanent deformation to dislocation plasticity. We extend the size range of experimental measurements of yield stress and ductility from those reported on compression testing of 250-5000 nm MgO pillars [140, 141] and bridge the gap to multiscale modeling with molecular dynamics (MD) simulations on sub-10 nm cubes [158, 159].

6.2 Methods

Commercially available Magnesium turnings (99.95% pure, Aldrich Chemical Co.) were burned using a propane gas flame in ambient air of a fume hood producing as-synthesized smoke particles. For TEM characterization the as-synthesized smoke particles were collected directly on a standard copper TEM grid with carbon supporting film. For SEM characterization, the as-synthesized smoke particles were collected directly on sapphire substrate coated with about 50 Å carbon to minimize specimen charging during imaging. Sapphire was chosen due to its significantly higher hardness and elastic modulus then MgO [160]. Individual MgO cubes for compression testing were obtained by ultra-sonication of the as-synthesized smoke particles placed in isopropanol (99.5% pure) for 90 minutes and then drop-casting on the carbon-coated sapphire substrates. Similarly the drop-casted solution, containing individual MgO cubes, was characterized in TEM. Compression tests were carried out using a Hysitron Triboindenter® in the displacement-controlled feedback mode.

6.3 Results and Discussion

Figure 6.1(a) shows a SEM micrograph of the as-synthesized smoke particles depicting agglomerated cubic-shaped MgO crystallites and also drop-casted individual MgO cube after ultra-sonication in isopropanol. A TEM diffraction pattern recorded from a MgO cube aligned along incident electron beam direction (Figure 1(b)) shows single crystallinity of cubes with {100} orientation. It has been shown that almost all MgO cubes obtained from smoke do not contain dislocations [161] and, therefore, for our

purposes can be considered dislocation-free. Extensive exposure to water and humidity from the air cause dissolution of MgO cubic crystals by developing first {110} truncations on the <110> edges and then {111} cuts at the corners without considerable hydroxylation [161-163]. For the MgO cubes studied here no detectable truncations and cuts were observed (see Figure 6.1).

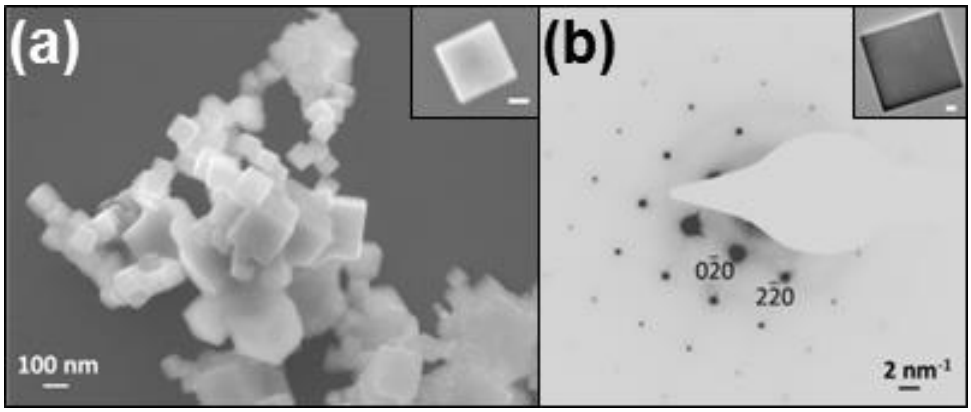

Figure 6.1 (a) A SEM image of as-synthesized MgO cubes collected from the smoke directly on carbon-coated sapphire. Inset shows a SEM image of individual MgO cube prepared by ultra-sonication of agglomerates in isopropanol for 90 min. (b) A TEM electron diffraction pattern and a bright-field image (inset) recorded from an individual MgO cube showing the single-crystallinity and {100} orientation of the cube. Insets in (a) and (b) have scale bar of 100 and 10 nm respectively.

Elemental compositions of cubes were also detected. Figures 6.2 and 6.3 summarize the results. Figure 6.2 shows a stark difference in the composition of cube and substrate, as expected. Cube comprises mainly of magnesium and oxygen, and the aluminum signal from the point and shoot XEDS acquisition on cube is expected to come

from the sapphire substrate beneath it. Carbon signal is due to the 50 Å coating on sapphire substrate, and a feeble silicon signal is coming from the Si(Li) detector.

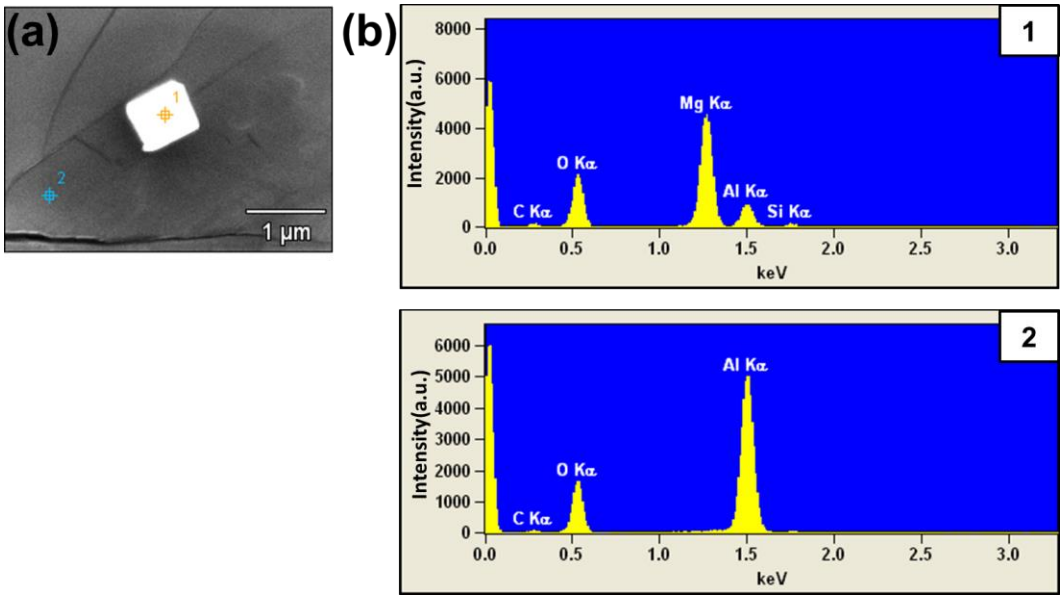

Figure 6.2 (a) A SEM image for the point and shoot XEDS acquisition from Spot 1 (on MgO cube) and Spot 2 (on sapphire substrate). (b) XEDS spectrum from Spot 1 (top) and Spot 2 (bottom) as marked in the panel (a).

Figure 6.3 shows an XEDS elemental mapping. It can be seen that the magnesium K_α signal is localized inside the cube and the aluminum K_α signal is outside of the cube. Oxygen and carbon are spread over the whole spectrum acquisition region. Overall, a nearly uniform elemental composition of MgO cube was confirmed and a quantitative analysis confirmed nearly 1:1 elemental ratio in MgO cubes. XEDS acquisitions in TEM were also performed which also suggested a uniform elemental

composition and 1:1 elemental ratio (the results are not shown in this document for brevity).

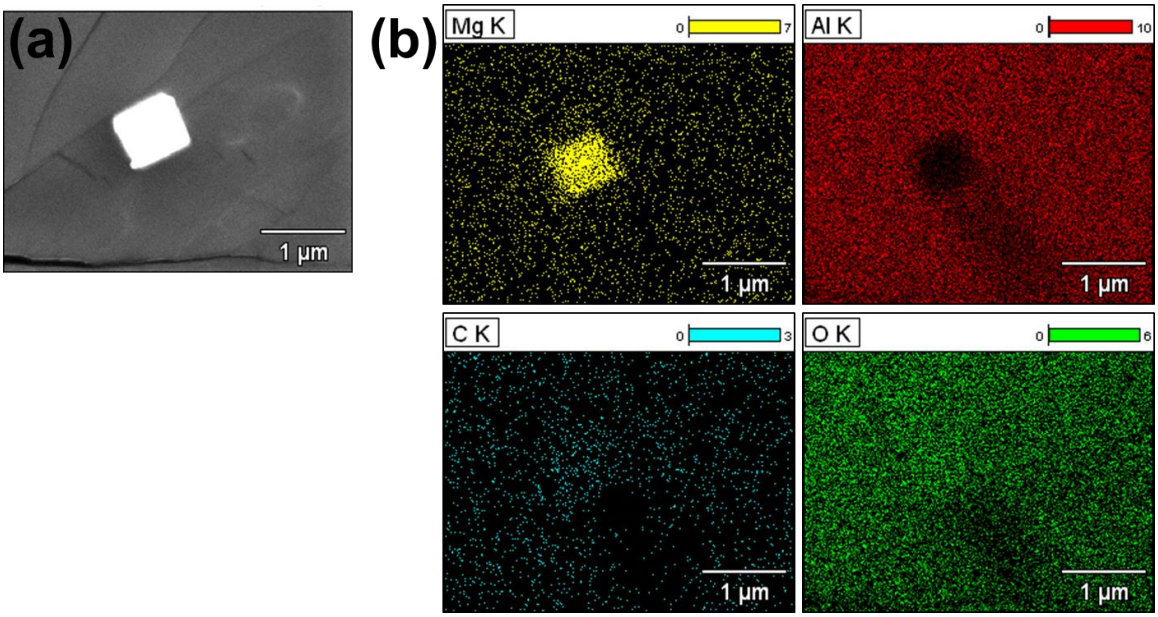

Figure 6.3 (a) A SEM image for the XEDS elemental mapping of a MgO cube located on sapphire substrate. (b) An XEDS elemental map in SEM for Mg (yellow), Al (red), C (blue) and O (green).

Figures 6.4-6.6 show typical load-displacement plot recorded from MgO cubes with associated SEM micrographs recorded before and after compression. In this study all MgO cubes were compressed using a cube corner diamond tip with R_{tip} = 190 nm radius of curvature. Constant nominal strain rates of 0.04 s^{-1} were used for all compression tests by adjusting the displacement and loading time. The yield stress, σ_Y, can be evaluated as:

$$\sigma_Y = \frac{F_Y}{\pi {a_{eff}}^2} \tag{1}$$

where F_Y is the load at the yield point and a_{eff} an effective in plane cube-indenter contact radius (see Figure 3) [164]:

$$a_{eff} = \sqrt{2\delta R_{eff} - \delta^2} \tag{2}$$

where δ is the displacement along the compression axis from the top of the cube and R_{eff} is effective radius of tip indenting cube of size d_0:

$$\frac{1}{R_{eff}} = \frac{2}{d_0} + \frac{1}{R_{tip}} \tag{3}$$

This approximation for evaluating yield stress is based on the fact that in these experiments the sizes of the indenting tip and cubes are of the same order, and after initial contact the radius of the tip changes to effective radius R_{eff}. Figure 6.7 shows a schematic describing the compression experiments and highlights the various experimental parameters used in the calculation of yield stress.

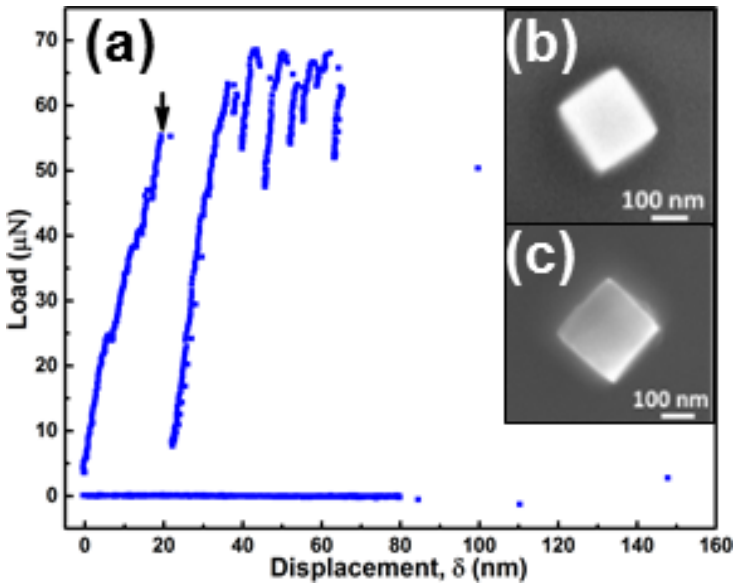

Figure 6.4 (a) Load-displacement plot obtained from a 206 nm MgO cube upon compression. Black arrow indicates the point on the curve that depicts yielding. SEM micrographs of the cube (b) before and (c) after compression. No fracture of the MgO cube was observed even at engineering strain ε_{eng} = 0.3.

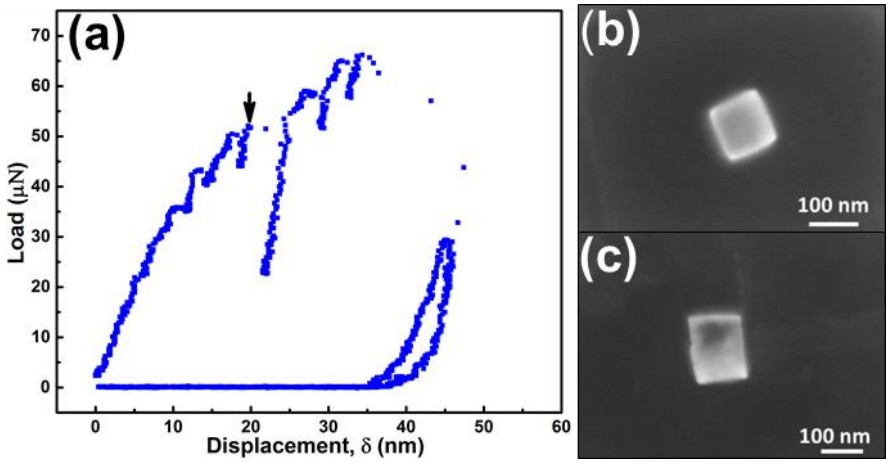

Figure 6.5 (a) Load-displacement plot obtained from a 111 nm MgO cube. Black arrow indicates the point on the curve that depicts yielding. SEM micrographs of the cube (b) before and (c) after compression. No fracture of the MgO cube was observed even at engineering strain ε_{eng} = 0.3.

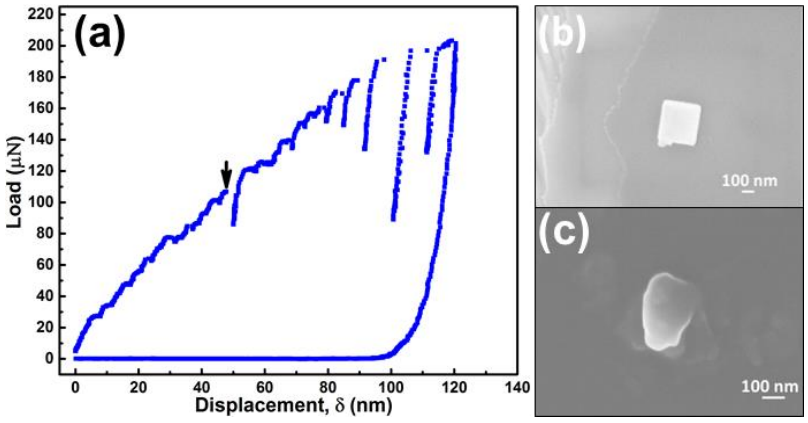

Figure 6.6 (a) Load-displacement plot obtained from a 331 nm MgO cube. Black arrow indicates the point on the curve that depicts yielding. SEM micrographs of the cube (b) before and (c) after compression. No fracture of the MgO cube was observed even at engineering strain ε_{eng} = 0.3.

Yield strength values from these experiments were deduced from the point of first major load drop in the load-displacement data, which is due to a dislocation avalanche under displacement-controlled experiments [145]. Multiscale modeling and atomistic MD simulations on single crystal nano-scale ideal MgO cubes confirms that yield strength indeed corresponds to first major load drop that is due to dislocation nucleation and propagation [158, 159]. It should be noted that small load drops occurring before load reaches yield strength point (see Figures 6.4-6.6) could be attributed to limited dislocation nucleation and propagation due to surface roughness of the cubes and indenter. It was also consistently seen in SEM after all the compression experiments that there was no fracture of the MgO cubes even up to engineering strain ε_{eng} = 0.3, which depicts a significant enhancement in the plasticity of MgO cubes from the pillars and bulk.

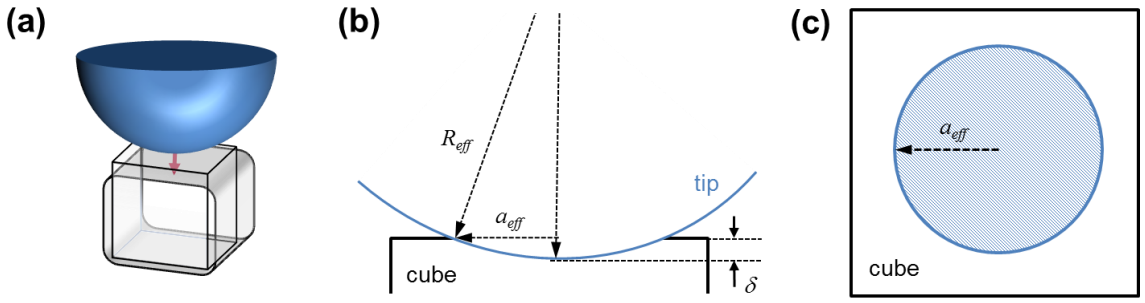

Figure 6.7 (a) Schematic representing the compression experiment and a deformation of cube upon loading. (b) An edge-on view of the indenter tip and a cube upon compression. (c) A top-view showing the circular contact area of indenter and cube.

The results of the compression experiments conducted on the cubes ranging from 100 to 350 nm are presented in Figure 6.8. As can be seen the yield stress has inverse power-law dependence on cube size. For comparison, yield strength values measured from single crystal {100}-oriented 0.5 to 5 μm [140] and 0.25 to 4.5 μm MgO pillars [141], and from bulk single crystals {100}-oriented MgO [165] are also shown. Here offset stresses at 0.2% strain was used to deduce yield strengths. The critical resolved shear stresses (CRSS), τ_c, for these cubes and pillars can be evaluated using corresponding Schmidt factors. Schmidt factors of the soft <110>{110} and hard <110>{100} slip systems in MgO for <001> applied compression are 0.5 and 0, respectively. The value of CRSS for the soft slip system is indicated in Figure 6.8(a). The dependence of engineering strains on the MgO cube size evaluated at yield point is shown in Figure 6.8(b).

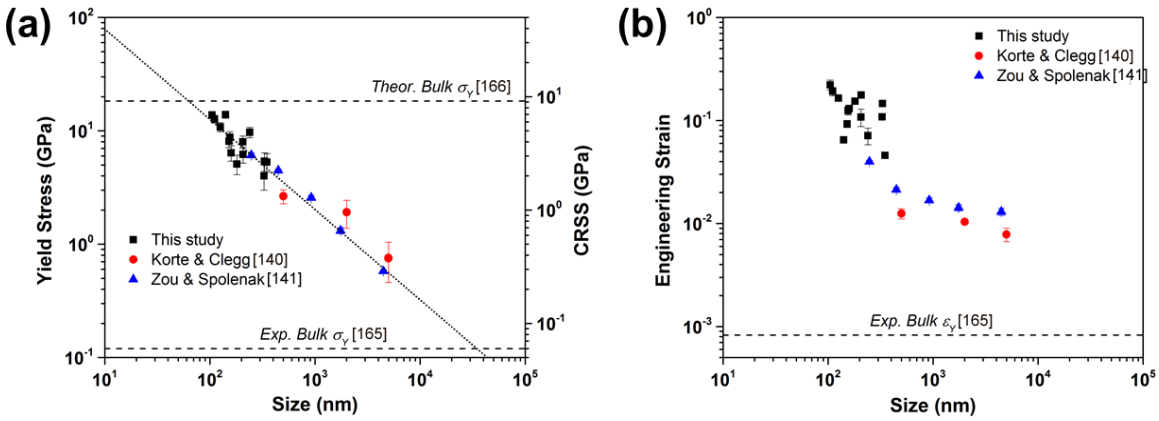

Figure 6.8 (a) Yield stress and CRSS for <110>{110} soft slip system as a function of MgO cube size. (b) Engineering strain at yielding as a function of cube size. For comparison, the results from Refs. [140] and [141] on MgO pillars are also indicated. The experimental values of the yield stress and engineering strain for bulk MgO [165] are indicated. Estimated theoretical yield stress for bulk MgO [166] is also plotted in panel (a).

The yield strength of bulk single-crystal MgO at room temperature when compressed along {100} orientation is 120 MPa and an engineering strain of 0.00076 at yielding leading to brittle failure at ε_{eng} = 0.075 [165]. Engineering strain up to 0.270 at brittle fracture has also been observed around 1200 °C in bulk {100}-oriented single crystals under compression [167]. The {100}-oriented 100-350 nm MgO cubes when compressed at room temperature exhibit yield stresses and engineering strains at yielding of 4.0 - 13.8 GPa and 0.046-0.154 respectively (Figure 6.8). They rarely show any brittle fracture at engineering strains up to 0.300 evaluated from load-displacement plots (see Figures 6.4-6.6 for an example). Reports by Korte and Clegg [140] and Zou and

Spolenak [141] on 250-5000 nm pillars also compressed along {100} indicate yield stresses of 0.6-6.1 GPa and engineering strains of 0.008-0.040, without brittle fracture for engineering strain up to ε_{eng} = 0.180. This increase of yield strength with decrease in MgO cube size can be attributed to a dislocation back stress, dislocation exhaustion, or creation of dislocation nucleation sources inside cubes also discussed by Nowak et al. [154]. The increase of engineering strain at yielding with decrease of MgO cube and pillars sizes indicates enhancement of crystal ductility with reduction of crystal size. Such size dependence of ductility at room temperature was also observed in Si [136] and GaAs [134] pillars and was explained by size dependent changes of the driving force for cracking [134]. Howie *et al.* [168] have suggested that cracking of Si and GaAs as well as in MgO, InAs, $MgAl_2O_4$ micro-pillars is due to through-thickness axial splitting which determines the brittle-to-ductile transitions.

The theoretical CRSS of a bulk single crystal MgO can be approximated as [166]:

$$\tau_c = G \frac{1}{6\pi} \frac{d_{110}}{d_{200}} \tag{4}$$

where G is the shear modulus, d_{200} and d_{110} are {200} and {100} interplanar spacings. For MgO <110>{100} slip system, G = 121.9 GPa [169], d_{200} = 2.106 Å and d_{110} = 2.978 Å [170] and it gives a theoretical CRSS of τ_c = 9.1 GPa. A Schmid factor of 0.5 gives theoretical bulk compressive yield strength of σ_Y = 18.3 GPa. As can be seen from Figure 6.8(a) simple extrapolation of a power-law size dependence of yield strength versus crystal size suggests that at about 60 nm single crystal MgO will potentially reach theoretical bulk yield strength. From Figure 6.8(a), it can also be noted that for 100-155 nm MgO cubes τ_t and CRSS lie in the expected theoretical shear strength range of G/30-

$G/2\pi$ (or 4.1-19.4 GPa) [171]. Xiong *et al.* [158] and Xiong and Chen [159] estimated the average compressive yield strength of 63.5 GPa for ~3×3×3 nm cube using multiscale modeling and atomistic MD simulations. Interestingly, their yield strength of 63.5 GPa was achieved near 0.110 engineering strain which is much more than 0.00076 for bulk MgO. Note that such simulations are not capable of producing brittle fracture. When experimental results were extrapolated to 63.5 GPa with power-law fit, an effective cube size of 11 nm is achieved. It should be noted that a large disparity in strain rates exists between the experiments reported here (0.04 s^{-1}) and the modeling and simulations referred above (~10^{10} s^{-1}). Even though extrapolated experimental results lay close to such simulations, it is premature to expect such few atoms represent the complexities of friction, multiple slip and image forces encountered experimentally. Additionally, in the absence of studies showing the strain-rate sensitivity of yield stress for nano-scale MgO, it should be expected that yield stress values are lower at a strain rate of 0.04 s^{-1} than the ~10^{10} s^{-1} used for the 3 nm cube simulation. Also noteworthy is that the size exponent of -0.74 (slope of linear fit in Figure 6.8(a)) for the size dependence of yield strength for MgO cubes and pillars (cf. Figure 6.8(a)) is similar to that of fcc metals [147]. The power-law fit, extrapolated to larger length scales, gives a cube size of 50 μm at the bulk yield strength. Such a transition to bulk properties has been observed for Ni [145, 172] and predicted for Ni alloy [145] microcrystals for diameters of 20 μm and larger.

Multiscale modeling and atomistic MD simulations predict surface dislocation nucleation and propagation along {110} slip planes to be the prominent plastic deformation mechanism for sub-10 nm defect free MgO cubes [158, 159] and we expect

the same for the MgO cubes in the 100-350 nm regime. TEM studies by Korte and Clegg [140] and SEM studies by Zou and Spolenak [141] also demonstrated that for compression of <100> MgO pillars, plastic deformation occurs along the <110>{110} soft slip system. However, a final caveat is that the MgO cube synthesis process may introduce unknown impurities. It was shown in literature that 40 mole parts per million (ppm) of Fe^{+3} impurities can increase the compressive yield stress in bulk {100}-oriented single crystal MgO by approximately 5 times [173]. Energy-dispersive X-ray spectroscopy (EDS) was attempted in TEM for impurities, but ppm level impurities cannot be detected. For better understanding of size effects in nano-scale single crystal MgO, effect of impurities should also be considered.

6.4 Conclusion and Future Directions

Compression testing of 100-350 nm {100}-oriented single crystal MgO cubes resulted in size-dependent yielding at stresses of 4-13.8 GPa and engineering strains of 0.046-0.154 without any significant brittle fracture at least up to 0.300 engineering strain. These values are significantly higher than the bulk compressive yield strength of 120 MPa and fracture strain of 0.075. A theoretical bulk compressive strength of 18.3 GPa is estimated and if extrapolated from the power-law relation, a cube size of nearly 60 nm for the theoretical bulk yield strength would be attained. While the power-law extrapolation of experimental results lay in the vicinity of multiscale modeling and atomistic MD simulations for sub-10 nm cubes, there are too many unknowns to ascribe significance. However, the general scheme of dislocation nucleation and growth is consistent. Surface

dislocation nucleation and motion through the complete crystal is expected to be the plastic deformation mechanism for the MgO cubes studied.

In future, performing *in situ* TEM compression experiments with Hysitron PI 95 Picoindenter in conjunction with molecular dynamics simulations on MgO and other ceramic nanoparticles could provide a clear picture of the atom origins of their deformation mechanisms [174-176]. This would be helpful in tailoring the microstructure of nano-scale ceramics for their future applications. The molecular dynamics simulations on MgO nanocubes are underway to understand the deformation mechanisms from the present study. Figure 6.9 shows a 6.5 nm MgO cube at various stages of a compression experiment in molecular dynamics simulations.

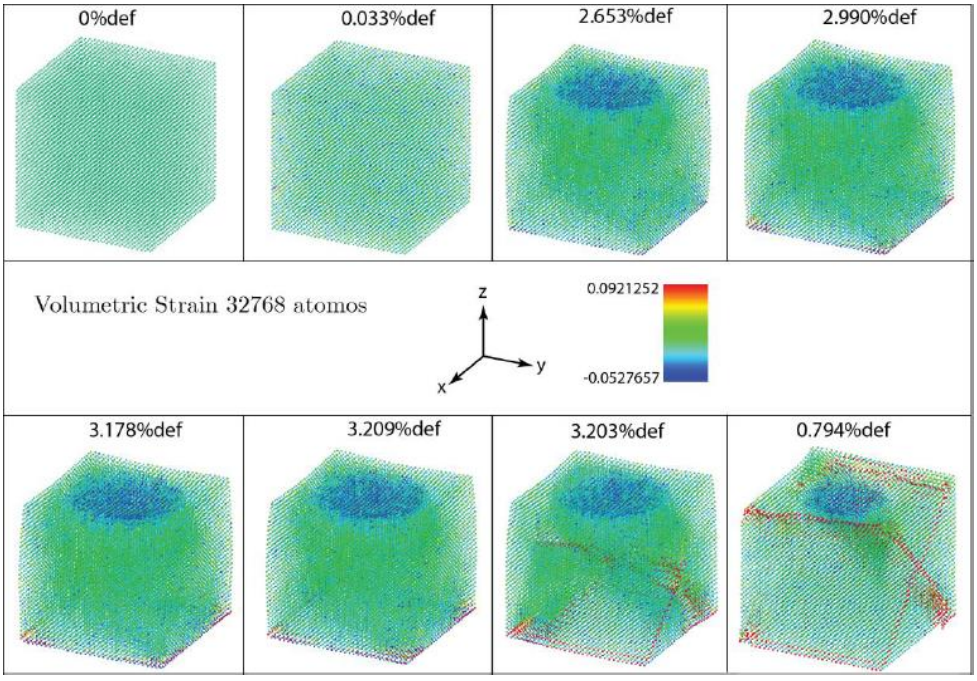

Figure 6.9 Snapshots of a 6.5 nm (or 32768 atoms) MgO cube at various deformation levels of a compression experiment in molecular dynamics simulations.

Chapter 7

Static Electron Microscopy Investigations of Fe-N-C Compounds

7.1 Introduction

The search for viable alternatives to non-renewable sources of energy (e.g., crude oil, coal, etc.) is a critical human endeavor that must succeed if we are to sustain quality of life without decimating the environment. In 2013 alone, the United States consumed 6.89 billion barrels of petroleum products or 18.88 million barrels per day [177]. The extraction of energy from carbon bonds in petroleum products is realized primarily by combustion, and this process produces greenhouse gases that are leading to rapid changes in the global environment. Further, extraction of these fossil fuels is becoming increasingly difficult, and the resulting geopolitical climate produces strained international relationships and – at worst – violent conflicts.

Sustained research efforts have generated several methods for reducing use of non-renewable energy sources [178]. For example, harvesting wind energy with large turbines and the use of electric vehicles (EVs) powered by efficient batteries are increasingly prevalent. While these technologies reduce overall fossil fuel use, they are currently quite costly due to reliance on motors and generators based on permanent

magnets (i.e., materials displaying persistent magnetism in the absence of an applied field) which can retain their properties at elevated working temperatures. Such magnets are often made from alloys of magnetic transition metals (Fe, Co, Ni) and rare earth elements (REEs) like neodymium (Nd), dysprosium (Dy), and samarium (Sm). The high costs of obtaining REEs limits the proliferation of technologies based on these materials [179].

The high costs of REEs stem from their geographic isolation as well as challenges associated with mining and processing. In 2010, approximately 97% of the world's REE supply came from production in China, and current processes for extraction and isolation rely on chemically-aggressive methods involving ammonia, sulfates, chlorides, and radioactive elements [180]. The current geopolitical climate, as well as an increasing need for permanent-magnet-based technologies for energy and defense, has prompted the U. S. Department of Energy (DOE) to call on researchers to identify, synthesize, and characterize sources of rare-earth-free permanent magnetic materials [181].

At the University of Minnesota, research is focused on developing low-cost permanent magnets comprised of earth-abundant elements such as iron (Fe) and nitrogen (N) that can be produced on large scales. An especially promising compound is $Fe_{16}N_2$, which has been shown to have magnetic properties comparable to REE-based magnets and can be synthesized as nanoparticles (diameters < 100 nanometers) and made into thin films (thicknesses < 500 nanometers) [182]. To date, however, high-purity $Fe_{16}N_2$ has not been produced on bulk scales (e.g., dimensions of centimeters). The challenge lies in developing synthetic protocols which allows N to be retained in the Fe crystal structure.

This in turn requires clear understanding of the crystal structure of the synthesized bulk iron nitride (FeN) compounds in order to confirm the presence and distribution of N. Recently, Prof. Jianping Wang's group in Electrical and Computer Engineering have developed synthetic methods for producing bulk quantities of FeN compounds, but precise understanding of their crystal structure and purity is needed. Moreover, the high-temperature stability of the FeN compounds, an important property for application in motors and generators, is not fully understood. The cutting edge electron microscopic capabilities at the University of Minnesota can be used to address these questions. In this chapter my research is therefore focused on using state-of-the-art electron microscopic capabilities to determine the crystal structures, purities, thermal stabilities, and structural and magnetic dynamics of these FeN compounds, and to understand how structure affects magnetic properties. This understanding is necessary to develop and refine synthetic methods for producing bulk quantities of high-purity $Fe_{16}N_2$ having magnetic properties that are at least comparable to commercially-available REE permanent magnets.

7.2 Methods

7.2.1 Image Simulations.

Simulations of atomic-resolution HAADF-STEM images were performed using a multislice computational method [88, 94]. Both aberration-corrected (nearly 0.5 Å probe size) and non-aberration-corrected (nearly 1.2 Å probe size) images at an accelerating voltage of 300 kV were simulated. Convergence angles of 25 mrad and 9 mrad were used for aberration-corrected and non-aberration-corrected image simulations,

respectively. $Cs_{(3)}$, $Cs_{(5)}$ and d_f were taken as zero, and only convergence angle was varied to control the STEM probe size on specimen. A detector collection angle of 54 to 340 mrad was used for all the HAADF-STEM image simulations. Atomic thermal vibrations at 300 K were simulated by averaging 10 frozen-phonon configurations for each image [95]. Root-mean-square (RMS) thermal displacement values of 0.112 and 0.060 Å at 300 K for N and Fe were used, respectively.

7.2.2 Specimen Preparation.

TEM specimens from ball-milled powders were prepared via ultrasonication in ethanol solution for 60 minutes followed by drop-casting onto holey carbon TEM grids made out of copper. TEM specimens from all the other bulk samples were made via an FEI Quanta 200 3D focused ion beam (FIB) operating at 30 kV of gallium ion beam. An OmniProbe® micromanipulator within the FIB chamber was used to lift-out the TEM lamella and attach them to OmniProbe® lift-out copper TEM grids with three posts.

7.2.3 Microscope Parameters.

An FEI Tecnai G2 F30 (FEG-TEM) operated at 300 kV (extraction voltage of 4,000 V), and equipped with Gatan Enfina EEL spectrometer and EDAX rTEM XEDS system having an ultrathin-window Si(Li) detector was used for conventional bright-field TEM imaging, HAADF-STEM imaging, EELS, XEDS and selected-area electron diffraction. Another FEI Technai G2 F30 (Cryo FEG-TEM) operated at 300 kV (extraction voltage of 4,000 V) and having a 4096 × 4096 ultrascan CCD camera was also used for conventional bright-field imaging and selected-area diffraction patterns. In this microscope, a Gatan 652 double-tilt heating holder was used for *in situ* thermal

experiments. In this model of heating holder temperature is measured via a type R thermocouple (platinum-13% rhodium vs. platinum).

7.3 Results and Discussion

7.3.1 Multislice Image Simulations.

The crystal structure of $Fe_{16}N_2$ has thus far only been hypothesized; there is no clear understanding where the nitrogen atoms sit in the unit-cell [183]. Therefore, the initial efforts in this work were directed towards developing methods and techniques to elucidate the interstitial position of nitrogen atoms in the $Fe_{16}N_2$ crystal structure. Figure 7.1 shows a body-centered tetragonal (BCT) crystal structure of $Fe_{16}N_2$ with a = 5.72 Å, c = 6.29 Å from the literature [183].

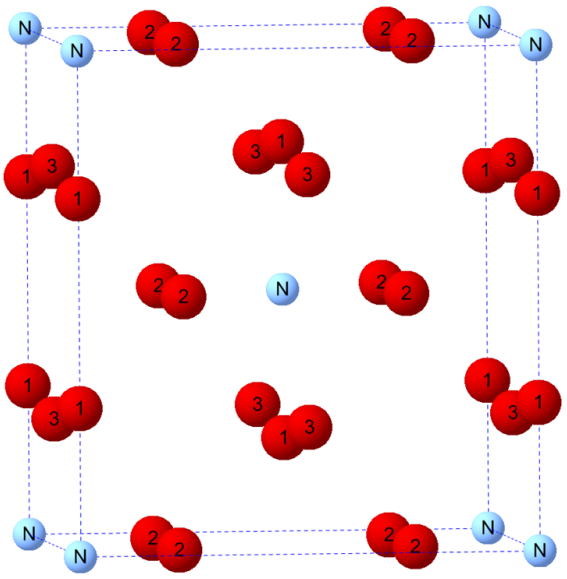

Figure 7.1 Crystal Structure of $Fe_{16}N_2$ (space group *I4/mmm*; No. 139). Nitrogen (light blue) and iron (red) atoms are visible. Indexing 1, 2, and 3 on iron (red) atoms depict the

three different types of locations of iron in the crystal structure. Unit-cell parameters are taken from ref [183].

As there is a significant difference in the atomic numbers of iron (*Z*: 26) and nitrogen (*Z*: 7), it was proposed that the *Z*-contrast of HAADF-STEM imaging could provide insights into the location of interstitial nitrogen atoms. To test this hypothesis, multislice simulations were performed. Figure 7.2 shows a qualitative *Z*-contrast between iron atomic-columns indexed 1 (center of image) and 2 in the cartoon at 0 K in both non-aberration-corrected and aberration-corrected images. This *Z*-contrast is because of the difference in the number of iron and nitrogen atoms along those columns (see Figure 7.1 for visualization). But this *Z*-contrast was not present in the simulated images at 300 K due an averaging of intensities upon thermal vibrations (Figure 7.3). Therefore, for the rest of the studies simulated images at 300 K were used to closely match the experimental conditions.

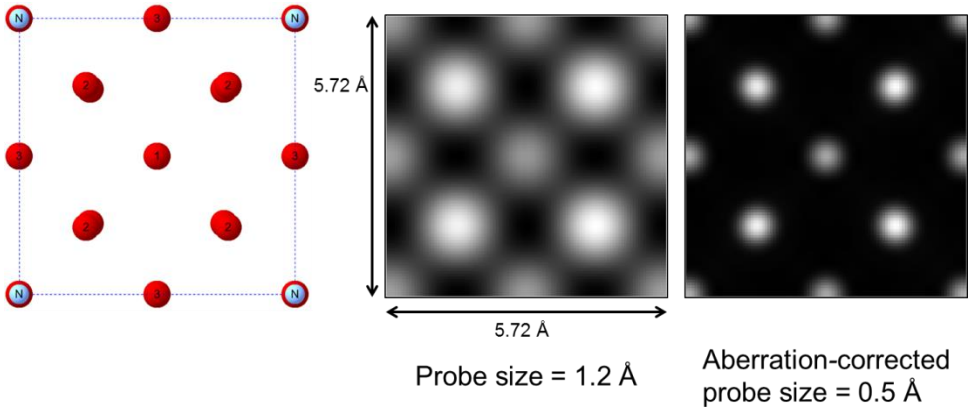

Figure 7.2 Crystal structure cartoon, a non-aberration-corrected HAADF-STEM image and an aberration corrected HAADF-STEM image of [001] oriented $Fe_{16}N_2$. Unit cell dimensions are marked in the non-aberration-corrected image which is also applicable for the cartoon and aberration-corrected image. Note that the simulated images do not include frozen-phonon configurations and hence are at 0 K. Atomic-column intensities are normalized to the incident beam intensity.

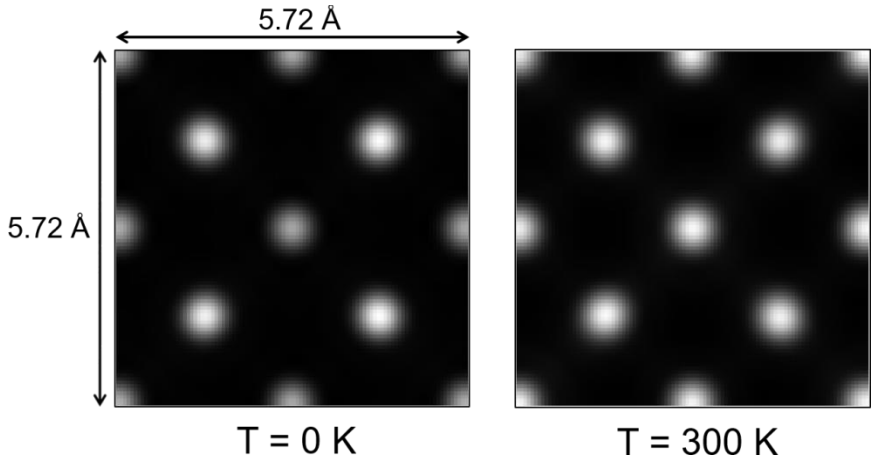

Figure 7.3 Aberration-corrected HAADF-STEM images of [001] oriented $Fe_{16}N_2$ at 0 K and 300 K. Unit cell dimensions are marked and are also applicable for the aberration-corrected image at 300 K. Atomic-column intensities are normalized to the incident beam intensity.

To de-convolute the iron and nitrogen atomic-column intensities in the HAADF-STEM images, multislice simulations were performed for [100] orientation having "pure" nitrogen columns (without any overlap of iron atoms). The results are summarized in Figures 7.4-7.6. Iron atomic-columns are clearly visible in Figure 7.4, but nitrogen

atomic-columns at the center and corner of unit-cell seem to be invisible to the naked eye. Therefore, intensity line-scans were performed in the images (Figures 7.5-7.6) to check for any evidence of the nitrogen signal.

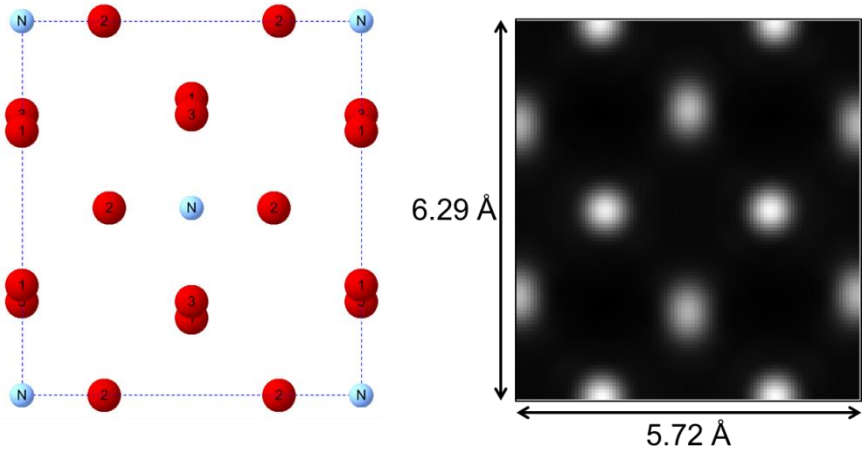

Figure 7.4 Crystal structure cartoon and an aberration corrected HAADF-STEM image of [100] oriented $Fe_{16}N_2$. Unit cell dimensions are marked in the aberration-corrected image which is also applicable for the cartoon. Note that the simulated image includes 10 frozen-phonon configurations at 300 K. Atomic-column intensities are normalized to the incident beam intensity.

From Figure 7.5 it could be seen that there are peaks in the intensity line-scan at the position of nitrogen atoms for a diagonal scan but not for a vertical scan. The presence of iron atoms along the vertical line-scan suppresses the feeble intensity peaks from nitrogen atoms as can be seen from the zoomed-view of the vertical intensity line-scan (Figure 7.5(c)). However, the absence of iron atoms along the diagonal line-scan allows visualization of intensity maxima at the nitrogen atom locations. This intensity

maxima hints that the nitrogen atoms are visible in the HAADF-STEM images. In order to confirm the visibility of "pure" nitrogen columns, control experiments were also performed. Figure 7.6 summarizes the results from a control experiment.

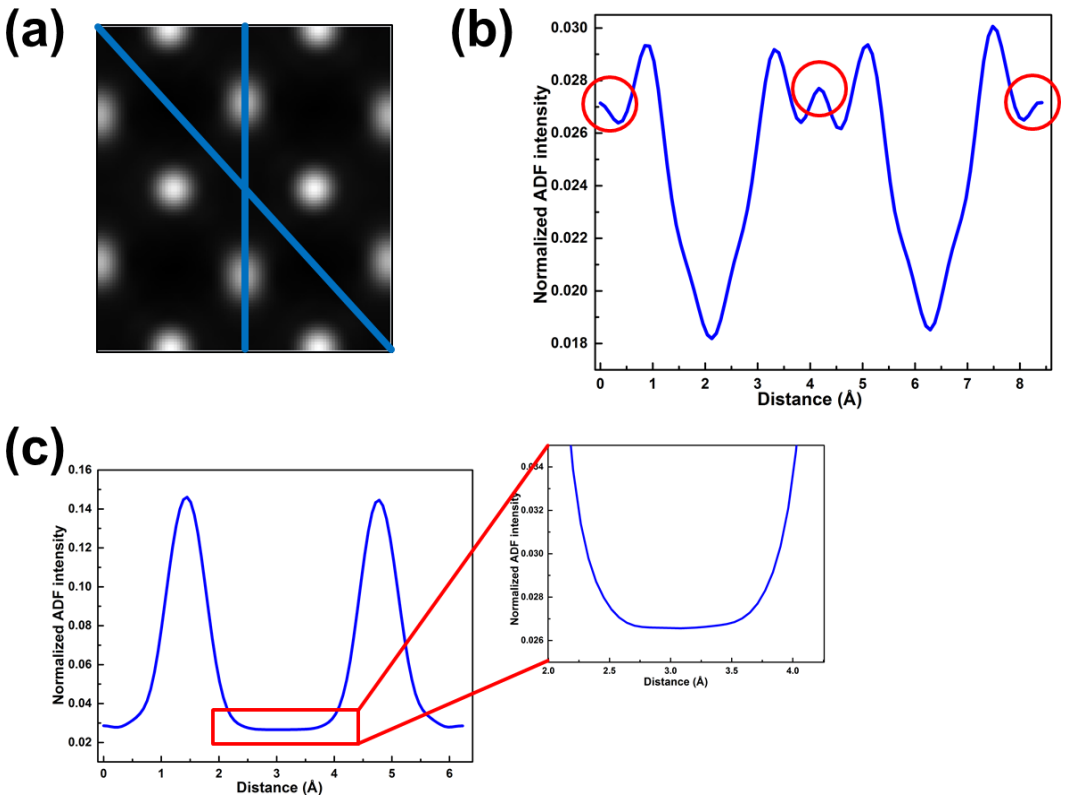

Figure 7.5 (a) A simulated aberration corrected HAADF-STEM image of [100] oriented $Fe_{16}N_2$ at 300 K. The diagonal and vertical blue lines represent the directions for 1-pixel and 4-pixels intensity integration in panels (b) and (c), respectively. Atomic-column intensities are normalized to the incident beam intensity. (b) HAADF-STEM intensity integrated for 1-pixel along the diagonal blue line in panel (a). The red circles highlight the peaks arising at the location of nitrogen atoms in the crystal structure. (c) HAADF-STEM intensity integrated for 4-pixels along the vertical blue line in panel (a). The red

rectangle highlights the region where nitrogen atom is present in the crystal structure and from where the zoomed-in intensity is shown.

Figure 7.6 represents a control for image simulation. HAADF-STEM Intensity scans were performed in the crystal structures of $Fe_{16}N_2$ with and without nitrogen. An absence of intensity maxima at the location of nitrogen atoms (Figure 7.6(c)) and their presence at the location of nitrogen atoms (Figure 7.6(b)) confirm that indeed nitrogen could be visible in the HAADF-STEM images if viewed along specific crystallographic orientations.

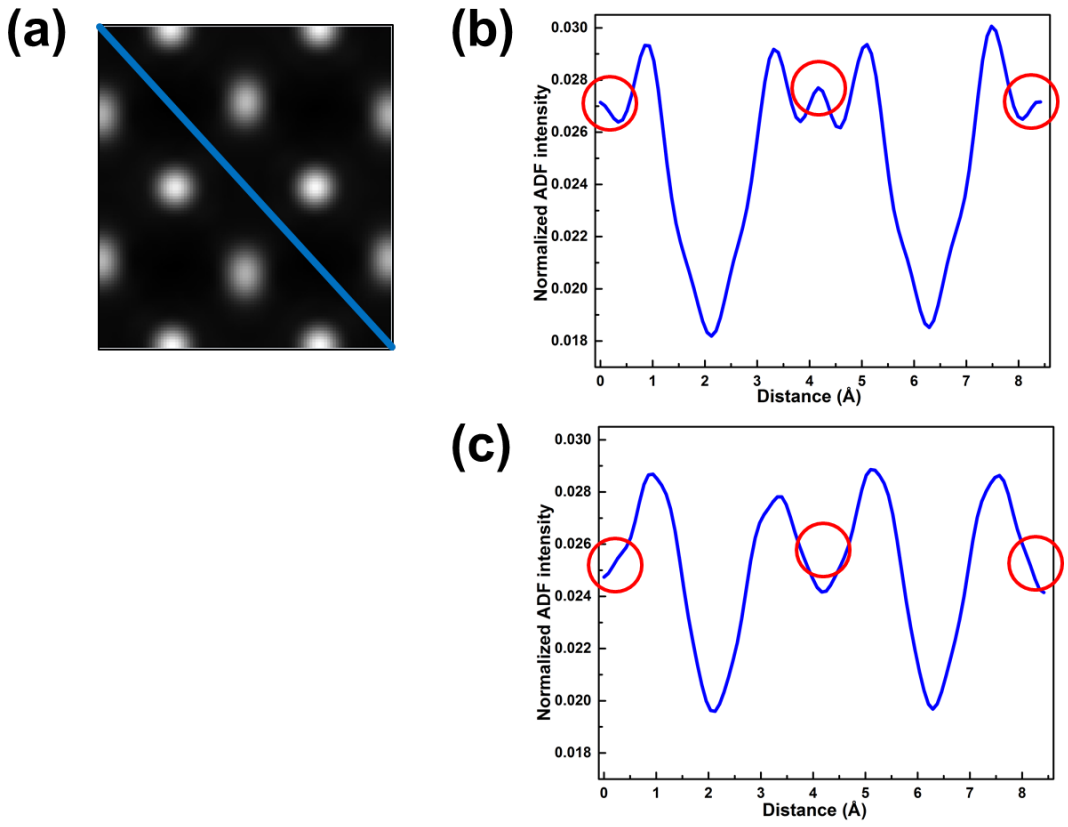

Figure 7.6 (a) A simulated aberration-corrected HAADF-STEM image of [100] oriented $Fe_{16}N_2$ at 300 K. The diagonal blue line represent the direction for 1-pixel integration in panels (b) and (c). Atomic-column intensities are normalized to the incident beam intensity. (b) HAADF-STEM intensity integrated for 1-pixel along the diagonal blue line in panel (a) when nitrogen atoms are present in the crystal structure. The red circles highlight the peaks arising at the location of nitrogen atoms in the crystal structure. (c) HAADF-STEM intensity integrated for 1-pixel along the diagonal blue line in panel (a) when nitrogen atoms are absent in the crystal structure. Note the absence of peaks at the red circles.

Based on the present simulation results, it is proposed that the presence of "pure" nitrogen atomic-columns along [101] and [111] crystal orientations could potentially allow the visibility of nitrogen in the experimental HAADF-STEM images of $Fe_{16}N_2$. This might require taking intensity line-scans in the directions without iron atoms in them. This would be helpful in elucidating the precise location of nitrogen atoms in the $Fe_{16}N_2$ crystal structure.

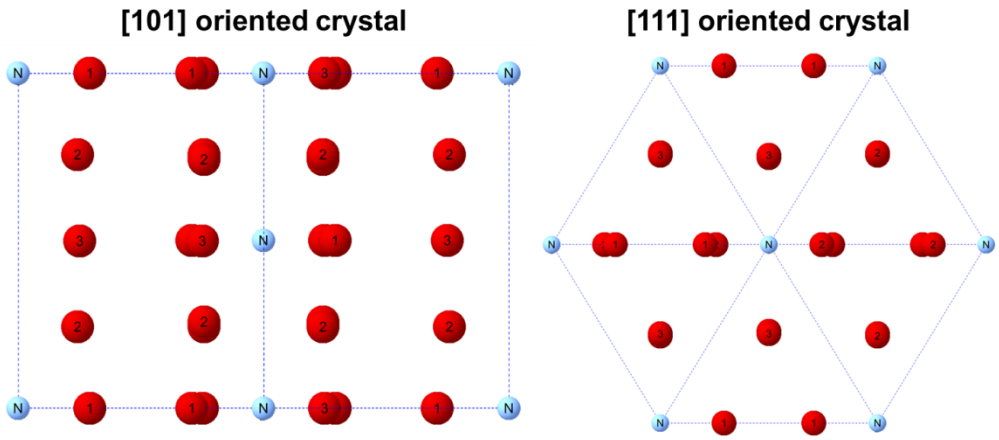

Figure 7.7 $Fe_{16}N_2$ crystal structure along [101] and [111] orientations depicting the presence of "pure" nitrogen atomic-columns.

The static TEM characterization results from hereon are on the specimens synthesized by various routes in the Prof. Jianping Wang's group. The aim is determine the crystal structures, purity levels and thermal stabilities of the synthesized FeN compounds. Dynamic TEM characterization on FeN compounds using UEM has not been systematically carried out yet.

7.3.2 Ball-Milled Specimens.

The synthesis protocol of ball-milled specimens is mentioned in detail elsewhere [184]. TEM characterization shows that the particles are agglomerated even after an ultrasonication of 60 mintues (Figure 7.8(a)) which hints that there is a significant welding of particles during ball-milling. The diffraction contrast in the powder particles denotes their crystalline nature. Kikuchi band and PBED pattern from a particle represent its single-crystallinity (Figures 7.8(b,c)) and shows a random crystal orientation

(Figure 7.8(c)). A higher-order Laue zone (HOLZ) could also be seen along with the Kikuchi band in Figure 7.8(b) which again confirms the single-crystalline nature of powder particles. These particles were found to be thick and randomly oriented for atomic-resolution imaging and diffraction.

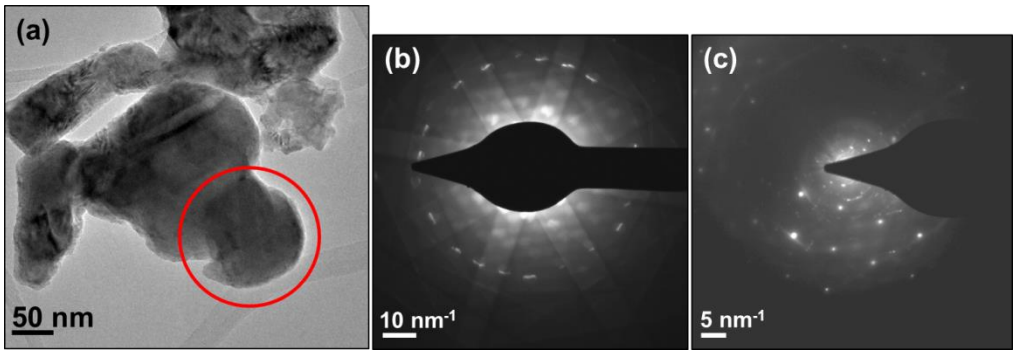

Figure 7.8 (a) A bright-field CTEM image of ball-milled specimens. Red circle denote the position of selected area aperture for the acquisition of Kikuchi band and PBED pattern in panels (b) and (c), respectively. (b) Kikuchi band from the powder particle highlighted with red circle in panel (a). (c) PBED pattern along a random crystal orientation of the powder particle highlighted with red circle in panel (a). Panel (a) is adapted from ref [184]. This sample received from Prof. Wang group had the identification number: FeN104.

Elemental composition of the ball-milled specimens was tested with XEDS. Figure 7.9 shows the presence of iron and nitrogen along carbon and oxygen which could be the impurities in the synthesis protocol. A significant presence of oxygen and carbon hints that the particles are getting oxidized and contain impurities, which could be

deleterious for their large-scale applications. A small nitrogen XEDS peak is potentially due its low fluorescence yield. Copper and silicon signals are coming from the copper TEM grid and an X-ray excitation of Si(Li) detector, respectively.

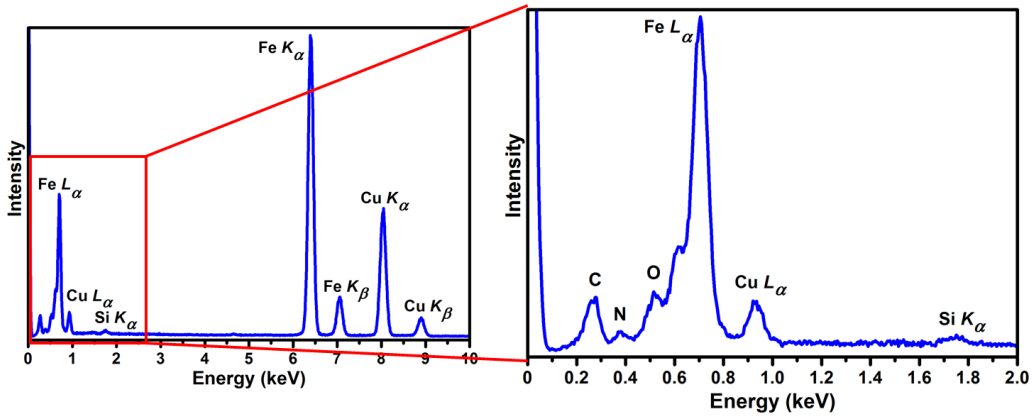

Figure 7.9 X-ray energy dispersive spectra (XEDS) acquired in CTEM mode from ball-milled specimens. This sample received from Prof. Wang group had the identification number: FeN104.

EELS, better for detecting low-*Z* elements than XEDS, was employed to detect the presence of various elements and to study the nano-scale distribution of iron and nitrogen in the ball-milled specimens. Figures 7.10 and 7.11 summarize the results. Iron and nitrogen were easily detected (Figure 7.10). Presence of oxygen signifies a possible oxidation of particles (Figure 7.10). EELS spectrum mapping in Figure 7.11 depicts a heterogeneous distribution of nitrogen and a nearly homogenous distribution of iron. These results show that it is difficult to keep nitrogen intact in the bulk specimens

uniformly and improvements are required in synthesizing the high-purity iron-nitride compounds.

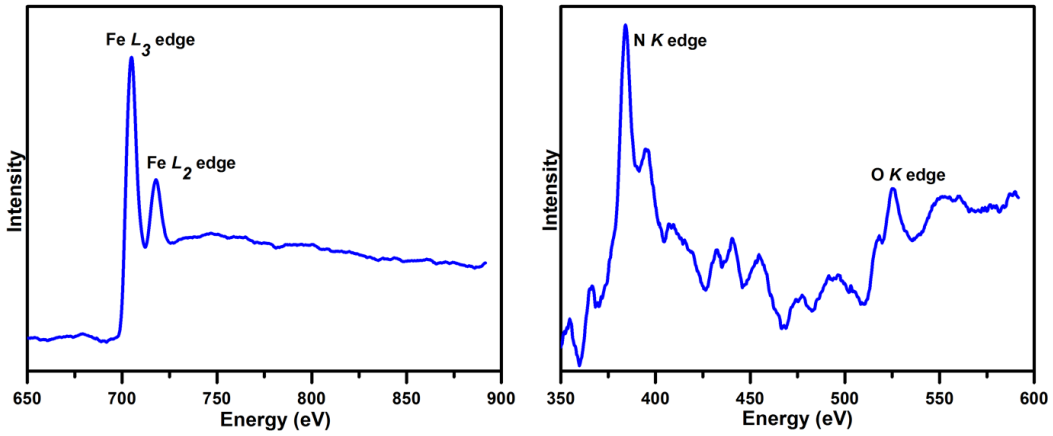

Figure 7.10 Electron energy-loss spectra (EELS) acquired in STEM mode from ball-milled specimens. Adapted from ref [184]. This sample received from Prof. Wang group had the identification number: FeN104.

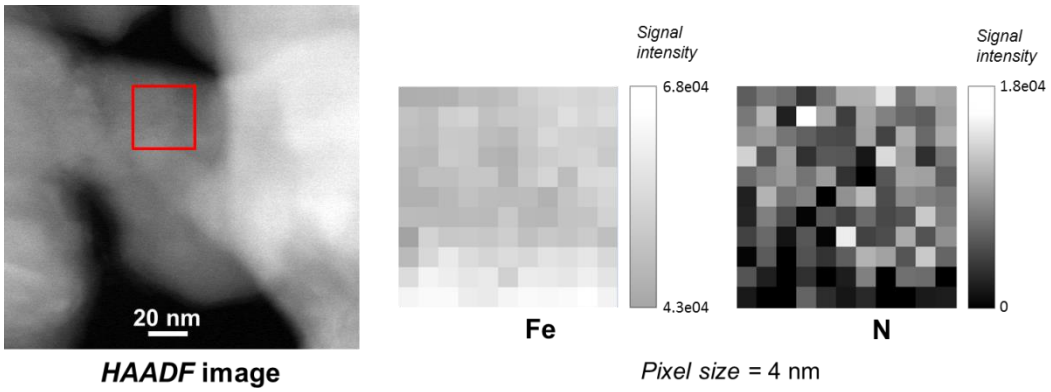

Figure 7.11 Elemental mapping of iron and nitrogen in ball-milled specimens with STEM-EELS. This sample received from Prof. Wang group had the identification number: FeN104.

7.3.3 Ball-Milled and Shock Compacted Specimens.

Alternate routes to synthesize bulk quantities of $Fe_{16}N_2$ having superior permanent magnetic properties than ball-milled powders were also employed in Prof. Wang group. Another such synthesis protocol was ball-milling followed by shock compaction of powders. The synthesis steps are mentioned in detail elsewhere [184]. In addition to determine crystal structure and purity, the synthesized samples were also tested for their thermal stability. Figure 7.12 shows the microstructure at two different temperatures and the grain boundaries could also be seen. Grains with sizes 80-200 nm were found at 23 ºC and no significant change in their size was observed with increasing temperature. We did not expect a change in grain size with temperature as the TEM specimens were kept only for 10 minutes at 275 ºC. Interestingly, a drastic change in the phases was observed upon heating as can be seen from the PBED patterns (Figure 7.13).

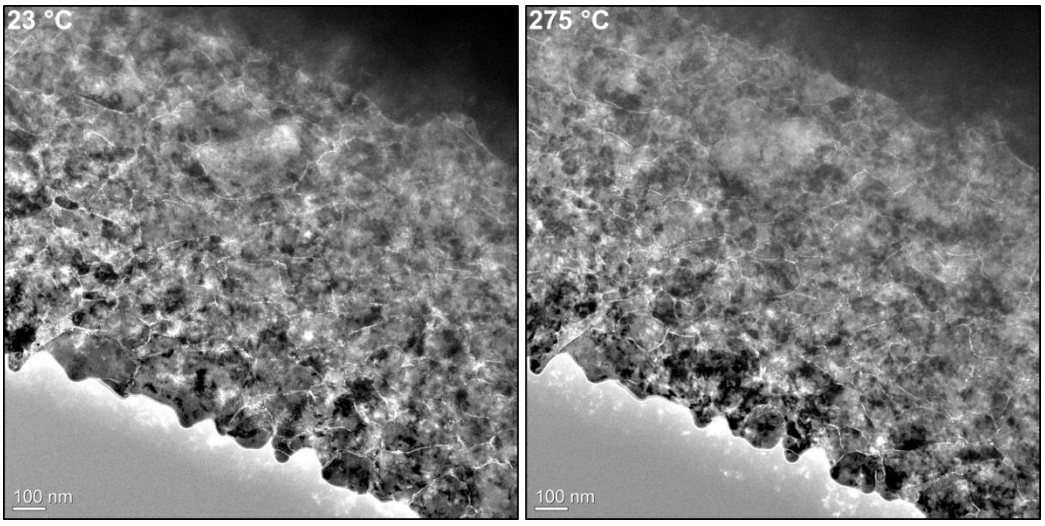

Figure 7.12 Microstructure of ball-milled and shock compacted specimens at 23 ºC (left) and 275 ºC (right). Adapted from ref [184]. This sample received from Prof. Wang group had the identification number: FeN120#3.

Figure 7.13 shows a decomposition of phases and hence a poor thermal stability of $Fe_{16}N_2$ phase in the ball-milled and shock compacted specimens. It has been observed in the literature [185, 186] and in the present study (Figure 7.13) that α´´- $Fe_{16}N_2$ decomposes into α-Fe and γ´- Fe_4N upon heating above 190 ºC. From Figure 7.13, it can be seen that the intensity of Fe, Fe_4N and iron oxide phases increase and of $Fe_{16}N_2$ decrease at 275 ºC, indicating a phase transformation Therefore, thermal stability of $Fe_{16}N_2$ phase is still a concern for their high-temperature applications and more work needs to be done for improvements.

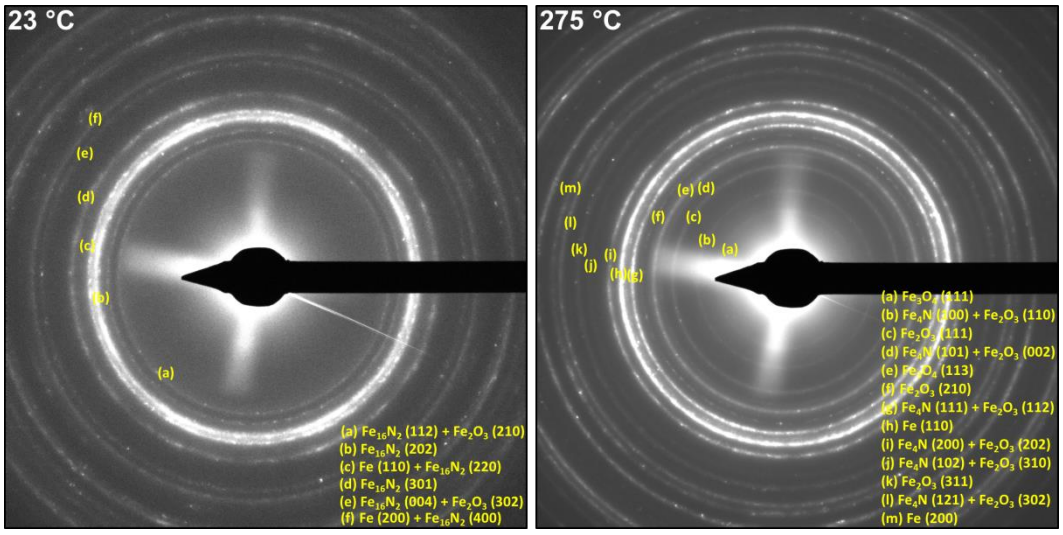

Figure 7.13 PBED patterns of ball-milled and shock compacted specimens at 23 ºC (left) and 275 ºC (right). Adapted from ref [184]. This sample received from Prof. Wang group had the identification number: FeN120#3.

7.3.4 Strained-Wire Specimens.

The strained-wire synthesis method to prepare rods is detailed in [187]. From TEM characterization, alternating grains of two different phases having 300-500 nm size were observed (Figure 7.14). One of the two phases was iron with [113] crystal orientation (Figure 7.14(center)) and the second phase with lattice spacing - 6.60 Å and 1.62 Å - was also found. Interestingly, these lattice-spacing values did not match with those of Fe, FeO, Fe_2O_3, Fe_3O_4, Fe_4N, Fe_3N, Fe_2N phases and were found to be very close to d_{001} and d_{123} of $Fe_{16}N_2$. This hints the presence of $Fe_{16}N_2$ grains. To support the structural analysis, it would be necessary to perform spectroscopic analysis (EELS, XEDS) in future for determining the elemental distribution.

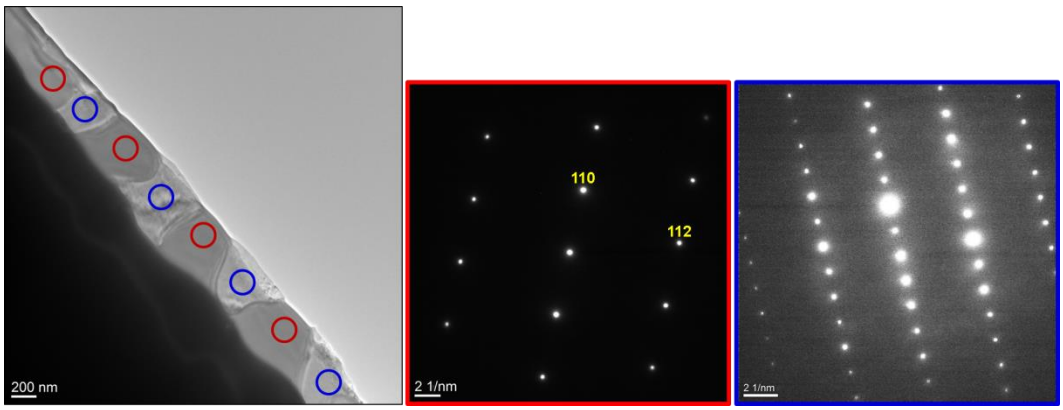

Figure 7.14 (Left) A bright-field CTEM image of a strained-wire specimen. Red and blue circles denote the location of selected area aperture in each grain for the acquisition

of PBED patterns. (Center) A representative PBED pattern from red circles marked in CTEM image. (Right) A representative PBED pattern from blue circles marked in CTEM image. This sample received from Prof. Wang group had the identification number: FeN48.

Figure 7.15 summarizes the high-resolution bright-field CTEM imaging results. The *d*-spacing values measured from both CTEM image and its FFT are same as measured from the PBED pattern in Figure 7.14(right). From both the diffraction and imaging results (Figures 7.14 and 7.15) it can be concluded that there are grains comprising different phases in them and hence there is a heterogeneous distribution of phases. In future, a spectroscopic analysis would be the next logical step to support the structural analysis results.

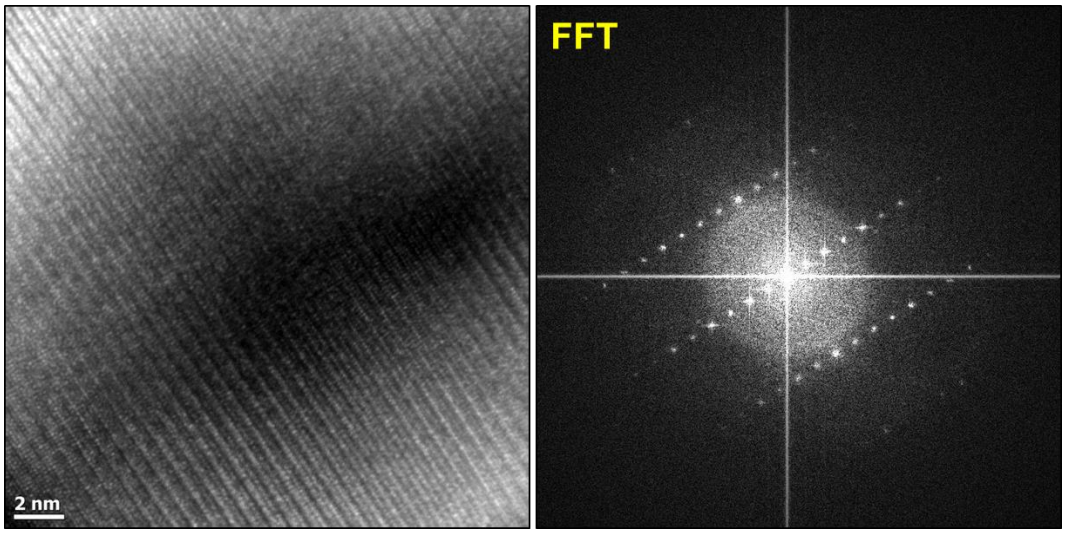

Figure 7.15 (Left) A high-resolution bright-field CTEM image from the grains highlighted with blue circles in Figure 7.14(left). (Right) FFT of the high-resolution

CTEM image. This sample received from Prof. Wang group had the identification number: FeN48.

7.3.5 Melt Spun Foil/Ribbon Specimens.

The synthesis protocol is summarized in [188]. A grain size of 2-10 μm was observed in these specimens (Figure 7.16(a)). In TEM characterization, individual grains were tested for their crystal structure determination and orientation with selected area apertures of different sizes (Figure 7.16(b)). It was observed from the PBED patterns that there are grains consisting of different phases and having multiple crystal orientations (Figure 7.16(bottom panel)). One of the phases was iron with [001] crystal orientation (Figure 7.16(bottom left)) and with [011] crystal orientation (Figure 7.16(bottom center)). Another phase with lattice spacing – 13.51 Å and 2.11 Å – was also found. Interestingly, these lattice-spacing values did not match with those of Fe, FeO, Fe_2O_3, Fe_3O_4, Fe_4N, Fe_3N, Fe_2N phases and were found to be very close to $2 \times d_{001}$ and d_{202} of $Fe_{16}N_2$. This hints the presence of $Fe_{16}N_2$ grains. To support the structural analysis, it would be necessary to perform spectroscopic analysis (EELS, XEDS) for determining the elemental distribution. However, these results show that the grains in melt spun foil/ribbon have a heterogeneous distribution of phases consisting of iron and possibly $Fe_{16}N_2$.

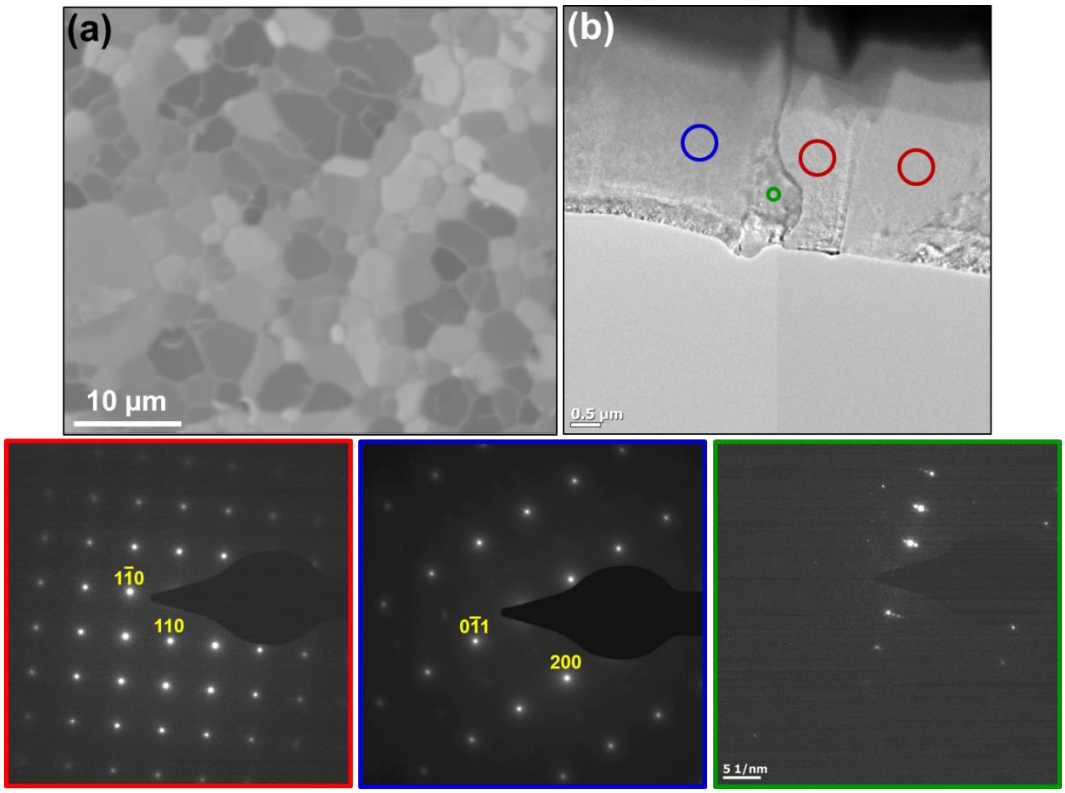

Figure 7.16 (a) A SEM image acquired with secondary electrons. (b) A bright-field CTEM image. Red, blue and green circles denote the selected area aperture location for the acquisition of PBED patterns in the bottom panel. (Bottom left) A representative PBED pattern from the red circles highlighted in panel (b). (Bottom center) A representative PBED pattern from the blue circle highlighted in panel (b). (Bottom right) A representative PBED pattern from the green circle highlighted in panel (b). This sample received from Prof. Wang group had the identification number: FeNM063a2.

7.3.5 Discovery of a New Phase - Minnedust.

During the synthesis of different types of iron-nitride specimen geometries ranging from ball-milled powders to melt spun foil/ribbon, a new phase (named

Minnedust) having very different magnetic properties (high saturation flux density, high relative permeability and low coercivity) than α″-$Fe_{16}N_2$ was discovered in Prof. Wang group. The synthesis protocol involves a cold crucible casting and is described in detail elsewhere [189]. This new phase Minnedust consists of iron, nitrogen and carbon. It is proposed that Minnedust could have one of the four possible elemental constitutions and structures: a mixture of α′-Fe_8N and α′-Fe_8C, a compound α′-$Fe_8(NC)$, a mixture of α″-$Fe_{16}N_2$ and α″-$Fe_{16}C_2$, or a compound α″-$Fe_{16}(NC)_2$ [189]. The proposed crystal structure (BCT) and *d*-spacing values of Minnedust are expected to be similar to that of α″-$Fe_{16}N_2$ [189]. But the magnetic properties of the synthesized specimens are significantly different than that of α″-$Fe_{16}N_2$ which suggests that this new phase of Minnedust is present. In the present work, static TEM characterization was performed on the synthesized specimens containing Minnedust which confirmed that it is currently difficult to conclusively elucidate the crystal structure of Minnedust. In this chapter, Minnedust is written as a mixture of α″-$Fe_{16}N_2$ and α″-$Fe_{16}C_2$. In a synthesized specimen containing Minnedust, various phases – pure iron, iron oxides, iron nitride and iron carbide – were observed (Figure 7.17). This shows that it is not possible yet to get pure Minnedust, and avoid the presence of iron oxides and pure iron in the synthesized specimens.

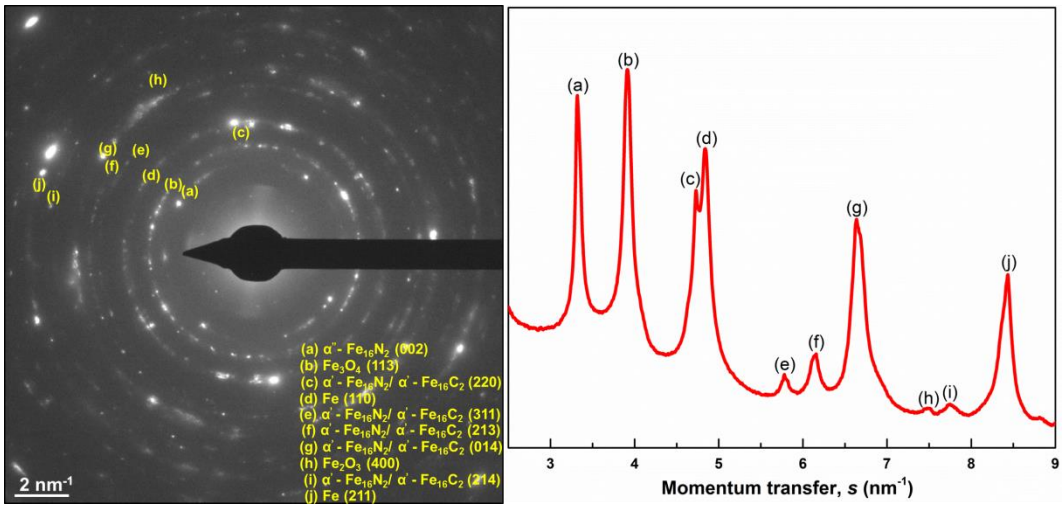

Figure 7.17 (Left) PBED pattern showing the various constituents in a synthesized specimen containing Minnedust. (Right) Radially integrated peak intensities from the PBED pattern. Note that the peaks of α″-$Fe_{16}N_2$ and α″-$Fe_{16}C_2$ are indistinguishable. Adapted from ref [189].

The high-resolution TEM image in Figure 7.18 shows a crystalline structure and the presence of multiple grains with different orientations in the synthesized specimens. From the inset, lattice spacing of (002) plane of BCT α″-$Fe_{16}N_2$ could be seen. From the magnetic property measurements and TEM characterization [189], it is concluded that there are additional phases in the synthesized specimens apart from α″-$Fe_{16}N_2$ which suggests a discovery of new phase – Minnedust.

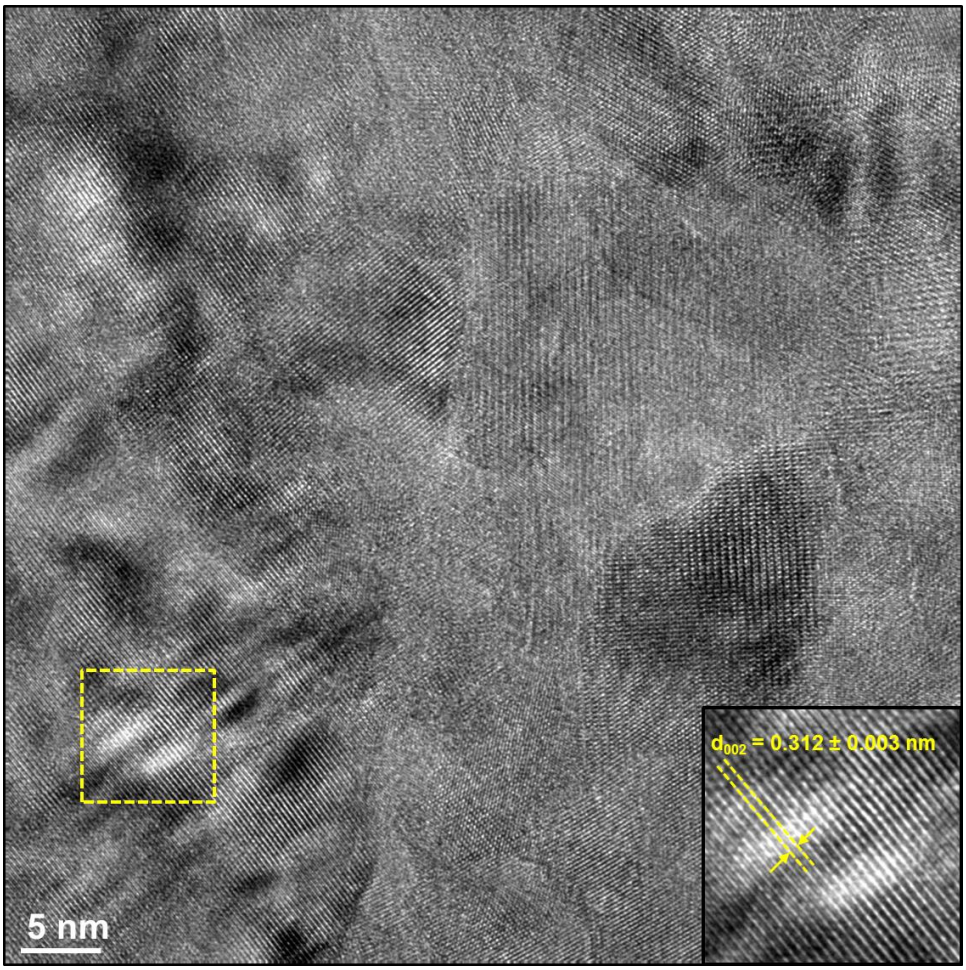

Figure 7.18 A high-resolution bright-field CTEM image of Minnedust specimen. Yellow dotted rectangle is the region for acquisition of inset. Inset shows d_{002} of α″-$Fe_{16}N_2$. Adapted from ref [189].

7.4 Conclusion and Future Directions

HAADF-STEM images of α″-$Fe_{16}N_2$ were simulated using a multislice code. Results show that it is possible to detect interstitial nitrogen and confirm the literature crystal structure of α″-$Fe_{16}N_2$ through atomic-resolution HAADF-STEM imaging experiments. To image the nitrogen it is necessary to integrate along specific

crystallographic orientations, including [100], [101], [111], having “pure” nitrogen columns in them. This is meaningful to de-convolute iron and nitrogen atomic-columns and to precisely observe the interstitial location of nitrogen to elucidate the crystal structure of α''-$Fe_{16}N_2$.

Various specimen geometries containing Fe-N-C phases were studied via static TEM. It was found that these methods were unable to produce pure α''-$Fe_{16}N_2$ and thepresence of iron and iron oxides hinder the synthesis. It was observed that the grain size depends on the synthesis protocol. There is a heterogeneous distribution of nitrogen and other phases. It was noticed that smaller grain size samples,i.e. ball-milled and ball-milled + shock compacted specimens, contained more α''-$Fe_{16}N_2$

In future, a combination of PBED, HR-TEM and spectroscopy from localized regions should be employed to determine crystal structures and purity levels, and to understand how structure affects magnetic properties. To study thermal stabilities, structural and magnetic dynamics of these FeN compounds, *in situ* TEM heating and UEM could be used [190]. All these characterization will give a comprehensive picture of the intrinsic structural, thermal and magnetic properties of synthesized FeN compounds.

References

[1] E. Ruska and T. Mulvey, *The Early Development of Electron Lenses and Electron Microscopy* (Hirzel Stuttgart, 1980).

[2] P. E. Batson, N. Dellby, and O. L. Krivanek, Sub-Ångstrom Resolution Using Aberration Corrected Electron Optics, *Nature* **418**, 617 (2002).

[3] P. D. Nellist, M. F. Chisholm, N. Dellby, O. L. Krivanek, M. F. Murfitt, Z. S. Szilagyi, A. R. Lupini, A. Borisevich, W. H. Sides, Jr., and S. J. Pennycook, Direct Sub-Angstrom Imaging of a Crystal Lattice, *Science* **305**, 1741 (2004).

[4] J. C. H. Spence and J. M. Zuo, *Electron Microdiffraction* (Plenum Press, New York, 1992).

[5] R. Erni, M. D. Rossell, C. Kisielowski, and U. Dahmen, Atomic-Resolution Imaging with a Sub-50-pm Electron Probe, *Phys. Rev. Lett.* **102**, 096101 (2009).

[6] J. C. H. Spence, *High-Resolution Electron Microscopy* (Oxford University Press, New York, NY, USA, 2013).

[7] D. B. Williams and C. B. Carter, *Transmission Electron Microscopy: A Textbook for Materials Science* (Springer, New York, 2009).

[8] B. Fultz and J. Howe, *Transmission Electron Microscopy and Diffractometry of Materials* (Springer, New York, 2013).

[9] F. Banhart, Ed., *In-Situ Electron Microscopy at High Resolution* (World Scientific, Singapore, 2008).

[10] G. Dehm, J. M. Howe, and J. Zweck, Eds., *In-Situ Electron Microscopy: Applications in Physics, Chemistry, and Materials Science* (Wiley, Weinheim, 2012).

[11] H. Zheng, Y. S. Meng, and Y. Zhu, Frontiers of *In Situ* Electron Microscopy, *MRS Bull.* **40**, 12 (2015).

[12] N. de Jonge and F. M. Ross, Electron Microscopy of Specimens in Liquid, *Nat. Nanotechnol.* **6**, 695 (2011).

[13] J. M. Yuk, J. Park, P. Ercius, K. Kim, D. J. Hellebusch, M. F. Crommie, J. Y. Lee, A. Zettl, and A. P. Alivisatos, High-Resolution EM of Colloidal Nanocrystal Growth Using Graphene Liquid Cells, *Science* **336**, 61 (2012).

[14] H.-G. Liao, D. Zherebetskyy, H. Xin, C. Czarnik, P. Ercius, H. Elmlund, M. Pan, L.-W. Wang, and H. Zheng, Facet Development During Platinum Nanocube Growth, *Science* **345**, 916 (2014).

[15] C.-M. Wang, H.-G. Liao, and F. M. Ross, Observation of Materials Processes in Liquids by Electron Microscopy, *MRS Bull.* **40**, 46 (2015).

[16] P. L. Gai, Developments in *In Situ* Environmental Cell High-Resolution Electron Microscopy and Applications to Catalysis, *Top. Catal.* **21**, 161 (2002).

[17] H. Yoshida, Y. Kuwauchi, J. R. Jinschek, K. J. Sun, S. Tanaka, M. Kohyama, S. Shimada, M. Haruta, and S. Takeda, Visualizing Gas Molecules Interacting with Supported Nanoparticulate Catalysts at Reaction Conditions, *Science* **335**, 317 (2012).

[18] H. L. Xin, S. Alayoglu, R. Tao, A. Genc, C.-M. Wang, L. Kovarik, E. A. Stach, L.-W. Wang, M. Salmeron, G. A. Somorjai, and H. Zheng, Revealing the Atomic Restructuring of Pt-Co Nanoparticles, *Nano Lett.* **14**, 3203 (2014).

[19] P. A. Crozier and T. W. Hansen, *In Situ* and *Operando* Transmission Electron Microscopy of Catalytic Materials, *MRS Bull.* **40**, 38 (2015).

[20] J. X. Zhang, B. Xiang, Q. He, J. Seidel, R. J. Zeches, P. Yu, S. Y. Yang, C. H. Wang, Y. H. Chu, L. W. Martin, A. M. Minor, and R. Ramesh, Large Field-Induced Strains in a Lead-Free Piezoelectric Material, *Nat. Nanotechnol.* **6**, 97 (2011).

[21] M. J. Hÿtch and A. M. Minor, Observing and Measuring Strain in Nanostructures and Devices with Transmission Electron Microscopy, *MRS Bull.* **39**, 138 (2014).

[22] J. F. Pulecio, P. Warnicke, S. D. Pollard, D. A. Arena, and Y. Zhu, Coherence and Modality of Driven Interlayer-Coupled Magnetic Vortices, *Nat. Commun.* **5**, 3760 (2014).

[23] G. McMullan, S. Chen, R. Henderson, and A. R. Faruqi, Detective Quantum Efficiency of Electron Area Detectors in Electron Microscopy, *Ultramicroscopy* **109**, 1126 (2009).

[24] M. Battaglia, D. Contarato, P. Denes, D. Doering, T. Duden, B. Krieger, P. Giubilato, D. Gnani, and V. Radmilovic, Characterisation of a CMOS Active Pixel Sensor for Use in the TEAM Microscope, *Nucl. Instrum. Methods Phys. Res., Sect. A* **622**, 669 (2010).

[25] G. McMullan, A. R. Faruqi, D. Clare, and R. Henderson, Comparison of Optimal Performance at 300 keV of Three Direct Electron Detectors for Use in Low Dose Electron Microscopy, *Ultramicroscopy* **147**, 156 (2014).

[26] V. A. Lobastov, R. Srinivasan, and A. H. Zewail, Four-Dimensional Ultrafast Electron Microscopy, *Proc. Natl. Acad. Sci. U. S. A.* **102**, 7069 (2005).

[27] W. E. King, G. H. Campbell, A. Frank, B. Reed, J. F. Schmerge, B. J. Siwick, B. C. Stuart, and P. M. Weber, Ultrafast Electron Microscopy in Materials Science, Biology, and Chemistry, *J. Appl. Phys.* **97**, 111101 (2005).

[28] T. LaGrange, M. R. Armstrong, K. Boyden, C. G. Brown, G. H. Campbell, J. D. Colvin, W. J. DeHope, A. M. Frank, D. J. Gibson, F. V. Hartemann, J. S. Kim, W. E. King, B. J. Pyke, B. W. Reed, M. D. Shirk, R. M. Shuttlesworth, B. C. Stuart, B. R. Torralva, and N. D. Browning, Single-Shot Dynamic Transmission Electron Microscopy, *Appl. Phys. Lett.* **89**, 044105 (2006).

[29] H. S. Park, J. S. Baskin, O.-H. Kwon, and A. H. Zewail, Atomic-Scale Imaging in Real and Energy Space Developed in Ultrafast Electron Microscopy, *Nano Lett.* **7**, 2545 (2007).

[30] M. R. Armstrong, K. Boyden, N. D. Browning, G. H. Campbell, J. D. Colvin, W. J. DeHope, A. M. Frank, D. J. Gibson, F. Hartemann, J. S. Kim, W. E. King, T. B. LaGrange, B. J. Pyke, B. W. Reed, R. M. Shuttlesworth, B. C. Stuart, and B. R. Torralva, Practical Considerations for High Spatial and Temporal Resolution Dynamic Transmission Electron Microscopy, *Ultramicroscopy* **107**, 356 (2007).

[31] A. H. Zewail, Four-Dimensional Electron Microscopy, *Science* **328**, 187 (2010).

[32] A. H. Zewail and J. M. Thomas, *4D Electron Microscopy: Imaging in Space and Time* (Imperial College Press, London, 2010).

[33] A. H. Zewail, Micrographia of the Twenty-First Century: From Camera Obscura to 4D Microscopy, *Philos. Trans. R. Soc. London, Ser. A* **368**, 1191 (2010).

[34] D. J. Flannigan and A. H. Zewail, 4D Electron Microscopy: Principles and Applications, *Acc. Chem. Res.* **45**, 1828 (2012).

[35] N. D. Browning, M. A. Bonds, G. H. Campbell, J. E. Evans, T. LaGrange, K. L. Jungjohann, D. J. Masiel, J. McKeown, S. Mehraeen, B. W. Reed, and M. Santala, Recent Developments in Dynamic Transmission Electron Microscopy, *Curr. Opin. Solid State Mater. Sci.* **16**, 23 (2012).

[36] T. LaGrange, B. W. Reed, M. K. Santala, J. T. McKeown, A. Kulovits, J. M. K. Wiezorek, L. Nikolova, F. Rosei, B. J. Siwick, and G. H. Campbell, Approaches for Ultrafast Imaging of Transient Materials Processes in the Transmission Electron Microscope, *Micron* **43**, 1108 (2012).

[37] D. J. Flannigan and O. Lourie, 4D Ultrafast Electron Microscopy Sheds Light on Dynamic Processes from the Micrometer to the Atomic Scale, *Microsc. Anal.* **27**, S5 (2013).

[38] L. Piazza, D. J. Masiel, T. LaGrange, B. W. Reed, B. Barwick, and F. Carbone, Design and Implementation of a fs-Resolved Transmission Electron Microscope Based on Thermionic Gun Technology, *Chem. Phys.* **423**, 79 (2013).

[39] J. S. Baskin and A. H. Zewail, Seeing in 4D with Electrons: Development of Ultrafast Electron Microscopy at Caltech, *C. R. Phys.* **15**, 176 (2014).

[40] T. LaGrange, B. W. Reed, and D. J. Masiel, Movie-Mode Dynamic Electron Microscopy, *MRS Bull.* **40**, 22 (2015).

[41] L. Reimer and H. Kohl, *Transmission Electron Microscopy: Physics of Image Formation* (Springer Science & Business Media, New York, NY, USA, 2008).

[42] S. J. Pennycook and P. D. Nellist, *Scanning Transmission Electron Microscopy: Imaging and Analysis* (Springer, New York, 2011).

[43] A. C. Fischer-Cripps, *Nanoindentation* (Springer New York, 2011).

[44] F. L. Deepak, A. Mayoral, and R. Arenal, Eds., *Advanced Transmission Electron Microscopy* (Springer International Publishing Switzerland, 2015).

[45] D. A. Muller, Structure and Bonding at the Atomic Scale by Scanning Transmission Electron Microscopy, *Nat. Mater.* **8**, 263 (2009).

[46] D. A. Plemmons, P. K. Suri, and D. J. Flannigan, Probing Structural and Electronic Dynamics with Ultrafast Electron Microscopy, *Chem. Mater.* **27**, 3178 (2015).

[47] R. J. D. Miller, Femtosecond Crystallography with Ultrabright Electrons and X-Rays: Capturing Chemistry in Action, *Science* **343**, 1108 (2014).

[48] E. Kieft, K. B. Schliep, P. K. Suri, and D. J. Flannigan, Communication: Effects of Thermionic-Gun Parameters on Operating Modes in Ultrafast Electron Microscopy, *Struct. Dyn.* **2**, 051101 (2015).

[49] P. Voyles, J. Grazul, and D. Muller, Imaging Individual Atoms inside Crystals with ADF-STEM, *Ultramicroscopy* **96**, 251 (2003).

[50] W. C. Oliver and G. M. Pharr, Measurement of Hardness and Elastic Modulus by Instrumented Indentation: Advances in Understanding and Refinements to Methodology, *J. Mater. Res.* **19**, 3 (2004).

[51] W. C. Oliver and G. M. Pharr, An Improved Technique for Determining Hardness and Elastic-Modulus Using Load and Displacement Sensing Indentation Experiments, *J. Mater. Res.* **7**, 1564 (1992).

[52] G. Haugstad, *Atomic Force Microscopy Understanding Basic Modes and Advanced Applications* (John Wiley & Sons,, Hoboken, N.J., 2012).

[53] Y. Kamihara, T. Watanabe, M. Hirano, and H. Hosono, Iron-Based Layered Superconductor $La[O_{1-x}F_x]FeAs$ (x = 0.05-0.12) with T_c = 26 K, *J. Am. Chem. Soc.* **130**, 3296 (2008).

[54] Z.-A. Ren, G.-C. Che, X.-L. Dong, J. Yang, W. Lu, W. Yi, X.-L. Shen, Z.-C. Li, L.-L. Sun, F. Zhou, and Z.-X. Zhao, Superconductivity and Phase Diagram in Iron-Based Arsenic-Oxides $ReFeAsO_{1-\delta}$ (Re = Rare-Earth Metal) without Fluorine Doping, *EPL* **83**, 17002 (2008).

[55] J. Paglione and R. L. Greene, High-Temperature Superconductivity in Iron-Based Materials, *Nat. Phys.* **6**, 645 (2010).

[56] P. J. Hirschfeld, M. M. Korshunov, and I. I. Mazin, Gap Symmetry and Structure of Fe-Based Superconductors, *Rep. Prog. Phys.* **74**, 124508 (2011).

[57] A. Chubukov, Pairing Mechanism in Fe-Based Superconductors, *Annu. Rev. Condens. Matter Phys.* **3**, 57 (2012).

[58] K. Ishida, Y. Nakai, and H. Hosono, To What Extent Iron-Pnictide New Superconductors Have Been Clarified: A Progress Report, *J. Phys. Soc. Jpn.* **78**, 062001 (2009).

[59] P. C. Canfield and S. L. Bud'ko, Feas-Based Superconductivity: A Case Study of the Effects of Transition Metal Doping on $BaFe_2As_2$, *Annu. Rev. Condens. Matter Phys.* **1**, 27 (2010).

[60] D. C. Johnston, The Puzzle of High Temperature Superconductivity in Layered Iron Pnictides and Chalcogenides, *Adv. Phys.* **59**, 803 (2010).

[61] H.-H. Wen and S. Li, Materials and Novel Superconductivity in Iron Pnictide Superconductors, *Annu. Rev. Condens. Matter Phys.* **2**, 121 (2011).

[62] C. de la Cruz, Q. Huang, J. W. Lynn, J. Li, W. Ratcliff II, J. L. Zarestky, H. A. Mook, G. F. Chen, J. L. Luo, N. L. Wang, and P. Dai, Magnetic Order Close to Superconductivity in the Iron-Based Layered $LaO_{1-x}F_xFeAs$ Systems, *Nature* **453**, 899 (2008).

[63] T. Nomura, S. W. Kim, Y. Kamihara, M. Hirano, P. V. Sushko, K. Kato, M. Takata, A. L. Shluger, and H. Hosono, Crystallographic Phase Transition and

High-T_c Superconductivity in LaFeAsO:F, *Supercond. Sci. Technol.* **21**, 125028 (2008).

[64] M. A. McGuire, A. D. Christianson, A. S. Sefat, B. C. Sales, M. D. Lumsden, R. Jin, E. A. Payzant, D. Mandrus, Y. Luan, V. Keppens, V. Varadarajan, J. W. Brill, R. P. Hermann, M. T. Sougrati, F. Grandjean, and G. J. Long, Phase Transitions in LaFeAsO: Structural, Magnetic, Elastic, and Transport Properties, Heat Capacity and Mössbauer Spectra, *Phys. Rev. B* **78**, 094517 (2008).

[65] J. H. Chu, J. G. Analytis, K. De Greve, P. L. McMahon, Z. Islam, Y. Yamamoto, and I. R. Fisher, In-Plane Resistivity Anisotropy in an Underdoped Iron Arsenide Superconductor, *Science* **329**, 824 (2010).

[66] T. M. Chuang, M. P. Allan, J. Lee, Y. Xie, N. Ni, S. L. Bud'ko, G. S. Boebinger, P. C. Canfield, and J. C. Davis, Nematic Electronic Structure in the "Parent" State of the Iron-Based Superconductor $Ca(Fe_{1-x}Co_x)_2As_2$, *Science* **327**, 181 (2010).

[67] S. Kasahara, H. J. Shi, K. Hashimoto, S. Tonegawa, Y. Mizukami, T. Shibauchi, K. Sugimoto, T. Fukuda, T. Terashima, A. H. Nevidomskyy, and Y. Matsuda, Electronic Nematicity above the Structural and Superconducting Transition in $BaFe_2(As_{1-x}P_x)_2$, *Nature* **486**, 382 (2012).

[68] J.-H. Chu, H.-H. Kuo, J. G. Analytis, and I. R. Fisher, Divergent Nematic Susceptibility in an Iron Arsenide Superconductor, *Science* **337**, 710 (2012).

[69] S. A. Kivelson, E. Fradkin, and V. J. Emery, Electronic Liquid-Crystal Phases of a Doped Mott Insulator, *Nature* **393**, 550 (1998).

[70] R. M. Fernandes, A. V. Chubukov, and J. Schmalian, What Drives Nematic Order in Iron-Based Superconductors?, *Nat. Phys.* **10**, 97 (2014).

[71] R. M. Fernandes, L. H. VanBebber, S. Bhattacharya, P. Chandra, V. Keppens, D. Mandrus, M. A. McGuire, B. C. Sales, A. S. Sefat, and J. Schmalian, Effects of Nematic Fluctuations on the Elastic Properties of Iron Arsenide Superconductors, *Phys. Rev. Lett.* **105**, 157003 (2010).

[72] Y. Gallais, R. M. Fernandes, I. Paul, L. Chauvière, Y. X. Yang, M. A. Méasson, M. Cazayous, A. Sacuto, D. Colson, and A. Forget, Observation of Incipient Charge Nematicity in $Ba(Fe_{1-x}Co_x)_2As_2$, *Phys. Rev. Lett.* **111**, 267001 (2013).

[73] A. E. Böhmer, P. Burger, F. Hardy, T. Wolf, P. Schweiss, R. Fromknecht, M. Reinecker, W. Schranz, and C. Meingast, Nematic Susceptibility of Hole-Doped and Electron-Doped $BaFe_2As_2$ Iron-Based Superconductors from Shear Modulus Measurements, *Phys. Rev. Lett.* **112**, 047001 (2014).

[74] S. Nandi, M. G. Kim, A. Kreyssig, R. M. Fernandes, D. K. Pratt, A. Thaler, N. Ni, S. L. Bud'ko, P. C. Canfield, J. Schmalian, R. J. McQueeney, and A. I. Goldman, Anomalous Suppression of the Orthorhombic Lattice Distortion in Superconducting $Ba(Fe_{1-x}Co_x)_2As_2$ Single Crystals, *Phys. Rev. Lett.* **104**, 057006 (2010).

[75] E. C. Blomberg, M. A. Tanatar, R. M. Fernandes, I. I. Mazin, B. Shen, H. H. Wen, M. D. Johannes, J. Schmalian, and R. Prozorov, Sign-Reversal of the in-Plane Resistivity Anisotropy in Hole-Doped Iron Pnictides, *Nat. Commun.* **4**, 1914 (2013).

[76] E. P. Rosenthal, E. F. Andrade, C. J. Arguello, R. M. Fernandes, L. Y. Xing, X. C. Wang, C. Q. Jin, A. J. Millis, and A. N. Pasupathy, Visualization of Electron Nematicity and Unidirectional Antiferroic Fluctuations at High Temperatures in NaFeAs, *Nat. Phys.* **10**, 225 (2014).

[77] H. Takahashi, K. Igawa, K. Arii, Y. Kamihara, M. Hirano, and H. Hosono, Superconductivity at 43 K in an Iron-Based Layered Compound $LaO_{1-x}F_xFeAs$, *Nature* **453**, 376 (2008).

[78] C. Hess, A. Kondrat, A. Narduzzo, J. E. Hamann-Borrero, R. Klingeler, J. Werner, G. Behr, and B. Buchner, The Intrinsic Electronic Phase Diagram of Iron-Oxypnictide Superconductors, *EPL* **87**, 17005 (2009).

[79] L. X. Yang, B. P. Xie, Y. Zhang, C. He, Q. Q. Ge, X. F. Wang, X. H. Chen, M. Arita, J. Jiang, K. Shimada, M. Taniguchi, I. Vobornik, G. Rossi, J. P. Hu, D. H. Lu, Z. X. Shen, Z. Y. Lu, and D. L. Feng, Surface and Bulk Electronic Structures of LaFeAsO Studied by Angle-Resolved Photoemission Spectroscopy, *Phys. Rev. B* **82**, 104519 (2010).

[80] X. D. Zhou, C. Ye, P. Cai, X. F. Wang, X. H. Chen, and Y. Y. Wang, Quasiparticle Interference of C_2-Symmetric Surface States in a LaOFeAs Parent Compound, *Phys. Rev. Lett.* **106**, 087001 (2011).

[81] Q. Zhang, R. M. Fernandes, J. Lamsal, J. Yan, S. Chi, G. S. Tucker, D. K. Pratt, J. W. Lynn, R. W. McCallum, P. C. Canfield, T. A. Lograsso, A. I. Goldman, D. Vaknin, and R. J. McQueeney, Neutron-Scattering Measurements of Spin Excitations in LaFeAsO and $Ba(Fe_{0.953}Co_{0.047})_2As_2$: Evidence for a Sharp Enhancement of Spin Fluctuations by Nematic Order, *Phys. Rev. Lett.* **114**, 057001 (2015).

[82] H. Luetkens, H.-H. Klauss, M. Kraken, F. J. Litterst, T. Dellmann, R. Klingeler, C. Hess, R. Khasanov, A. Amato, C. Baines, M. Kosmala, O. J. Schumann, M. Braden, J. Hamann-Borrero, N. Leps, A. Kondrat, G. Behr, J. Werner, and B. Büchner, The Electronic Phase Diagram of the $LaO_{1-x}F_xFeAs$ Superconductor, *Nat. Mater.* **8**, 305 (2009).

[83] T. M. McQueen, A. J. Williams, P. W. Stephens, J. Tao, Y. Zhu, V. Ksenofontov, F. Casper, C. Felser, and R. J. Cava, Tetragonal-to-Orthorhombic Structural Phase Transition at 90 K in the Superconductor $Fe_{1.01}Se$, *Phys. Rev. Lett.* **103**, 057002 (2009).

[84] T. Tohei, T. Mizoguchi, H. Hiramatsu, Y. Kamihara, H. Hosono, and Y. Ikuhara, Direct Imaging of Doped Fluorine in $LaFeAsO_{1-x}F_x$ Superconductor by Atomic Scale Spectroscopy, *Appl. Phys. Lett.* **95**, 193107 (2009).

[85] C. Cantoni, J. E. Mitchell, A. F. May, M. A. McGuire, J. C. Idrobo, T. Berlijn, E. Dagotto, M. F. Chisholm, W. Zhou, S. J. Pennycook, A. S. Sefat, and B. C. Sales, Orbital Occupancy and Charge Doping in Iron-Based Superconductors, *Adv. Mater.* **26**, 6193 (2014).

[86] P. Gao, Y. Zhang, S. Y. Zhang, S. Lee, J. Weiss, J. R. Jokisaari, E. E. Hellstrom, D. C. Larbalestier, C. B. Eom, and X. Q. Pan, Atomic and Electronic Structures of Superconducting $BaFe_2As_2/SrTiO_3$ Superlattices, *Phys. Rev. B* **91**, 104525 (2015).

[87] J. Yang, R. Zhou, L. L. Wei, H. X. Yang, J. Q. Li, Z. X. Zhao, and G. Q. Zheng, New Superconductivity Dome in $LaFeAsO_{1-x}F_x$ Accompanied by Structural Transition, *Chin. Phys. Lett.* **32**, 107401 (2015).

[88] E. J. Kirkland, *Advanced Computing in Electron Microscopy* (Springer Publishing, New York, 2010).

[89] D. R. Cremons and D. J. Flannigan, Direct *In Situ* Thermometry: Variations in Reciprocal-Lattice Vectors and Challenges with the Debye–Waller Effect, *Ultramicroscopy* **161**, 10 (2016).

[90] D. A. Muller, T. Sorsch, S. Moccio, F. H. Baumann, K. Evans-Lutterodt, and G. Timp, The Electronic Structure at the Atomic Scale of Ultrathin Gate Oxides, *Nature* **399**, 758 (1999).

[91] D. A. Muller, L. F. Kourkoutis, M. Murfitt, J. H. Song, H. Y. Hwang, J. Silcox, N. Dellby, and O. L. Krivanek, Atomic-Scale Chemical Imaging of Composition and Bonding by Aberration-Corrected Microscopy, *Science* **319**, 1073 (2008).

[92] R. Ramachandramoorthy, R. Bernal, and H. D. Espinosa, Pushing the Envelope of *In Situ* Transmission Electron Microscopy, *ACS Nano* **9**, 4675 (2015).

[93] J.-Q. Yan, S. Nandi, J. L. Zarestky, W. Tian, A. Kreyssig, B. Jensen, A. Kracher, K. W. Dennis, R. J. McQueeney, A. I. Goldman, R. W. McCallum, and T. A. Lograsso, Flux Growth at Ambient Pressure of Millimeter-Sized Single Crystals of LaFeAsO, $LaFeAsO_{1-x}F_x$, and $LaFe_{1-x}Co_xAsO$, *Appl. Phys. Lett.* **95**, 222504 (2009).

[94] J. M. Cowley and A. F. Moodie, The Scattering of Electrons by Atoms and Crystals. I. A New Theoretical Approach, *Acta Crystallogr.* **10**, 609 (1957).

[95] R. F. Loane, P. R. Xu, and J. Silcox, Thermal Vibrations in Convergent-Beam Electron-Diffraction, *Acta Crystallogr., Sect. A* **47**, 267 (1991).

[96] N. Qureshi, Y. Drees, J. Werner, S. Wurmehl, C. Hess, R. Klingeler, B. Büchner, M. T. Fernández-Díaz, and M. Braden, Crystal and Magnetic Structure of the Oxypnictide Superconductor $LaFeAsO_{1-x}F_x$: A Neutron-Diffraction Study, *Phys. Rev. B* **82**, 184521 (2010).

[97] R. F. Egerton, *Electron Energy-Loss Spectroscopy in the Electron Microscope* (Springer, New York, 2011).

[98] J. Fertig and H. Rose, Resolution and Contrast of Crystalline Objects in High-Resolution Scanning-Transmission Electron-Microscopy, *Optik* **59**, 407 (1981).

[99] S. Hillyard, R. F. Loane, and J. Silcox, Annular Dark-Field Imaging: Resolution and Thickness Effects, *Ultramicroscopy* **49**, 14 (1993).

[100] J. M. LeBeau, S. D. Findlay, L. J. Allen, and S. Stemmer, Quantitative Atomic Resolution Scanning Transmission Electron Microscopy, *Phys. Rev. Lett.* **100**, 206101 (2008).

[101] D. O. Klenov, S. D. Findlay, L. J. Allen, and S. Stemmer, Influence of Orientation on the Contrast of High-Angle Annular Dark-Field Images of Silicon, *Phys. Rev. B* **76**, 014111 (2007).

[102] K. A. Mkhoyan, S. E. Maccagnano-Zacher, E. J. Kirkland, and J. Silcox, Effects of Amorphous Layers on ADF-STEM Imaging, *Ultramicroscopy* **108**, 791 (2008).

[103] S. E. Maccagnano-Zacher, K. A. Mkhoyan, E. J. Kirkland, and J. Silcox, Effects of Tilt on High-Resolution ADF-STEM Imaging, *Ultramicroscopy* **108**, 718 (2008).

[104] D. Van Dyck and W. Coene, The Real Space Method for Dynamical Electron Diffraction Calculations in High Resolution Electron Microscopy: I. Principles of the Method, *Ultramicroscopy* **15**, 29 (1984).

[105] O. Ugurlu, J. Haus, A. Gunawan, M. Thomas, S. Maheshwari, M. Tsapatsis, and K. Mkhoyan, Radiolysis to Knock-on Damage Transition in Zeolites under Electron Beam Irradiation, *Phys. Rev. B* **83**, 113408 (2011).

[106] R. Egerton, Electron Energy-Loss Spectroscopy in the TEM, *Rep. Prog. Phys.* **72**, 016502 (2008).

[107] J. C. Spence, Absorption Spectroscopy with Sub-Angstrom Beams: ELS in STEM, *Rep. Prog. Phys.* **69**, 725 (2006).

[108] R. M. Fernandes and J. Schmalian, Manifestations of Nematic Degrees of Freedom in the Magnetic, Elastic, and Superconducting Properties of the Iron Pnictides, *Supercond. Sci. Technol.* **25**, 084005 (2012).

[109] I. Shein and A. Ivanovskii, Elastic Properties of Quaternary Oxypnictides LaOFeAs and LaOFeP as Basic Phases for New 26–52 K Superconducting Materials from First Principles, *Scripta Mater.* **59**, 1099 (2008).

[110] R. Abd-Shukor, Calculated Sound Velocity Change in $LaFeAsO_{0.89}F_{0.11}$ at the Superconducting Transition, *J. Supercond. Novel Magn.* **23**, 1229 (2010).

[111] D. R. Cremons, D. A. Plemmons, and D. J. Flannigan, Femtosecond Electron Imaging of Defect-Modulated Phonon Dynamics, *Nat. Commun.* **7** (2016).

[112] A. Yurtsever and A. H. Zewail, 4D Nanoscale Diffraction Observed by Convergent-Beam Ultrafast Electron Microscopy, *Science* **326**, 708 (2009).

[113] L. Rettig, S. Mariager, A. Ferrer, S. Grübel, J. Johnson, J. Rittmann, T. Wolf, S. Johnson, G. Ingold, and P. Beaud, Ultrafast Structural Dynamics of the Fe-Pnictide Parent Compound $BaFe_2As_2$, *Phys. Rev. Lett.* **114**, 067402 (2015).

[114] S. Gerber, K. Kim, Y. Zhang, D. Zhu, N. Plonka, M. Yi, G. Dakovski, D. Leuenberger, P. Kirchmann, and R. Moore, Direct Characterization of Photoinduced Lattice Dynamics in $BaFe_2As_2$, *Nat. Commun.* **6** (2015).

[115] L. Rettig, S. Mariager, A. Ferrer, S. Grübel, J. Johnson, J. Rittmann, T. Wolf, S. Johnson, G. Ingold, and P. Beaud, Ultrafast Structural Dynamics of the Orthorhombic Distortion in the Fe-Pnictide Parent Compound $BaFe_2As_2$, *Struct. Dyn.* **3**, 023611 (2016).

[116] G. M. Vanacore, R. M. van der Veen, and A. H. Zewail, Origin of Axial and Radial Expansions in Carbon Nanotubes Revealed by Ultrafast Diffraction and Spectroscopy, *ACS Nano* **9**, 1721 (2015).

[117] L. Piazza, C. Ma, H. Yang, A. Mann, Y. Zhu, J. Li, and F. Carbone, Ultrafast Structural and Electronic Dynamics of the Metallic Phase in a Layered Manganite, *Struct. Dyn.* **1**, 014501 (2014).

[118] R. M. van der Veen, T. J. Penfold, and A. H. Zewail, Ultrafast Core-Loss Spectroscopy in Four-Dimensional Electron Microscopy, *Struct. Dyn.* **2**, 024302 (2015).

[119] M. He and T.-M. Lu, *Metal-Dielectric Interfaces in Gigascale Electronics: Thermal and Electrical Stability* (Springer Science & Business Media, New York, NY, USA, 2012).

[120] M. H. Kryder, E. C. Gage, T. W. McDaniel, W. Challener, R. E. Rottmayer, G. Ju, Y.-T. Hsia, and M. F. Erden, Heat Assisted Magnetic Recording, *Proc. IEEE* **96**, 1810 (2008).

[121] W. A. Challener, C. Peng, A. V. Itagi, D. Karns, W. Peng, Y. Peng, X. Yang, X. Zhu, N. J. Gokemeijer, Y.-T. Hsia, G. Ju, R. E. Rottmayer, M. A. Seigler, and E. C. Gage, Heat-Assisted Magnetic Recording by a Near-Field Transducer with Efficient Optical Energy Transfer, *Nat. Photonics* **3**, 220 (2009).

[122] T. Rausch, E. Gage, and J. Dykes, in *Ultrafast Magnetism I*, edited by J.-Y. Bigot, W. Hübner, T. Rasing and R. Chantrell (Springer Proceedings in Physics, Switzerland, 2015), Vol. 159, p. p. 200.

[123] R. Ji, B. Xu, Z. Cen, J. F. Ying, and Y. T. Toh, Thermal Effects on Transducer Material for Heat Assisted Magnetic Recording Application, *J. Appl. Phys.* **117**, 17A918 (2015).

[124] T. Zhao, M. C. Kautzky, W. A. Challener, and M. A. Seigler, *HAMR NFT Materials with Improved Thermal Stability* (Seagate Technology LLC, U.S., 2013).

[125] N. Zhou, X. Xu, A. T. Hammack, B. C. Stipe, K. Gao, W. Scholz, and E. C. Gage, Plasmonic near-Field Transducer for Heat-Assisted Magnetic Recording, *Nanophotonics* **3**, 141 (2014).

[126] P. Naumov, S. Chizhik, M. K. Panda, N. K. Nath, and E. Boldyreva, Mechanically Responsive Molecular Crystals, *Chem. Rev.* **115**, 12440 (2015).

[127] G. McMullan, A. R. Faruqi, D. Clare, and R. Henderson, Comparison of Optimal Performance at 300 keV of Three Direct Electron Detectors for Use in Low Dose Electron Microscopy, *Ultramicroscopy* **147**, 156 (2014).

[128] A. H. Zewail, Femtochemistry: Atomic-Scale Dynamics of the Chemical Bond, *J. Phys. Chem. A* **104**, 5660 (2000).

[129] O.-H. Kwon, B. Barwick, H. S. Park, J. S. Baskin, and A. H. Zewail, Nanoscale Mechanical Drumming Visualized by 4D Electron Microscopy, *Nano Lett.* **8**, 3557 (2008).

[130] J. S. Baskin, H. S. Park, and A. H. Zewail, Nanomusical Systems Visualized and Controlled in 4D Electron Microscopy, *Nano Lett.* **11**, 2183 (2011).

[131] D. J. Flannigan, P. C. Samartzis, A. Yurtsever, and A. H. Zewail, Nanomechanical Motions of Cantilevers: Direct Imaging in Real Space and Time with 4D Electron Microscopy, *Nano Lett.* **9**, 875 (2009).

[132] F. B. Stumpf, *Analytical Acoustics* (Ann Arbor Science, Ann Arbor, MI, USA, 1980).

[133] R. J. Stevens, A. N. Smith, and P. M. Norris, Measurement of Thermal Boundary Conductance of a Series of Metal-Dielectric Interfaces by the Transient Thermoreflectance Technique, *J. Heat Transfer* **127**, 315 (2005).

[134] F. Östlund, P. R. Howie, R. Ghisleni, S. Korte, K. Leifer, W. J. Clegg, and J. Michler, Ductile–Brittle Transition in Micropillar Compression of GaAs at Room Temperature, *Philos. Mag.* **91**, 1190 (2011).

[135] J. Michler, K. Wasmer, S. Meier, F. Östlund, and K. Leifer, Plastic Deformation of Gallium Arsenide Micropillars under Uniaxial Compression at Room Temperature, *Appl. Phys. Lett.* **90**, 043123 (2007).

[136] F. Östlund, K. Rzepiejewska-Malyska, K. Leifer, L. M. Hale, Y. Tang, R. Ballarini, W. W. Gerberich, and J. Michler, Brittle-to-Ductile Transition in Uniaxial Compression of Silicon Pillars at Room Temperature, *Adv. Funct. Mater.* **19**, 2439 (2009).

[137] J. Karch, R. Birringer, and H. Gleiter, Ceramics Ductile at Low-Temperature, *Nature* **330**, 556 (1987).

[138] B. R. Lawn, N. P. Padture, H. D. Cai, and F. Guiberteau, Making Ceramics Ductile, *Science* **263**, 1114 (1994).

[139] S. Korte and W. Clegg, Micropillar Compression of Ceramics at Elevated Temperatures, *Scripta Mater.* **60**, 807 (2009).

[140] S. Korte and W. Clegg, Discussion of the Dependence of the Effect of Size on the Yield Stress in Hard Materials Studied by Microcompression of MgO, *Philos. Mag.* **91**, 1150 (2011).

[141] Y. Zou and R. Spolenak, Size-Dependent Plasticity in Micron- and Submicron-Sized Ionic Crystals, *Philos. Mag. Lett.*, 1 (2013).

[142] C. Shin, H. H. Jin, W. J. Kim, and J. Y. Park, Mechanical Properties and Deformation of Cubic Silicon Carbide Micropillars in Compression at Room Temperature, *J. Am. Ceram. Soc.* **95**, 2944 (2012).

[143] A. Montagne, S. Pathak, X. Maeder, and J. Michler, Plasticity and Fracture of Sapphire at Room Temperature: Load-Controlled Microcompression of Four Different Orientations, *Ceram. Int.* **40**, 2083 (2014).

[144] X. Han, Y. Zhang, K. Zheng, X. Zhang, Z. Zhang, Y. Hao, X. Guo, J. Yuan, and Z. L. Wang, Low-Temperature In Situ Large Strain Plasticity of Ceramic SiC Nanowires and Its Atomic-Scale Mechanism, *Nano Lett.* **7**, 452 (2007).

[145] M. D. Uchic, D. M. Dimiduk, J. N. Florando, and W. D. Nix, Sample Dimensions Influence Strength and Crystal Plasticity, *Science* **305**, 986 (2004).

[146] W. W. Gerberich, W. M. Mook, C. R. Perrey, C. B. Carter, M. I. Baskes, R. Mukherjee, A. Gidwani, J. Heberlein, P. H. McMurry, and S. Girshick, Superhard Silicon Nanospheres, *J. Mech. Phys. Solids* **51**, 979 (2003).

[147] M. D. Uchic, P. A. Shade, and D. M. Dimiduk, Plasticity of Micrometer-Scale Single Crystals in Compression, *Annu. Rev. Mater. Res.* **39**, 361 (2009).

[148] J.-Y. Kim, D. Jang, and J. R. Greer, Tensile and Compressive Behavior of Tungsten, Molybdenum, Tantalum and Niobium at the Nanoscale, *Acta Mater.* **58**, 2355 (2010).

[149] E. Lilleodden, Microcompression Study of Mg (0001) Single Crystal, *Scripta Mater.* **62**, 532 (2010).

[150] M. Lowry, D. Kiener, M. LeBlanc, C. Chisholm, J. Florando, J. Morris Jr, and A. Minor, Achieving the Ideal Strength in Annealed Molybdenum Nanopillars, *Acta Mater.* **58**, 5160 (2010).

[151] E. Withey, A. Minor, D. Chrzan, J. Morris Jr, and S. Kuramoto, The Deformation of Gum Metal through in Situ Compression of Nanopillars, *Acta Mater.* **58**, 2652 (2010).

[152] D. Z. Chen, D. Jang, K. M. Guan, Q. An, W. Goddard III, and J. R. Greer, Nanometallic Glasses: Size Reduction Brings Ductility, Surface State Drives Its Extent, *Nano Lett.* **13**, 4462 (2013).

[153] E. Arzt, Size Effects in Materials Due to Microstructural and Dimensional Constraints: A Comparative Review, *Acta Mater.* **46**, 5611 (1998).

[154] J. Nowak, A. Beaber, O. Ugurlu, S. Girshick, and W. Gerberich, Small Size Strength Dependence on Dislocation Nucleation, *Scripta Mater.* **62**, 819 (2010).

[155] S. H. Oh, M. Legros, D. Kiener, and G. Dehm, In Situ Observation of Dislocation Nucleation and Escape in a Submicrometre Aluminium Single Crystal, *Nat. Mater.* **8**, 95 (2009).

[156] D. Chrobak, N. Tymiak, A. Beaber, O. Ugurlu, W. W. Gerberich, and R. Nowak, Deconfinement Leads to Changes in the Nanoscale Plasticity of Silicon, *Nat. Nanotechnol.* **6**, 480 (2011).

[157] T. S. Duffy, R. J. Hemley, and H.-k. Mao, Equation of State and Shear Strength at Multimegabar Pressures: Magnesium Oxide to 227 GPa, *Phys. Rev. Lett.* **74**, 1371 (1995).

[158] L. Xiong, Y. Chen, and J. Lee, Simulation of Dislocation Nucleation and Motion in Single Crystal Magnesium Oxide by a Field Theory, *Comput. Mater. Sci.* **42**, 168 (2008).

[159] L. Xiong and Y. Chen, Multiscale Modeling and Simulation of Single-Crystal MgO through an Atomistic Field Theory, *Int. J. Solids Struct.* **46**, 1448 (2009).

[160] W. Gerberich, W. Mook, C. Carter, and R. Ballarini, A Crack Extension Force Correlation for Hard Materials, *Int. J. Fract.* **148**, 109 (2007).

[161] R. Hacquart and J. Jupille, Hydrated MgO Smoke Crystals from Cubes to Octahedra, *Chem. Phys. Lett.* **439**, 91 (2007).

[162] M. Gajdardziska-Josifovska and R. Sharma, Interaction of Oxide Surfaces with Water: Environmental Transmission Electron Microscopy of MgO Hydroxylation, *Microsc. Microanal.* **11**, 524 (2005).

[163] R. Hacquart and J. Jupille, Morphology of MgO Smoke Crystallites Upon Etching in Wet Environment, *J. Cryst. Growth* **311**, 4598 (2009).

[164] K. L. Johnson, *Contact Mechanics* (Cambridge university press, 1987).

[165] C. O. Hulse and J. A. Pask, Mechanical Properties of Magnesia Single Crystals in Compression, *J. Am. Ceram. Soc.* **43**, 373 (1960).

[166] A. Kelly and N. H. Macmillan, *Strong Solids* (Clarendon Press Oxford, 1986).

[167] C. O. Hulse, S. M. Copley, and J. A. Pask, Effect of Crystal Orientation on Plastic Deformation of Magnesium Oxide, *J. Am. Ceram. Soc.* **46**, 317 (1963).

[168] P. R. Howie, S. Korte, and W. J. Clegg, Fracture Modes in Micropillar Compression of Brittle Crystals, *J. Mater. Res.* **27**, 141 (2012).

[169] D.-H. Chung, Elastic Moduli of Single Crystal and Polycrystalline MgO, *Philos. Mag.* **8**, 833 (1963).

[170] R. W. G. Wycoff, *Crystal Strucutre* (Wiley, New York, 1963).

[171] D. Hull and D. J. Bacon, *Introduction to Dislocations* (Butterworth-Heinemann, 2001).

[172] D. Dimiduk, M. Uchic, and T. Parthasarathy, Size-Affected Single-Slip Behavior of Pure Nickel Microcrystals, *Acta Mater.* **53**, 4065 (2005).

[173] M. Srinivasan and T. Stoebe, Effect of Impurities on the Mechanical Behavior of MgO Single Crystals, *J. Appl. Phys.* **41**, 3726 (1970).

[174] E. Hintsala, A. Wagner, W. Gerberich, and K. Mkhoyan, The Role of Back Stress in Sub-50 nm Si Nanocubes, *Scripta Mater.* **114**, 51 (2016).

[175] A. J. Wagner, E. D. Hintsala, P. Kumar, W. W. Gerberich, and K. A. Mkhoyan, Mechanisms of Plasticity in Near-Theoretical Strength Sub-100 nm Si Nanocubes, *Acta Mater.* **100**, 256 (2015).

[176] I. Issa, J. Amodeo, J. Réthoré, L. Joly-Pottuz, C. Esnouf, J. Morthomas, M. Perez, J. Chevalier, and K. Masenelli-Varlot, In Situ Investigation of MgO Nanocube Deformation at Room Temperature, *Acta Mater.* **86**, 295 (2015).

[177] U. S. Energy Information Administration. <Www.Eia.Gov> Accessed February 22, 2015.

[178] S. Chu and A. Majumdar, Opportunities and Challenges for a Sustainable Energy Future, *Nature* **488**, 294 (2012).

[179] O. Gutfleisch, M. A. Willard, E. Brück, C. H. Chen, S. Sankar, and J. P. Liu, Magnetic Materials and Devices for the 21st Century: Stronger, Lighter, and More Energy Efficient, *Adv. Mater.* **23**, 821 (2011).

[180] U. S. Department of Energy Critical Materials Strategy. <Energy.Gov/Sites/Prod/Files/Doe_Cms2011_Final.Pdf> December 2011.

[181] U. S. Department of Energy Advanced Research Projects Agency-Energy (ARPA-E) Rare Earth Alternatives in Critical Technologies (REACT).<Arpa-E.Energy.Gov> Accessed February 22, 2015.

[182] J.-P. Wang, N. Ji, X. Liu, Y. Xu, C. Sanchez-Hanke, Y. Wu, F. De Groot, L. F. Allard, and E. Lara-Curzio, Fabrication of $Fe_{16}N_2$ Films by Sputtering Process and Experimental Investigation of Origin of Giant Saturation Magnetization in $Fe_{16}n_2$, *Magnetics*, *IEEE Transactions on* **48**, 1710 (2012).

[183] H. Sawada, A. Nogami, T. Matsumiya, and T. Oguchi, Structural, Electronic, and Magnetic Properties of $Fe_{16}N_2$, *Phys. Rev. B* **50**, 10004 (1994).

[184] Y. Jiang, J. Liu, P. K. Suri, G. Kennedy, N. N. Thadhani, D. J. Flannigan, and J.-P. Wang, Preparation of an α″-$Fe_{16}N_2$ Magnet Via a Ball Milling and Shock Compaction Approach, *Adv. Eng. Mater.* (2015).

[185] K. Takagi, M. Akada, K. Ozaki, N. Kobayashi, T. Ogawa, Y. Ogata, and M. Takahashi, High-Pressure Sintering Behavior of α″-$Fe_{16}N_2$ Nanopowder, *J. Appl. Phys.* **115**, 103905 (2014).

[186] C. Wehrenberg, B. Zande, S. Simizu, R. Obermyer, S. Sankar, and N. Thadhani, Shock Compression Response of α″-$Fe_{16}N_2$ Nanoparticles, *J. Appl. Phys.* **111**, 3522 (2012).

[187] J.-P. Wang, S. He, and Y. Jiang, *Iron Nitride Permanent Magnet and Technique for Forming Iron Nitride Permanent Magnet* (Regents Of The University Of Minnesota, U.S., 2012).

[188] M. A. Mehedi, Y. Jiang, and J.-P. Wang, Microstructure Analysis of Melt Spun Fen Foils with α″-$Fe_{16}N_2$ Phase, *MRS Advances* **FirstView**, 1 (2016).

[189] M. A. Mehedi, Y. Jiang, P. K. Suri, D. J. Flannigan, and J.-P. Wang, Minnedust: A New Soft Magnetic Material with High Flux Density and Low Coercivity *(Submitted).*

[190] H. S. Park, O.-H. Kwon, J. S. Baskin, B. Barwick, and A. H. Zewail, Direct Observation of Martensitic Phase-Transformation Dynamics in Iron by 4D Single-Pulse Electron Microscopy, *Nano Lett.* **9**, 3954 (2009).